DAC-92200

Final Report
DEVELOPMENT OF A SYSTEM FOR PRESTRESSING BRITTLE MATERIALS

AUGUST 1967

Prepared under Contract No. NAS 7-429
for
National Aeronautics and Space Administration
Marshall Space Flight Center
Huntsville, Alabama

DAC-92200

Final Report
DEVELOPMENT OF A SYSTEM FOR PRESTRESSING BRITTLE MATERIALS

AUGUST 1967

By

L.B. GRESZCZUK AND H. LEGGETT
Missile and Space Systems Division
Douglas Aircraft Company
Santa Monica, California

Prepared under Contract No. NAS 7-429
for
National Aeronautics and Space Administration
Marshall Space Flight Center
Huntsville, Alabama

PREFACE

This Final Report was prepared by the Missile and Space Systems Division, Douglas Aircraft Company, Santa Monica, California, under Contract No. NAS 7-429 entitled, "Development of a System for Prestressing Brittle Materials." This program was monitored by National Aeronautics and Space Administration, Marshall Space Flight Center, V. F. Seitzinger, Project Engineer. The program was under the technical management of H. Leggett. Principal investigators were B. G. Leonard--Materials Development and L. B. Greszczuk--Structural Analysis. In addition to the principal investigators, personnel participating in this program were V. Edlin, C. A. Hauck, R. J. Miller, W. V. Mixon, C. T. Powers and T. T. Sakurai.

ABSTRACT

The concept of internally prestressing chemically consolidated zirconia with tungsten cable to increase flexural and tensile load-carrying ability of the ceramic at room and elevated temperature has been demonstrated. Stress at failure, taken as the stress at which the initial crack in the ceramic occurred, was increased four-fold in flexure and eight-fold in tension. A theory whereby the strength of the composite is predicted from the properties of the constituents was developed for estimating the initial and ultimate strengths of the developed composites. Experimental data obtained in this program demonstrated the validity of the developed theory. Analytical trade-off studies were also conducted on the strength of composites incorporating various combinations of matrix (ceramic) and reinforcement materials. These trade-off studies were used to rate the efficiency of these composites at room and elevated temperatures, and also to select the ceramic and reinforcement to be used in this program. The two materials chosen for study, tungsten cables and chemically consolidated zirconia, were characterized for mechanical and physical properties at room and elevated temperatures.

CONTENTS

FIGURES

TABLES

Section 1
INTRODUCTION

The potential for the use of ceramic materials as load carrying members in an elevated temperature environment is extremely favorable because of low densities, non-oxidizing characteristics, relatively high compression strengths and moduli of elasticity, and high melting points. However, the actual usage of ceramics as load carrying members in aerospace vehicles has been practically nonexistent. If ceramics or other brittle, inorganic nonmetallic materials are to be used as load carrying members for high temperature applications, the inherent low tensile strengths must be circumvented and the high compressive strengths and moduli of elasticity used advantageously. The objective of this program was to develop a method for prestressing brittle materials, such as ceramics, in order to circumvent their inherent low tensile strength and to increase the resistance to failure from induced thermal and mechanical stresses.

The concept employed in this program to attain the stated objective consisted of internally precompressing a ceramic material with continuous pretensioned metal filaments while processing the composite at a low temperature. The ceramic slurry was cast around the pretensioned filaments. The ceramic was chemically consolidated at approximately 600°F (316°C), thus eliminating the degradation of the metal reinforcing which occurs if conventional high temperature ceramic processing is used. After curing, the load on the filaments was released thereby placing the ceramic in compression. Thus, to fail the ceramic in tension, the induced compressive stress must first be overcome. This results in an increase in tensile load carrying ability of the ceramic and imparts a degree of yielding prior to failure.

The program was divided into three phases to provide a continuity of material selection, analytical studies, and development and evaluation of behavior of the composites.

1.1 PHASE I--SELECTION OF MATRIX AND REINFORCEMENT MATERIALS

The candidate matrix materials were selected by compiling the pertinent data on the mechanical, physical, and thermophysical properties of the oxides, carbides, nitrides, and borides which had potential usage at elevated temperatures, and which were theoretically capable of being chemically consolidated (based upon original studies conducted at Douglas under Company sponsorship). The candidate reinforcement materials were selected on the basis of their ability to withstand the high temperature environment. Analysis methods were then developed for investigating the anchoring of the reinforcement, properties of reinforcement configuration, and for predicting the precompression of the ceramic and the strength of the prestressed reinforced composites subjected to external loads and thermal environment. Using this analysis, trade-off studies were conducted on the strength of composites employing various combinations of candidate matrix and reinforcement materials. These studies involved the investigation of strength of prestressed ceramics as a function of the following variables: matrix material, reinforcing material, volume of reinforcement, pretension (mechanical and thermal) of the reinforcement, and reinforcement configuration. The results of these studies were used to select the reinforcement and matrix materials to be used in this program.

1.2 PHASE 11--BONDING STUDIES AND MECHANICAL PROPERTIES DETERMINATIONS

Chemical consolidation studies were conducted on zirconium diboride, the matrix chosen in addition to zirconia. The latter material was selected prior to the literature survey. During the course *of* the development program in consolidating the zirconium diboride by casting, difficulties were encountered in excessive formation of volatiles. Although the hot pressing of chemically consolidated zirconium diboride was successful, it was felt that the effort required to develop a suitable casting formulation was not justified. As a consequence, alumina consolidated with orthophosphoric acid was selected as a substitute material. The choice of alumina was predicated on the relative ease of developing phosphate bonds of alumina without side reactions, and the excellent potential determined during the trade-off studies. Due to fabrication problems, alumina was substituted for the zirconium diboride. Physical and mechanical properties of the reinforcement were obtained up to **3,** 500°F (1,927°C), and properties of the matrixes were obtained to 2,500°F (1,371°C).

Characterization studies were conducted on the zirconia as well as the zirconium diboride. These studies included differential thermal analysis, thermogravimetric analysis, chemical content, density and particle size distribution. A basic understanding of the reactions occurring during chemical consolidation was obtained. Characterization studies of alumina were not conducted, as the material is well characterized in the literature.

1.3 PHASE 111--STRENGTH AND PROPERTIES OF THE COMPOSITE SYSTEM

Refinements were made in the structural analysis and the results obtained on strength-temperature relationships for the selected composites. Test specimens were designed and fabricated, according to the established pretension and volume of reinforcing material, and tested at room and elevated temperatures. A correlation was then made between the predicted and experimentally obtained strengths of composites to establish the validity of the theory and verify the efficiency of the concept of prestressing brittle materials.

Section 2
PROPERTIES OF CANDIDATE MATERIALS

The candidate matrix materials selected for consideration in this program, in addition to zirconia, were limited to materials which (1) could be chemically consolidated at low temperatures, (2) had high melting points, and **(3)** did not form a theoretical secondary low melting point phase. These materials included the borides and carbides of zirconium and hafnium, and the oxides of hafnium, aluminum, and thorium. The candidate reinforcement materials to be used for prestressing of the matrix were restricted primarily to the refractory metals.

2. 1 REINFORCING MATERIALS

The candidate materials selected for reinforcement and precompression of ceramics were tungsten (W), molybdenum (Mo), tantalum (Ta), rhenium (Re), and columbium (Cb). All the materials have melting points above 4, 300°F (2, 370°C) and are suitable for elevated temperature structural applications. Although some of the new inorganic filaments such as boron and graphite appeared as potential candidates, there was a lack of information on the elevated temperature properties of these materials.

The applicable properties of the various refractory metals are summarized in Table 2-1 and Figures 2-1 through 2-4. The reported data were obtained from a literature survey conducted in Phase I of the program. Table 2-1 shows the density, melting point, coefficient of thermal expansion, Young's modulus, shear modulus, and Poisson's ratio for the selected metals. The variation of Young's modulus, linear thermal expansion, and tensile strength as a function of temperature is shown in Figures 2-1, 2-2, and **2-3.** The references from which these data were obtained are shown in parentheses. Figure 2-4 shows the variation of tensile strength of filaments made of various materials as a function of filament diameter. For materials for which the data on the filaments strengths were not available, best strength values for the sheet are shown.

TABLE 2-1

PROPERTIES OF REFRACTORY METALS

Property \ Material	Tungsten (W)	Molybdenum (Mo)	Tantalum (Ta)	Columbium (Cb)	Rhenium (Re)
Density (lbs/in^3)	0.697 (1)	0.369 (4)	0.600 (14)	0.312 (12)	0.761 (13)
Melting Point (° F)	6170 (1, 2)	4740 (3)	5425 (12, 14)	4390 (12)	5740 (13)
Coeff. of Thermal Expansion at 20° C (/°C)	4.43×10^{-6} (2)	5.30×10^{-6} (3)	6.5×10^{-6} (14)	7.1×10^{-6} (7, 12)	6.6×10^{-6} (13)
Young's Modulus at 20° C, E (psi)	$50\text{-}59 \times 10^6$ (2, 8, 12)	$45\text{-}48 \times 10^6$ (3, 4, 5)	27×10^6 (6, 9, 14)	$12\text{-}16 \times 10^6$ (5, 10, 11, 14)	$64\text{-}70 \times 10^6$ (13)
Shear Modulus G (psi)	24×10^6 (2)	17.3×10^6 (4)	- -	5.44 (14)	- -
Poisson's Ratio	.284	.324 (4)	.35 (14)	.38 (14)	- -

Numbers in parentheses denote references

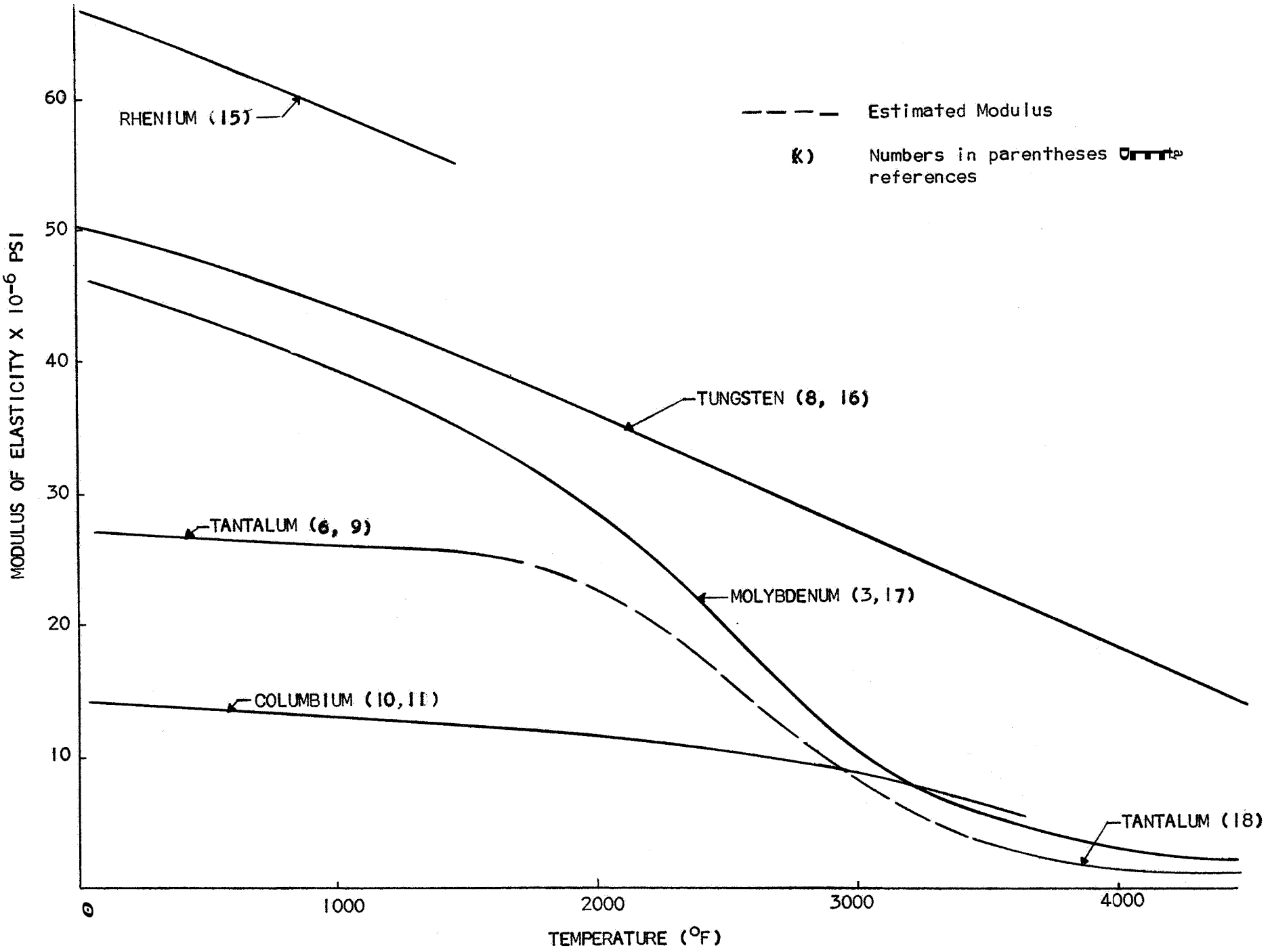

Figure 2-1. Modulus of Elasticity vs Temperature for Various Refractory Metals

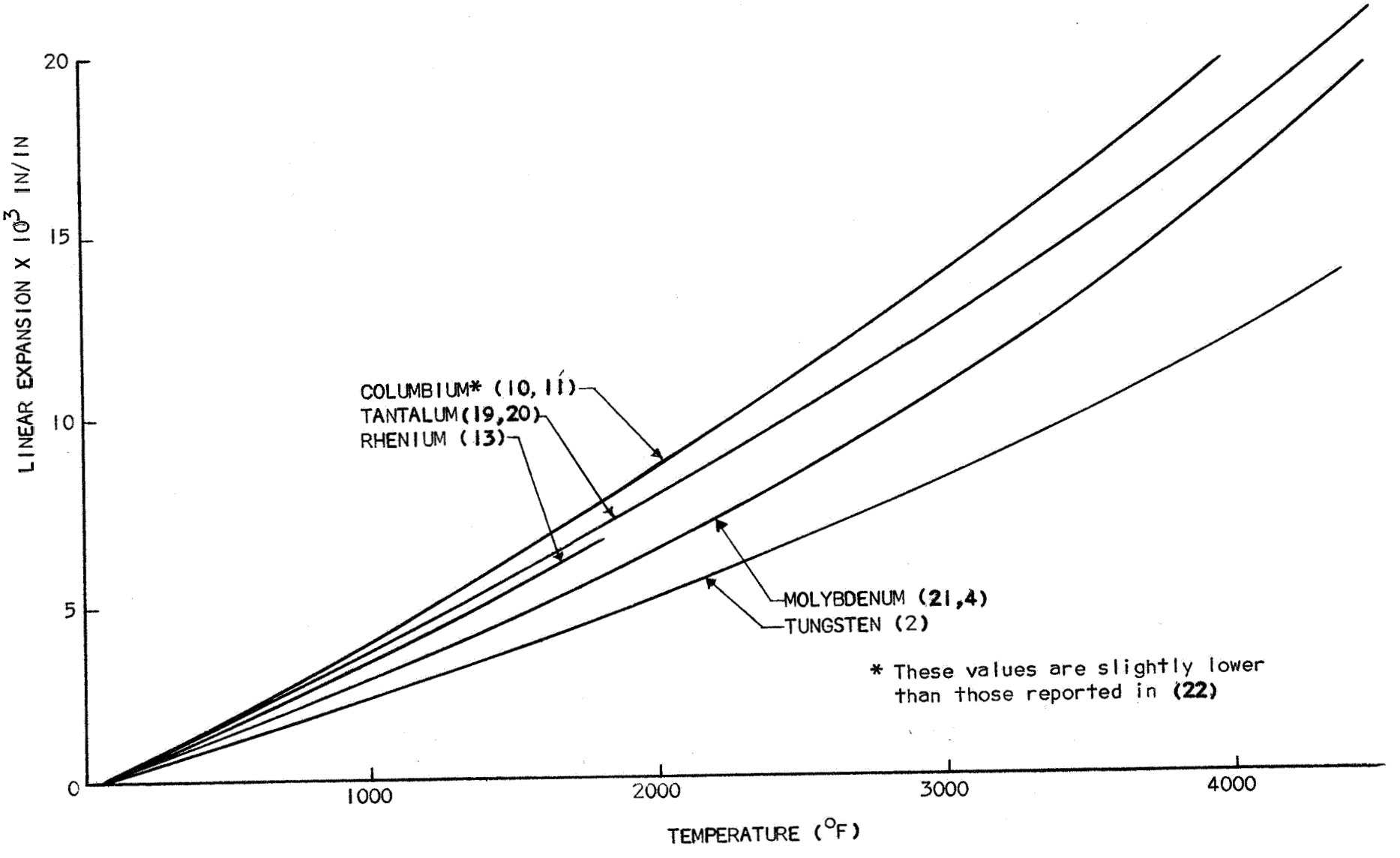

Figure 2-2. Linear Thermal Expansion vs Temperature for Various Refractory Metals

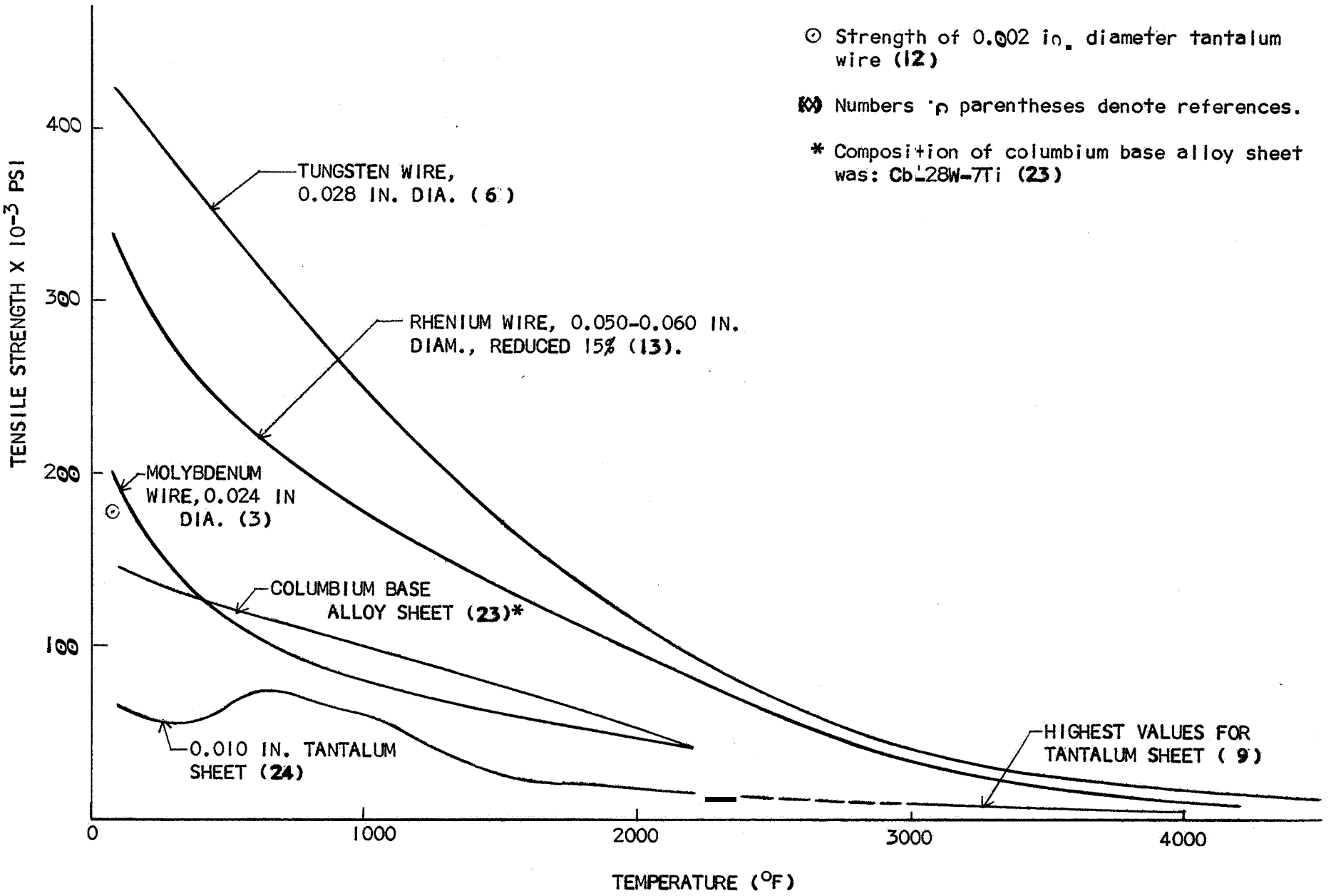

Figure 2-3. Tensile Strength vs Temperature for Various Refractory Metals

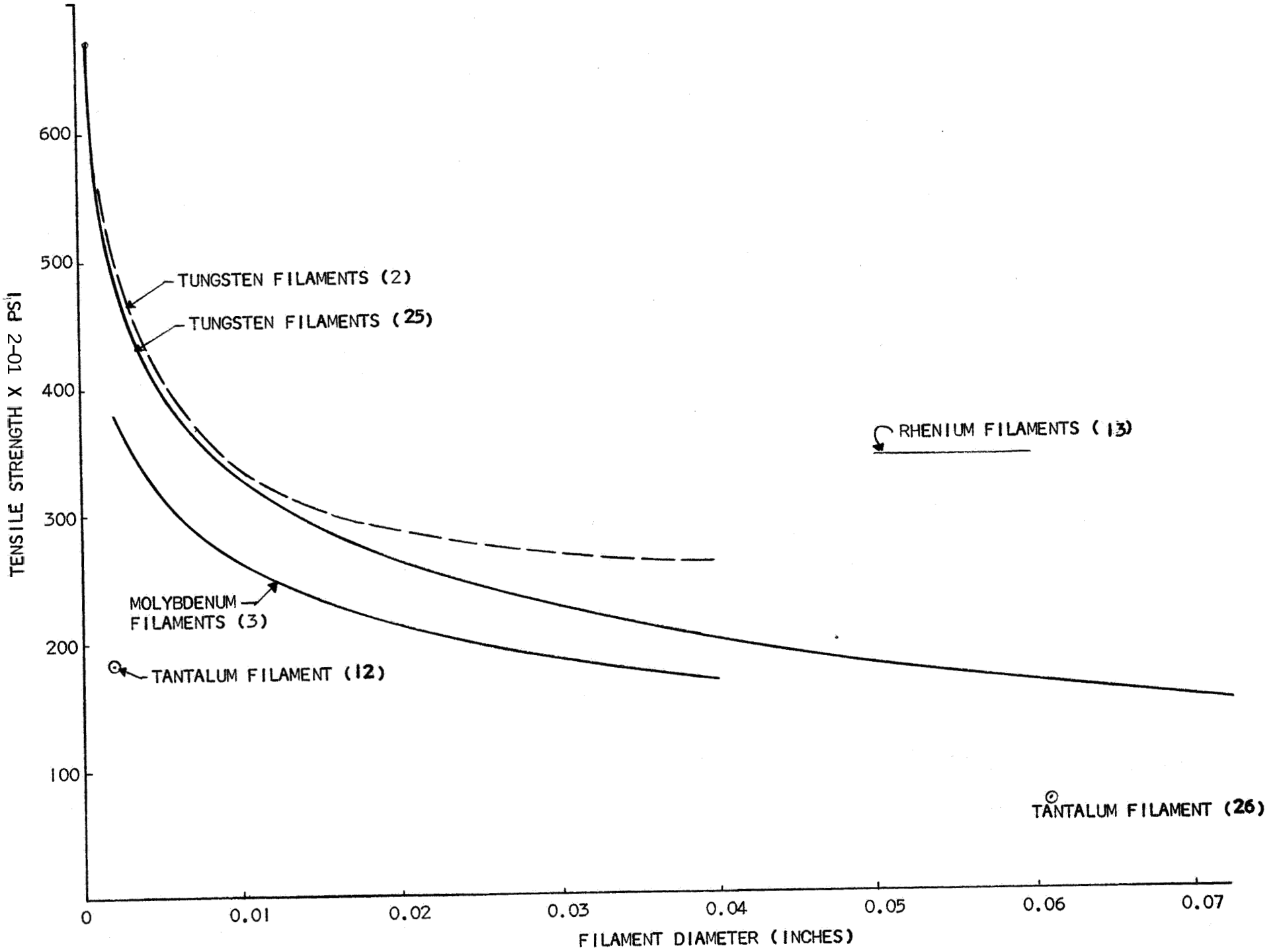

Figure 2-4. Tensile Strength vs Diameter of Refractory Metal Filaments

TABLE 2-2 (Pag

MECHANICAL AND THERMOPHYSICAL PROPERTIES OF MATE

		Al_2O_3	HfO_2	ThO_2	ZrO_2	HfB_2
Density (Lbs/Ft^3)		249[28]	624 to 688 604[31]	605 to 624 613[31]	319 354[31]	688 to 750 700[31]
Melting Point (°F)		3630 3722[29] 3704[31]	5140 5090[29] 5072[31]	5970[29] 5520[29] 5795[31]	5010[29] 4874[29] 4800[31]	5880[29] 5550[29] 5610[31]
Thermal Expansion (%)	500°F	--	0.20	--	0.20	0. 13 (32
	1000°F	0. 30	0.40	0.4	0.44	0.25
	2000°F	0.90	1.00	0.9	0.95	--
	2500°F	--	--	--	--	--
	3000°F	1.40	1.70	1.50	1.38	1.20
	4000"F	--	--	--	1.84	1.50
Thermal Conductivity (Btu/Hr. Ft. "F)	70°F	25	--	6.5	--	--
	500°F	10	--	4.0	0.6	--
	1000°F	6	--	3.5	0.5	--
	2000°F	3	1.6	2.0	0.8	30
	3000°F	3	1.6	--	0.8	30 33.4[32]
	3500°F	--	1.6	--	--	75[32]
	4000°F	--	1.6	--	1.7	--
Heat Capacity (Btu/Lb°F)	70°F	0.20	0.06	0.06	0.11	0.06
	1000°F	0. 27	0.08	0.07	0.13	0.07
	2000°F	0.20	0.10	0. 08	0.14	0.08
	2500°F	0.32	--	--	--	--
	3000°F	--	0.13	0.08	0.18	0.10
	4000°F	--	--	--	0.29	0.10
	4500°F	--	--	--	--	0.12
Emittance	500°F	0.72	--	--	--	--
	1000°F	0.62	--	--	0.67	0.4
	1500°F	--	0.85	0.3	--	--
	2000°F	0.42	0.85	0.3	0.40	0.6
	2500°F	0.38	0.85	0.3	--	--
	3000°F	--	0.85	0.3	0.60	0.8
	4000°F	--	0.85	--	0.60	0.8
	4500°F	--	--	--	--	0.7

ERIALS WHICH CAN BE CHEMICALLY CONSOLIDATED

ZrB_2	HfN	ZrN	HfC	ZrC
			792[29]	424
381[31]	866[31]	468[31]	782[31]	410[30]
				400 to 428[31]
5500[29]	5990[29]	5400[29]	7030[30]	6460[31]
5440[29]	5990[29]	5345[29]	7037[30]	6390[31]
5440[31]	5970[31]	5340[31]	7034[30]	6170[31]
) 0.13 (32)	0.20	0.25	--	--
0.25	0.30	0.50	0.25	0.40
0.50	0.70	0.90	0.50	0.80
--	1.20	--	.924[44]	.919[44]
0.90	--	1.25	0.81	1.20
			1.01	
1.30	--	1.90	1.10	1.70
--	--	--	12.9[33]	12[35]
25	7.5	6.5	--	16[40]
17	5.0	6.5	6.0	20
12	9.5	8.5	9.5	21
12	11.0	8.5	11.5	22
14[32]	15.0	--	22.6[33]	--
17	--	6.5	14.0	22
0. 14	--	0. 10	--	--
0, 15	0.06	0.12	0.06	0.11
0.20	0.08	0. 13	0.07	0. 13
--	--	--	--	--
0.20	0.06	0.13	0.07	0.13
0.20	0.06	0.13	0.07	0.15
--	--	--	--	--
--	--	--	--	--
--	0.55	--	--	--
0.35	--	--	0.97	--
0.72	0.75	0.73 to 0.76	0.97	0.77
--	--	--	--	--
0.72	0.72	--	0.85	0.77
0.70	0.56	--	0.70	0.77
0.60	0.62	--	--	--

TABLE 2

		Al_2O_3	HfO_2	ThO_2	ZrO_2	H
Thermal Diffusivity (Ft^2/Hr)	70°F	0.50	--	0.18	--	-
	635°F	--	--	--	--	-
	1000"F	0.09	--	0.09	0.01	-
	2000°F	0.05	0.03	0.07	0.01	0
	3000°F	--	0.02	--	0.01	0
	4000°F	--	--	--	0.02	-
Oxidation Resistance		Exc.	Exc.	Exc.	Exc.	F
Tensile Strength (KSI)	70°F	37.8	--	14	21	--
	70°F	42(37)	--	16(37)	20(37)	--
	570°F	37.4	--	--	--	--
	1470°F	34.2	--	--	16	--
	1624" F	--	--	--	16	--
	1800°F	--	--	--	--	--
	1800°F	--	--	--	--	--
	1920°F	33.8	--	--	--	--
	2000	30(37)	--	--	20(37)	--
	2192°F	18.5	--	--	11.9	--
	2192°F	--	--	--	13(34)	--
	2550°F	4.3	--	--	--	--
	2732	--	--	--	1.8(34)	--
	2804°F	--	--	--	1.9	--
Flexure Strength (KSI)	70°F	52(37)	10	16(43)b	3.5a	--
	70°F	--	--	--	26(37)	--
	500°F	46	--	2.0a	--	--
	1000°F	45	--	--	--	--
	1000°F	--	--	--	--	--
	1832°F	--	--	16.9	--	--
	2000°F	40	--	--	2.2	--
	2000°F	18(37)	--	--	--	--
	2500°F	30	--	--	--	--
	3000°F	--	--	--	--	--
	3500°F	--	--	--	--	--
	4000°F	--	--	0.5	0.5	--
Compressive Strength (KSI)	70°F	320	--	225	300	--
	70°F	350(37)	--	220(43)	350(37)	--
	500°F	266	--	--	--	-
	1000°F	200	--	100	325	-
	1110°F	--	--	84(34)	--	-
	1500°F	--	--	90	200	-
	1832°F	--	--	50(34)	170(34)	-
	2000°F	120	--	50	160	-
	2000°F	100(37)	--	--	120(37)	-
	2192°F	--	--	28(34)	110(34)	

(Page 2 of 3)

	ZrB_2	HfN	ZrN	HfC	ZrC
	--	--	--	--	0.593(40)
	--	--	--	--	0.338(40)
	0.30	0.10	0.12	0.08	0.44
4	0.16	0.13	0.14	0.17	0.39
3	0.16	0.21	0.14	0.21	0.39
	0.22	--	0.11	0.25	0.35
r	Exc. to 2000°F Poor above 2000°F	Good	Good	Poor	Poor
	28.7	--	--	35(39)	16
	29(32)	--	--	--	30(38)
	--	--	--	--	--
	--	--	--	--	--
	--	--	--	--	--
	--	--	--	--	13)
	--	--	--	--	
	--	--	--	22.5	--
	--	--	--	--	--
	--	--	--	--	--
	--	--	--	--	--
	--	--	--	--	--
	--	--	--	--	--
	--	--	--	--	12(38)c
	65	--	--	34.7	30(33)
	24(36)d	--	--	--	--
	24(36)d	--	--	--	23
	63	--	--	--	23
	24(36)d	--	--	--	--
	--	--	--	--	16(40)
	60	--	--	25(33)	24
	20(36)d	--	--	--	--
	14(36)d	--	--	16(33)	26(40)
	12(36)d	--	--	--	23
	3(36)d	--	--	12.6	18
	--	--	--	4.8	--
	225	--	--	--	238
	230(32)	--	--	--	--
	--	--	--	--	--
	--	--	--	--	--
	--	--	--	--	--
	--	--	--	--	--
	--	--	--	--	--
	25	--	--	--	--
	--	--	--	--	--
	--	--	--	--	--

TABLE 2-2

		Al_2O_3	HfO_2	ThO_2	ZrO_2	HfB
	2500°F	66	--	25	40	--
	2690°F	--	--	--	18[34]	--
	2800°F	--	--	1.4[34]	--	--
Modulus of Elasticity (10^6 psi)	70°F	50	8.2	20	23	--
	70°F	53[34]	--	--	--	--
	70°F	--	--	--	--	--
	500°F	--	--	19	--	--
	1000°F	48	--	18	21	--
	1000°F	50[34]	--	--	--	--
	1800°F	45[34]	--	--	--	--
	2000°F	39	--	15	17	--
	2500°F	28, 29[34]	--	13[42]	13	--
Shear Modulus (10^6psi)	70°F	19	--	14.3, 15	7.4, 8	--
	1000°F	18	--	13	--	--
	2000°F	15	--	6	--	--
	2500°F	10	--	--	--	--
Poisson's Ratio at 70°F		0.2 to 0.3	--	0.28	0.337[31]	--
		0.254[31]	--	--[31]	--	--
			--	0.275	0.26 to 0.29	--

a 79% Dense Bodies (SRI Data)
b 93% Dense Bodies[43]
c Tensile Strength at 3632°F = 3.5, at 3992°F = 2.5, at 4352°F = 1.5, at 4712°F
d Values for Boride Z

Note: All values shown without references were taken from Reference 28.

ZrB_2	HfN	ZrN	HfC	ZrC
--	--	--	--	--
--	--	--	--	--
50	--	--	21	34
50	--	--	61.5	49
--	--	--	46(33)	52(38)
--	--	--	--	51(40)
--	--	--	--	--
--	--	--	--	--
--	--	--	--	--
--	--	--	--	51(33)
--	--	--	--	--
--	--	--	--	--
27.8	--	--	---	18 24.7(40)
--	--	--	--	--
--	--	--	--	--
--	--	--	--	--
0.13 to	--	--	0.166(31)	0.257(31)
0. 14	--	--	--	--
0. 144(31)	--	--	--	0.167(40)

0.03(38) (KSI)

Tantalum and Ta-10W are compatible with alumina up to the melting point of alumina, and are also compatible with HfO_2 and calcia-stabilized zirconia to 4, 000°F (2, 204°C). Columbium has a tendency to react with alumina from the melting point of alumina to 4, 000°F (2, 204°C).

2. 3 REFERENCES FOR SECTION 2

1. Anon, Tungsten Wire, General Electric Company, Cleveland, Ohio.
2. Anon, Tungsten, Metalwerk Plansee, Aktiengesellschaft, Reutte, Tirol, Austria.
3. Anon, Molybdenum, Metalwerk Plansee, Gesellschaft, MBH Ruette, Tirol, Austria.
4. Anon, Molybdenum Metal, Climax Molybdenum Company, New York, 1960.
5. R. Syre, Niobium, Molybdenum, Tantalum and Tungsten - A Summary of Their Properties With Recommendations for Research and Development, AGARDOgraph 50, North Atlantic Treaty Organization Advisory Group for Aeronautics Research and Development, Paris, 1961.
6. Anon, Metals Handbook, Properties and Selection of Metals, American Society for Metals, Eighth Edition, Volume 1, 1961.
7. R. C. Tottle, The Physical and Mechanical Properties of Niobium, The Journal of the Institute of Metals, p. 375, Vol. LXXXV, 1956-57.
8. H. Parachenian, Tensile Properties of Commercially Pure Tungsten Sheet, Douglas Aircraft Company, Inc., Engineering Paper No. 1354, February 1962.
9. F. F. Schmidt, Tantalum and Tantalum Alloy, DMIC Report 133, Battelle Memorial Institute, July 1960.
10. F. F. Schmidt, and N. R. Ogden, The Engineering Properties of Columbium and Columbium Alloys, DMIC Report 188, Battelle Memorial Institute, September 1963.
11. T. E. Tietz, and J. W. Wilson, Mechanical, Oxidation and Thermal Property Data for Seven Refractory Metals and Their Alloys, Lockheed Missiles and Space Division, Contract No. AS 60-6119-C, Code 2. 36.61-1, September 1961.
12. W. Kohl, Material Technology for Electron Tubes, Reinhold Publishing Corp. New York.

13. C. T. Sims, C. M. Craighead, and R. I. Jaffe, Physical and Mechanical Properties of Rhenium, American Institute of Mining and Metallurgical Engineers, Transactions, Vol. 203, pp. 168-179, 1955.

14. Anon, Mechanical Properties of Tungsten, Tantalum, Molybdenum, and Columbium, Data Sheet Published by Fanstell Metallurgical Corp., Chicago, Illinois.

15. B. A. Rogers, The Properties of Eleven Less Common Metals, Chapter 9, Metals for Supersonic Aircraft and Missiles, edited by D. W. Grobecker, published by American Society for Metals, 1958.

16. F. F. Schmidt, and H. R. Ogden, The Engineering Properties of Tungsten and Tungsten Alloys, DMIC Report 191, Battelle Memorial Institute, September 1963.

17. F. F. Schmidt, and H. E. Ogden, The Engineering Properties of Molybdenum and Molybdenum Alloys, DMIC Report 190, pp. A-18, A-19, Battelle Memorial Institute, September 1963.

18. L. F. Glazier, R. D. Allen, and I. L. Saldinger, Mechanical and Physical Properties of Refractory Metals, Tungsten, Tantalum, and Molybdenum above 4000°F, Report No. M1826, Aerojet-General Corp., Azusa, California.

19. J. M. Cummings, Elevated Temperature Structural Materials Reference Book, Douglas Aircraft Company, Report SM-35575, February, 1959.

20. N. S. Rasor, and J. D. McClelland, Thermal Properties of Materials Part I Properties of Graphite, Molybdenum and Tantalum to Their Destruction Temperature, WADC Technical Report 56-240, March 1957.

21. A. Goldsmith, and T. E. Waterman, Thermophysical Properties of Solid Materials, WADC TR 58-476, January 1959.

22. I. B. Fieldhouse, J. C. Hedge, and J. I. Land, Measurements of Thermal Properties, WADC Technical Report 58-274, November 1958.

23. E. S. Bartlett, and J. A. Houck, Physical and Mechanical Properties of Columbium and Columbium Base Alloys, DMIC Report 125, Battelle Memorial Institute, February 1960.

24. J. W. Pugh, Temperature Dependence of the Tensile Properties of Tantalum, Transactions ASTM, Vol. 48, p. 677, 1956.

25. C. J. Smithells, Tungsten, Chapman and Hall Ltd., London, p. 161, 1952.

26. F. T. Sisco, E. Epremian, Columbium and Tantalum, John Wiley and Sons, New York, 1963.

27. J. E. Hauck, New Inorganic Filaments are Stiffer and Lighter than Metals, Materials in Design Engineering, Vol. 63, p. 82-85, February, 1966.

28. Refractory Ceramics of Interest in Aerospace Structural Applications, A Materials Selection Handbook, ADS-TDR-63-4102, October 1963

29. Properties of Refractory and Ablative Materials to 5000"F., Douglas Report SM-44549, November 1963.

30. E. G. Kendall, High Temperature Demands Turn Attention to Refractory Carbides, Ceramics News, July 1963.

31. Anon, Materials Index No. 1 and 2, High Temperature Materials Co., Lowell, Mass., 1963.

32. E. G, Kendall, The Refractory Borides, Ceramics News, October 1963.

33. P. T. B. Shaffer, High Temperature Materials, Plenum Press, New York, 1964.

34. J. D. McClelland, The Refractory Oxides, Ceramic Age, 1963.

35. C. R. Tipton, Jr., Editor, Reactor Handbook, Second Edition, Vol. 1, Materials, Interscience Publishers Inc., New York, 1960.

36. J. E. Howe, and W. C. Riley, Ceramics for Advanced Technologies, John Wiley & Sons, Inc., New York, 1965.

37. J. E. Howe, and W. C. Riley, Modern Ceramics - Some Principles and Concepts, John Wiley & Sons, Inc., New York, 1965.

38. M. H. Leipold, and T. H. Nielson, Mechanical and Thermal Properties of Hot-Pressed Zirconium Carbide Tested to 2600°C, J. P. L. TR No. 32-452, NASA Contract No. NASA 100.

39. W. S. Williams, and R. G. Lye, Research to Determine the Mechanisms Controlling Brittle-Ductile Behavior of Refractory Cubic Carbides, Union Carbide ML-TDR-64-25, Part II, April 1965.

40. D. P. H. Hasselman, and P. T. B. Shaffer, Factors Affecting Thermal Shock Resistance of Polyphase Ceramic Bodies, TW-ADD-TR-60-749 Part 11, April 1962.

41. K. R. Janowski, and R. Rossi, Development of Refractory Carbides for Severe Thermal Applications, 11th Refractory Composite Working Group Meeting, Los Angeles, January 1966.

42. Refractory Materials - DMIC Memorandum 44, February 26, 1960.

43. F. P. Knudsen, Dependence of Mechanical Strength of Brittle Polycrystalline Specimens on Porosity and Grain Size, J. Amer. Ceramic Society, August 1959.

44. C. R. Houska, Thermal Expansion of Certain Group IV and Group V Carbides at High Temperatures, J. Amer. Ceramic Society, August 1959.

Section 3
ANALYTICAL STUDIES OF PRESTRESSED CERAMICS

In order to establish the most desirable combinations of matrix and reinforcement materials described in Sections 2. 1 and 2. 2, pertinent equations have been derived for determining the ceramic precompression and the strength of prestressed composites as affected by the mechanical properties of the constituents, their volume fractions, and the mechanical and thermal pretension of the reinforcement. Although the analysis is an approximate one, a subsequent more rigorous analysis given in the appendix justifies its use for the composites under consideration. The analysis presented in the appendix is based on the consideration of the triaxial stresses in the constituents.

Analytical investigations of the properties of the reinforcement configuration and anchoring of the reinforcement are also presented in this section. The analysis is used in the trade-off studies on the most desirable combinations of materials to yield high strength-to-density ratios at room and elevated temperatures.

3.1 MECHANICAL AND THERMAL PRECOMPRESSION OF THE CERAMIC

An approximate relationship between the reinforcement pretension, ceramic precompression, thermally induced prestress, and other physical and mechanical properties of the matrix and the reinforcement can be established by considering a model shown in Figure 3-1.

The consideration of conditions of equilibrium of forces and compatibility of strains in the fiber direction requires that

$$\sigma_w A_w + \sigma_c A_c = 0 \qquad (3.1\text{-}1)$$

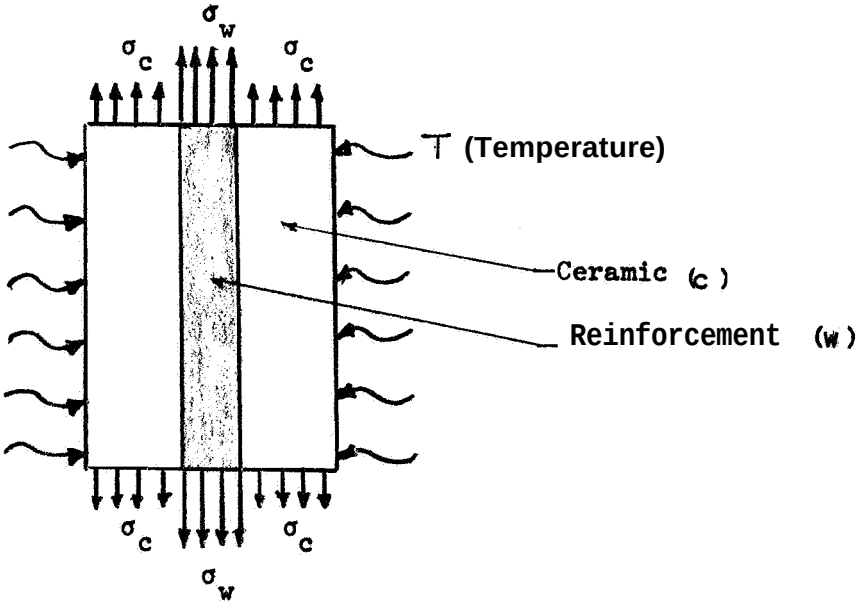

Figure 3-1. Element of Reinforced Ceramic

$$\epsilon_W = \epsilon_C \qquad (3.1\text{-}2)$$

where subscripts w and c denote the reinforcement and ceramic respectively, σ denotes stress, ϵ denotes strain, and **A** denotes cross-sectional area.

The relationship between the resultant strains, stresses, and temperature is

$$\epsilon_W = \frac{\mathbf{Au}_W}{E_w} + \alpha_w \, AT \qquad (3.1\text{-}3)$$

$$\epsilon_C = \frac{\sigma_C}{E_C} + \alpha_c \, AT \qquad (3.1\text{-}4)$$

where E denotes the modulus of elasticity, α denotes the coefficient of thermal expansion, AT is the difference between the initial and final temperature

$$AT = T_f - T_o \qquad (3.1\text{-}5)$$

and Au_W is the reduction in the initial, mechanically induced pretension of the wire σ_{wi}, due to precompression of the ceramic.

$$\sigma_W = \sigma_{wi} + \Delta\sigma_w \qquad (3.1\text{-}6)$$

Solving Equations 3.1-1, 3.1-2, **3.1-3, 3.1-4,** and 3.1-6 for σ_c yields*.

$$\sigma_C = -\left[\frac{\sigma_{wi}}{n + \frac{1 - k_w}{k_w}} \; t \; \frac{(\alpha_c - \alpha_w)\,\Delta T\, E_w}{n + \frac{1 - k_w}{k_w}}\right] \qquad (3.1\text{-}7)$$

where k_w is the volume fraction of reinforcement,

$$k_w = \frac{A_w}{A_W + A_C}$$

*The negative sign means that direction of σ_c is opposite to that shown in Figure 3-1.

and,

$$n = E_w/E_c$$

The first term in Equation **3.** 1-7 represents the precompression in the ceramic induced by relaxation of the pretensioned reinforcement, while the second term represents thermally induced precompression. From Equation **3.** 1-1 and **3.** 1-7, the remaining tension in the wire is

$$\sigma_W = \frac{\sigma_{wi} + (\alpha_c - \alpha_w)\,AT\,E_w}{\frac{n\,k_w}{1 - k_w} + 1} \qquad (3.\ 1\text{-}8)$$

It is obvious from Equation **3.** 1-7 that the following interrelationship exists between mechanically induced ceramic precompression and properties of constituents :

1. The induced precompression σ_C increases directly with the filament pretension σ_{wi},
2. Precompression σ_C can be increased by decreasing the modulus of elasticity of the filament, E_w, or increasing the modulus of elasticity of the ceramic,
3. The precompression σ_C can be increased by increasing the volume fraction of reinforcement, k_w.

The relationship between thermally induced precompression and the properties of constituents is:

1. For the case when the coefficient of thermal expansion of the ceramic is greater than that of the filament ($\alpha_c > \alpha_w$), and the composite is exposed to a temperature (T_f), precompression will be induced in the ceramic if $T_f > T_o$, where T_o is the processing temperature.
2. The thermally induced precompression will increase with increasing T_f.
3. The thermal precompression of the ceramic can be increased by increasing k_w, by increasing E_c, and by increasing E_w.

Figure 3-2 shows some typical numerical results on the precompression induced in the ceramic as affected by the properties of constituents, reinforcement content, and prestress.

3. 1. 1 Stresses Due to Externally Applied Load

If a composite such as shown in Figure 3-1 is subjected to an external force P, the stresses in the reinforcement and matrix can be obtained in a manner similar to that described above. For this condition, the stresses in the constituents are:

$$\sigma_c(P) = \frac{P}{A_w}\left[\frac{1}{n + \frac{1 - k_w}{k_w}}\right] \qquad (3.\ 1.\ 1\text{-}1)$$

$$\sigma_w(P) = \frac{P}{A_c}\left[\frac{1}{\frac{1}{n} + \frac{k_w}{1 - k_w}}\right] \qquad (3.\ 1.\ 1\text{-}2)$$

where $\sigma(P)$ denotes stress due to external load P.

By superposition, the total stresses due to mechanical and thermal prestress and the applied loading P are

$$\tilde{\sigma}_w = \sigma_w + \sigma_w(P) = \left\{\frac{Pn}{A_c} + \sigma_{wi} + (\alpha_c - \alpha_w)\,\Delta T\, E_w\right\}\left\{\frac{1}{\frac{n k_w}{1 - k_w}}\right\} \qquad t\ 1$$

(3. 1. 1-3)

$$\tilde{\sigma}_c = \sigma_c + \sigma_c(P) = \left|\frac{P}{} - {}_{wi} \qquad {}_{w})\,\Delta T\, E_w\right|\left\{\frac{1}{n + \frac{1 - k_w}{k_w}}\right\}$$

(3. 1. 1-4)

3.2 STRENGTH OF COMPOSITE

If the internal stresses in a composite due to externally applied loading, as well as mechanical and thermal prestress are known, the strength of a composite can be determined, Because of the nature of the construction, the failure of a composite will be progressive, that is, one of the constituents will

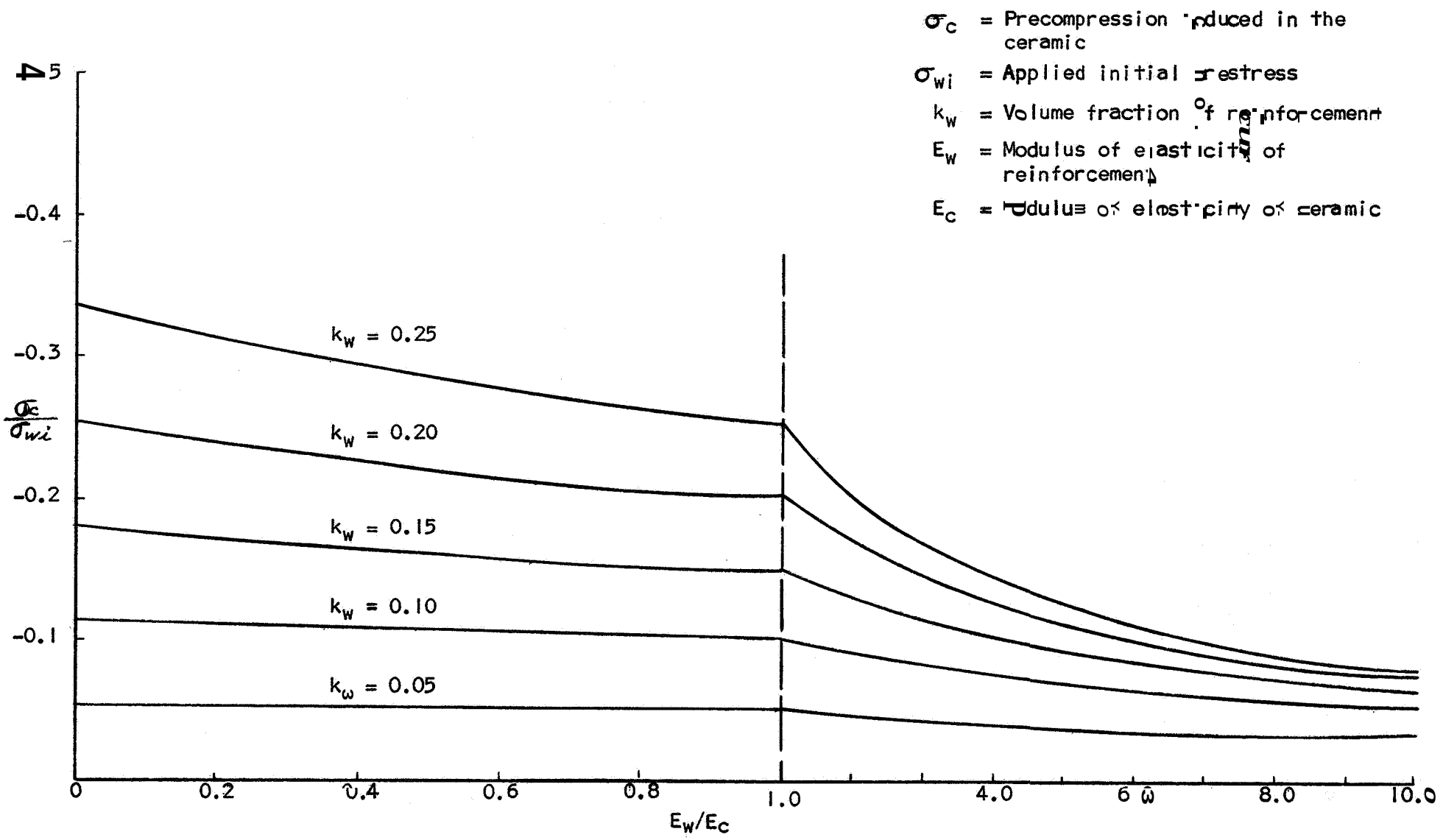

Figure 3-2. Effect of Volume Fractions and Properties of Constituents on Precompression of the Ceramic

fail first, which will lead to the failure of the other constituent. The important parameters influencing the failure of either of the constituents will be P, σ_{wi}, AT and the allowable strengths of the ceramic and the reinforcement. If the allowable tensile strength of the ceramic and the reinforcement at a given temperature are $(u_c)_A$ and $(\sigma_w)_A$ respectively, then the strength of a composite at that temperature can be estimated by setting.

$$\tilde{\sigma}_w = (\sigma_w)_A \tag{3.2-1}$$

$$\tilde{\sigma}_c = (\sigma_c)_A \tag{3.2-2}$$

and solving each of the equations for P. The lower of the **two** values of P will be the external load causing failure of a composite. From Equations **3. l. 1-3, 3. l. 1-4, 3.2-1,** and **3. 2-2** the stresses at which failure occurs can be written as

$$\sigma(w) = \left\{ (\sigma_w) \left[\frac{}{1-k} \quad 1 \right] - \sigma_{wi} - (\alpha_c - \alpha_w)\,\Delta T\, E_w \right\} \left(\frac{1-k_w}{n} \right) \tag{3.2-3}$$

$$\sigma(c) = \left\{ (\sigma_c)_A \left[n + \frac{1-k_w}{k_w} \right] + \sigma_{wi} + (\alpha_c - \alpha_w)\,\Delta T\, E_w \right\} k_w \tag{3.2-4}$$

For a given combination of materials the strength of a composite is obtained from Equations **3.2-3** and **3. 2-4.** The lower of the **two** values as computed from these equations is the strength of a composite. One additional factor which governs the composite strength is the magnitude of the initial prestress, σ_{wi}. The initial prestress σ_{wi} cannot exceed $(\sigma_w)_A$. The maximum value that σ_{wi} can reach is

$$(\sigma_{wi})_{max.} = (\sigma_w)_A - (\sigma_c)_A \frac{E_w}{E_c} - (\alpha_c - \alpha_w)\,\Delta T\, E_w \tag{3.2-5}$$

From the above equation it can be noted that $(\sigma_{wi})_{max.} < (\sigma_w)_A$. The above analysis and results are approximate, They are, however, sufficiently

accurate for the trade-off studies and for selecting the candidate constituent materials of a composite.

Some typical results relating strength of a composite with the properties of constituents and the filament prestress are shown in Figure **3-3.** It can be noted that the strength of the composite may be increased by increasing the initial filament prestress σ_{wi}, by increasing the Ew/Ec ratio, by increasing k_w, or by using filaments of high ultimate tensile strength, $(\sigma_w)_A$. Since for a given reinforcement material, consisting of two, three, or more twisted filaments, E_w may be varied by varying the twist or ℓ/r (see Section **3.** 5), this means that Figure **3-3** can be used for investigating the effect of reinforcement configuration (twist) on the strength of a composite. For any given value of E_c, the E_w/E_c scale shown in Figure **3-3** may be converted to ℓ/r scale with the help of results presented in Section **3.** 5. Thus if one sets E_w/E_c = 10 to correspond to $\ell/r = \infty$ (or $E_2^*/E = 1$), then for E_w/E_c = 9, ℓ/r = 14.* From Figure **3-3,** for an initial prestress of σ_{wi} = 200,000 psi, a reduction of 10% in E_w/E_c results in a 2. 5% reduction in the tensile strength of a composite. Thus, if the reinforcement configuration is such that $\ell/r \geq 14$, the maximum reduction in the tensile strength of a composite due to twist is about 2. 5%. Similarly, if σ_{wi} = 0 and $\ell/r \geq 14$, the maximum reduction in the composite tensile strength is about 5%. It is seen that **for** practical values of ℓ/r which are required to provide sufficient anchoring of the reinforcement, the reinforcement configuration has a minor influence on the strength of a composite. In view of the above findings it appeared reasonable to neglect the effect of reinforcement configuration in the trade-off studies, which are described in Section **3.6.**

3.3 ANCHORING OF REINFORCEMENT

The concept of precompressing ceramics to increase tensile load carrying ability consists of four steps:

1. The filaments (reinforcing) are pretensioned and held in a pretensioned position by anchoring to the mold or by other similar means.
2. A ceramic slurry is then cast around the pretensioned filaments.

*See Figure **3-8.**

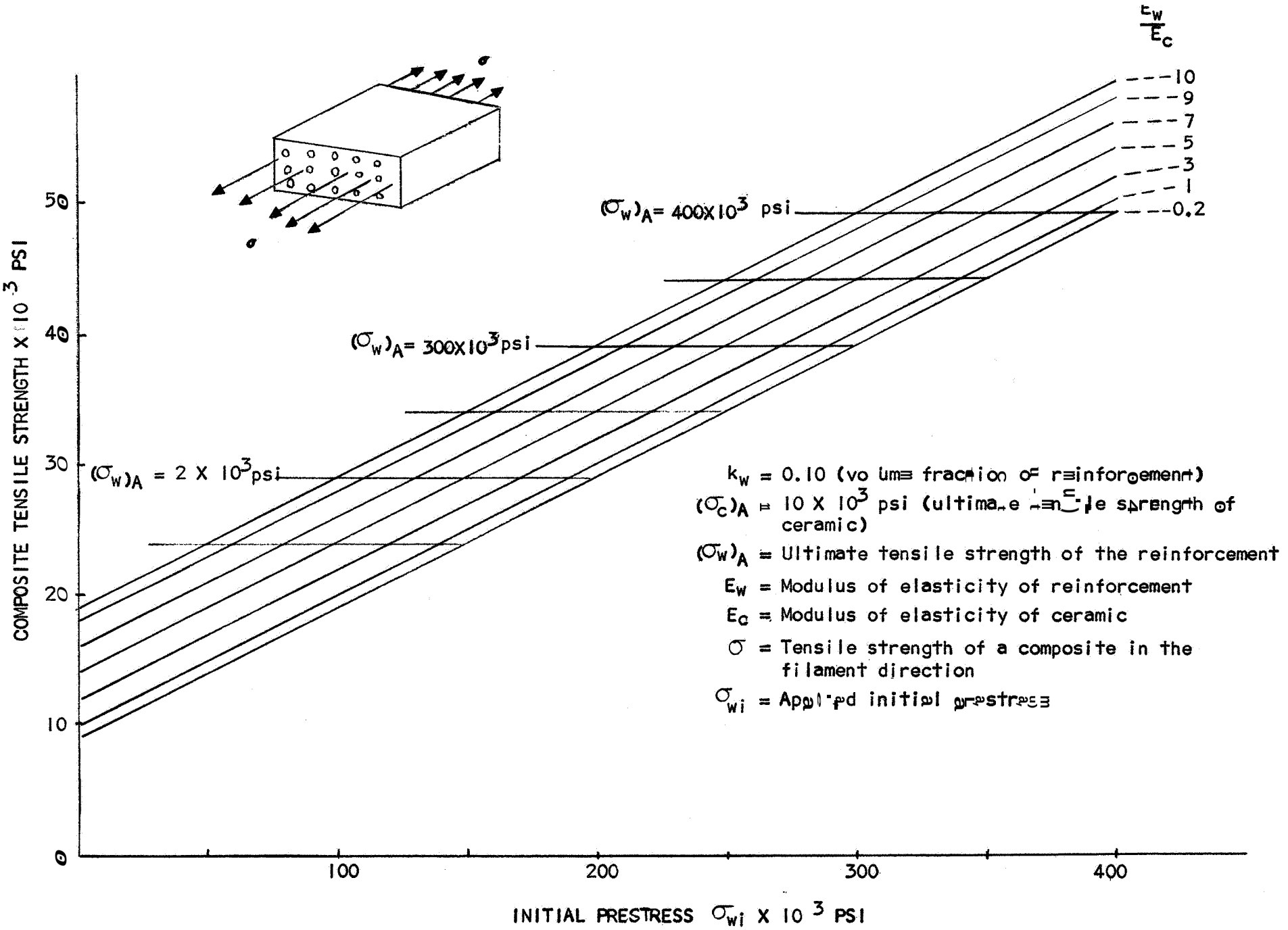

Figure 3-3. Tensile Strength of Composities vs Properties of Constituents (k_w, $(\sigma_w)_A$ = Constant)

3. The system is cured at a selected temperature between 400°F (204°C) and 600°F (316°C).

4. The specimen is removed from the mold.

Upon removal of the specimen from the mold, the filaments which were initially pretensioned tend to relax to their unstressed position. If there were no bond (chemical or mechanical) between the filaments and the ceramic, the filaments would relax to an unstressed position without inducing any precompression in the ceramic. If a bond does exist between the ceramic and the filaments, any stress relaxation in the filaments induces a pre-compression in the ceramic, Thus in order to induce precompression in the ceramic, the reinforcement must be anchored sufficiently to allow load transfer from the reinforcement to the ceramic without failure of the bond,

There are various means for achieving a sufficient bond between the filaments and the ceramic, Moreover, there are various types of bonds. The bond can be chemical or mechanical (frictional or shear), or various combinations of the two. Examples of anchoring configurations are illustrated in Figure 3-4.

3.3. 1 Chemical Bond

If untensioned reinforcement is placed in a ceramic slurry and the system is allowed to cure, some chemical bonding is expected to take place between the constituents. The strength of such a bond is however, expected to be weak unless either of the constituents is subjected to some special treatment to ensure a good bond. The determination of the existence as well as the strength of the chemical bond are discussed in Section 5.

3,3,2 Frictional Bond

If a ceramic slurry is cast around pretensioned filaments and, after the system has cured, the pretensioning device is removed, the reinforcement can be anchored through friction. Just before the removal of the pretension-ing device, the tension along the length of the filament will be uniform (neglecting thermal effects). After removal of the pretensioning device, the

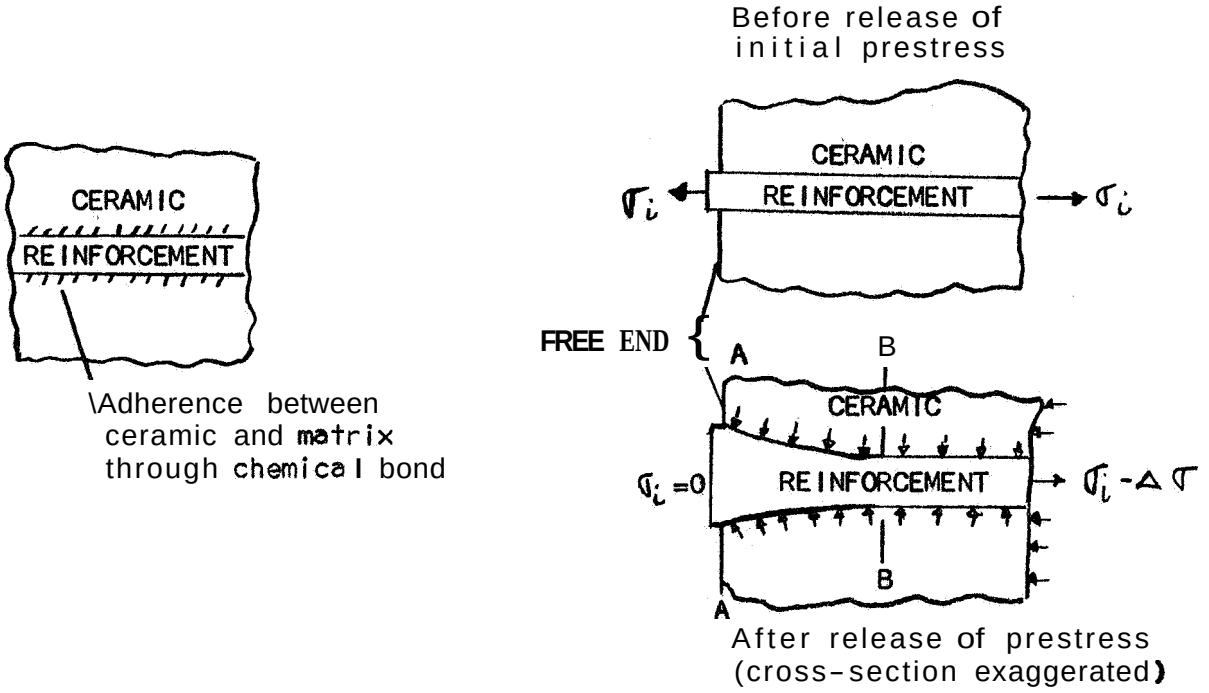

(a) Anchoring through chemical bond and friction

,Single square filament; anchoring through shear bond or friction.

Two or more circular filaments; anchoring through shear bond or friction.

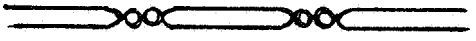

Two or more circular filaments with alternate lengths of twist and no twist; shear bond.

Strands of two or more filaments twisted into a strand; shear bond,

(b) Anchoring through mechanical action (or shear bond)

Figure 3-4. Reinforcement Anchoring Configurations

stress in the reinforcement at Section A-A (Figure 3-4a) will be zero, and the diameter of the reinforcement will be restored to the unstressed condition, At some Section B-B, the stress in the reinforcement will be

$$\sigma_i - \Delta\sigma_i$$

where σ_i is the initially applied pretension and $\Delta\sigma_i$ is the change in pretension due to deformation of the ceramic. Due to Poisson's ratio and to the restraint imposed by the ceramic on the reinforcement, the reinforcement diameter at B-B will be smaller than at A-A. Thus upon removal of the pretensioning device, the reinforcement will assume a conical shape with radial pressure action along it's length. Anchoring is achieved through a sort of wedging action, whereby the radial pressure gives rise to a frictional force along the transfer length. On the basis of such considerations, Hoyer (Reference 1) has derived the following expression for the length of transfer of load, L,

$$L = \frac{r}{u}(1 + \nu_c)\left(\frac{n}{\nu_w} - \frac{\sigma_i}{E_c}\right)\left(\frac{\sigma_e}{2\sigma_i - \sigma_e}\right) \qquad (3.3.2\text{-}1)$$

where,

r = filament radius

ν = Poisson's ratio

E = modulus of elasticity

u = coefficient of friction between constituent materials

σ_i = initial filament prestress

σ_e = effective filament prestress

$n = \frac{E_w}{E_c}$

c,w = subscripts denoting ceramic and reinforcement respectively

For a composite system consisting of zirconia and tungsten filaments with $\sigma_i = 150 \times 10^3$ psi, the L/r ratio is 25. The value is based on u = 0.30* and 10% volume fraction of filaments, and is the load transfer length required for the reinforcement to develop its 100% load carrying ability.

3.3.3 Mechanical Bond

In the various types of mechanical anchoring shown in Figure 3-4b, the load from the reinforcement to the ceramic is transferred by shear. Although all the anchoring configurations shown in Figure 3-4b are superior to those shown in Figure 3-4a, each of these shown in Figure 3-4b has some particular advantage. A single twisted filament of square cross section has a good anchoring ability and retains high proportion of the strength and stiffness of the basic material. By twisting two circular filaments into a strand, the shear bond strength can be increased. However, a somewhat greater reduction will occur in the stiffness and strength properties than for a square filament. A good shear bond can be obtained with a negligible loss in stiffness by utilizing reinforcement consisting of straight and twisted portions of filament. The strength of such a configuration will be similar to the strength of two twisted circular filaments. Finally, two double-filament strands may be twisted into a double strand as shown at the bottom right hand corner of Figure 3-4b. The reduction in stiffness and strength of such a configuration, as compared to the properties of the basic material, will be greater than that of the other configurations. The strength reduction of a double-stranded configuration may be overcome by utilizing very fine filaments to arrive at the same reinforcement volume fraction as in other configurations which require larger filaments. As was shown in Figure 2-4, the strength of a filament is strongly dependent on the filament diameter.

Although for the reinforcement configurations shown in Figure 3-4b, the anchoring is primarily through shear bond, there also exists secondary anchoring through friction and chemical bond. Due to complex interaction

* This is a coefficient of friction for 0.196" diameter drawn steel wire on smoothly finished concrete.

of the various types of bonds, the strength of such a configuration is extremely difficult to establish by rigorous theoretical means alone. Some insight into the efficiency of mechanical anchoring may, however, be obtained from consideration of some simple models.

At a point away from the ends, and approximate relationship between the tensile strength of the reinforcement, σ_w, shear strength of the ceramic, τ_c and ℓ/r for a two-filament twisted strand is

$$\frac{\ell}{r} = \frac{\sigma_w}{2\tau_c}$$

where r is the fiber radius, and ℓ represents the minimum length required to transfer the load from the fiber to the ceramic through shear. Thus if $\sigma_w = 300 \times 10^3$ psi and $\tau_c = 10 \times 10^3$ psi, then $\ell/r = 15$. If $\ell/r < 15$, and a tensile stress is applied to the reinforcement, the ceramic will fail in shear; if $\ell/r > 15$, the reinforcement will fail in tension. Similarly, for a three-filament strand the required ℓ/r is

$$\frac{\ell}{r} = 0.70 \left(\frac{\sigma_w}{\tau_c}\right)$$

3.4 REQUIRED SHEAR BOND STRENGTH IN A COMPOSITE BEAM UNDER LOAD

For a composite beam (Figure 3-5) subjected to some externally applied loading, the relationship between the tensile stresses in the ceramic or the reinforcement and the shear bond stresses may be obtained as follows: The equilibrium of forces (Figure 3-5c and d) requires that

$$V dx = M_B - M_A \qquad (3.4\text{-}1)$$

$$P_{WB} - P_{WA} = C\tau_c\, dx \qquad (3.4\text{-}2)$$

where C is the circumference of the shear circle. For convenience it is defined as

$$C = m\sqrt{\pi k_w} \qquad (3.4\text{-}3)$$

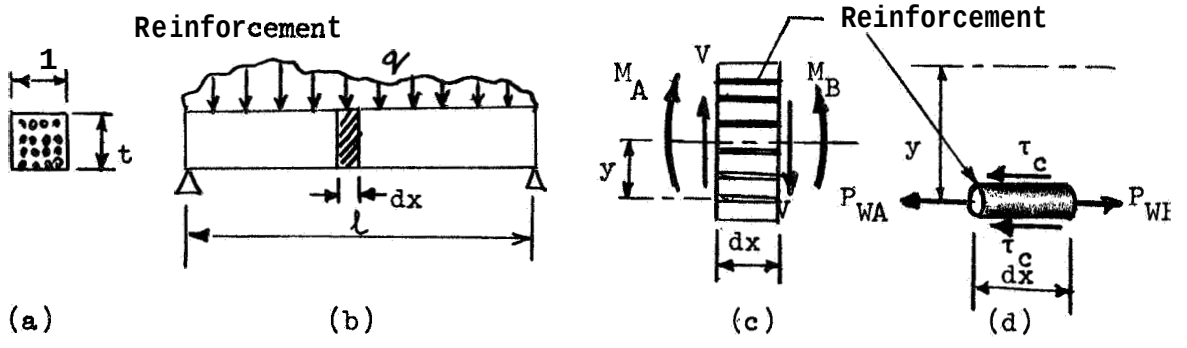

Figure 3-5. Composite Beam Under External Loading

where m is a function of the number of filaments in a reinforcement. For a single straight fiber, m = 2; for a two-filament twisted strand m = 2.828; for a three-filament twisted strand m = 2.480. Using some basic relationships from Section 3.1 (modified version of Equation 3. 1.1-2 together with the usual equation

$$\sigma = \frac{My}{I}$$

in combination with Equations 3.4-1, 3.4-2, and 3.4-3 one can readily arrive at the following relationship between τ, V and other parameters

$$\frac{\tau_c}{\sigma_w} = \left(\frac{1}{m}\right)\sqrt{\frac{k_w}{\pi}}\left(\frac{V}{M}\right) \qquad (3.4\text{-}4)$$

where τ_C is the shear stress between ceramic and reinforcement and σ_w is the direct stress in the reinforcement. For a beam subjected to a concentrated load at the midspan, typical results computed from Equation 3.4-4 are shown in Figure 3-6. Thus, if $\ell = 5''$, $k_w = 0.10$, and the tensile strength of the reinforcement is $\sigma_w = 200 \times 10^3$ psi, then for a single straight filament the required shear bond is

$$\tau_C = 7,200 \text{ psi};$$

for a two-filament strand the required shear bond is

$$\tau_C = 5,100 \text{ psi};$$

and for a three-filament strand the required shear bond is:

$$\tau_C = 5,800 \text{ psi}$$

Of the three cases considered, a two-filament strand is the most efficient anchoring configuration, since τ_C has the lowest values for that case.

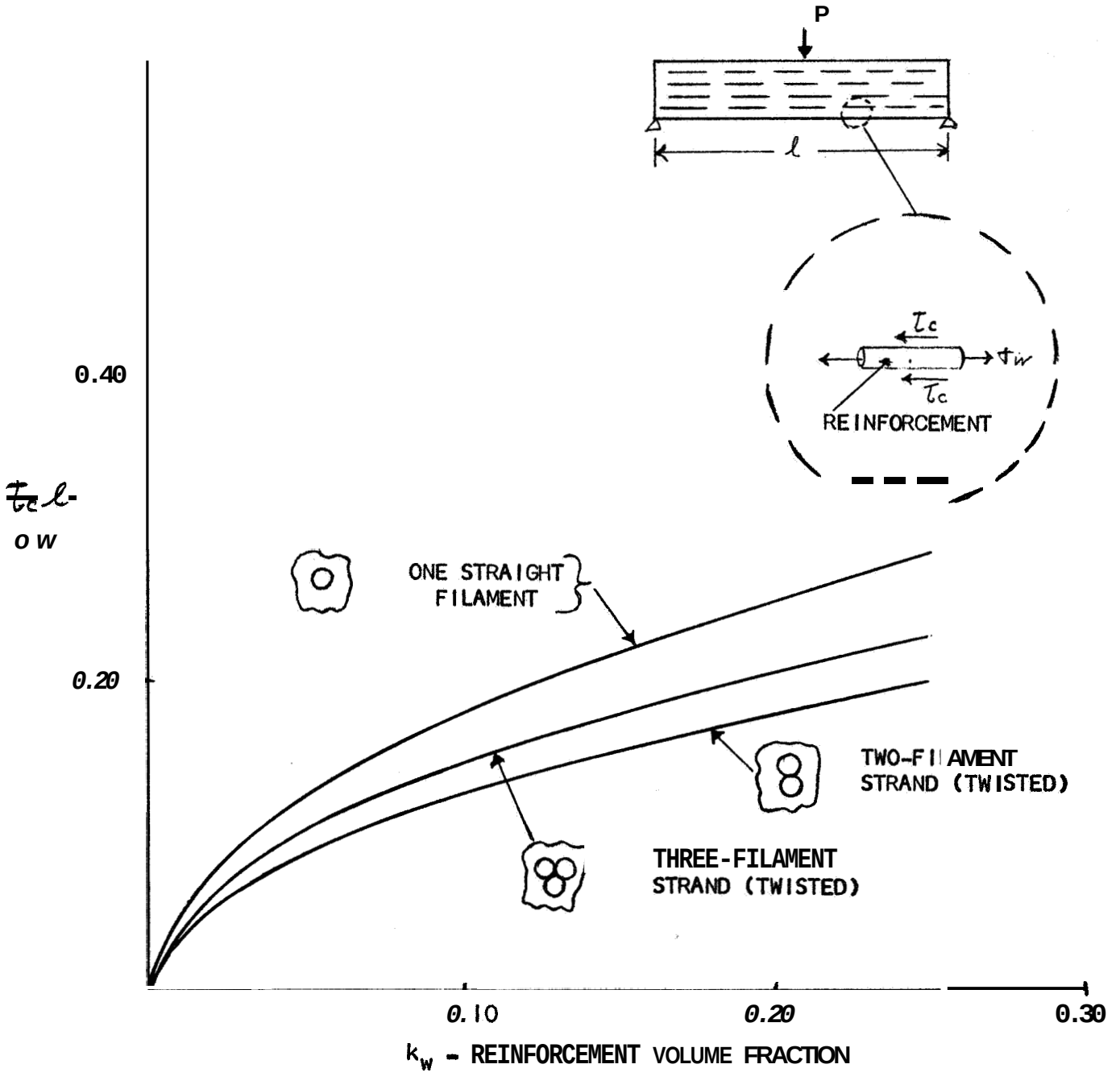

Figure 3-6. Effect of Reinforcement Volume Fraction and Reinforcement Configuration on the Shear Bond Stresses

3.5 PROPERTIES OF THE REINFORCEMENT CONFIGURATION

When two or more filaments are twisted to form a strand, the effective modulus of elasticity of such a strand will be lower than the modulus of elasticity of a straight filament. If the two filaments are not in firm contact along the whole length (Figure 3-7), the effective modulus of a strand will be a function of: the bending and extensional deformations, the load, the reinforcement geometry and fiber shape, and the basic material properties. The expression for the effective modulus may be derived by treating the filament as a curved beam undergoing beam-column action (Reference 2, **p.** 27). From such a consideration, the following approximate expression may be obtained:

$$E^* \approx E_\theta \left[1 + \frac{n^2}{\alpha} \left\{ 1 - \left(\frac{1}{1-\alpha} \right)^2 \left[f(\alpha, n, R) + 1 \right] \right\} \right]^{-1} \qquad (3.5\text{-}1)$$

where E_θ is the modulus of elasticity of the filament corrected for the helix angle, and where for a circular filament

$$n = h/r$$

$$\alpha = \frac{4 \sigma m^2}{E l l^2}$$

$$m = \ell/r$$

$$\sigma = P/\pi r^2$$

$$R = \text{contact reaction}$$

Using analysis similar to that employed by Huber (Reference 3), E_θ may be expressed in terms of E and the helix angle θ

$$E_\theta = E \cos^4 \theta \qquad (3.5\text{-}2)$$

where **for** a two-filament strand such as that shown in Figure 3-7a,

$$\theta = \cos^{-1} \left(\sqrt{\frac{1}{1 + \left(\frac{\pi n}{m} \right)^2}} \right) \qquad (3.5\text{-}3)$$

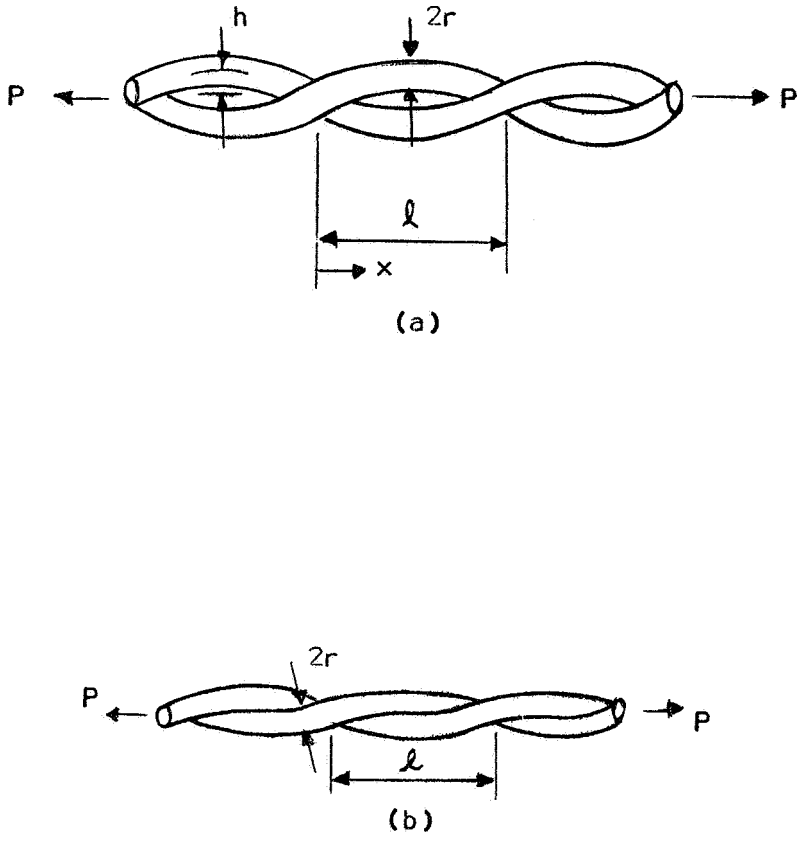

Figure 3-7. Two-Filament Reinforcement

The function f (cy, n, R) depends on the contact reaction of the adjacent filaments. If R = 0, then f (cy, n, R) = 0, and one obtains the effective modulus of a crimped filament (two-dimensional crimp). If the filaments are in firm contact (Figure 3-7b), then n = 1 and it may be shown that the term in Equation 3.5-1 in the outermost brackets is approximately equal to unity. Consequently, for a two-filament strand the effective modulus of elasticity is

$$E_2^* \approx \frac{E}{\left[1 + \left(\frac{\pi r}{\ell}\right)^2\right]^2} \qquad (3.5\text{-}4)$$

where the subscript "2" designates the number of filaments in a strand, Similarly for a three-filament strand,

$$E_3^* \approx \frac{E}{\left[1 + \frac{4}{3}\left(\frac{\pi r}{\ell}\right)^2\right]^2} \qquad (3.5\text{-}5)$$

The above equation can readily be extended to multifilament strands.

A comparison of experimental results with the theoretical results computed from Equation 3.5-4 is shown in Figure 3-8. The experimental results were obtained from tests conducted on two-filament strands made of 0.031" diameter steel filaments. The average error between experiment and theory is about 7%.

If the filaments are in firm contact (Figure 3-7b), the relationship between axial stress σ_8 in direction of load P, and the stress σ in the filament direction is

$$\sigma_\theta = \sigma_2 \cos^2\theta \qquad (3.5\text{-}6)$$

or in view of Equation 3.5-3

$$\frac{\sigma_\theta}{\sigma_2} \approx \frac{1}{\left[1 + \left(\frac{\pi r}{\ell}\right)^2\right]} \qquad (3.5\text{-}7)$$

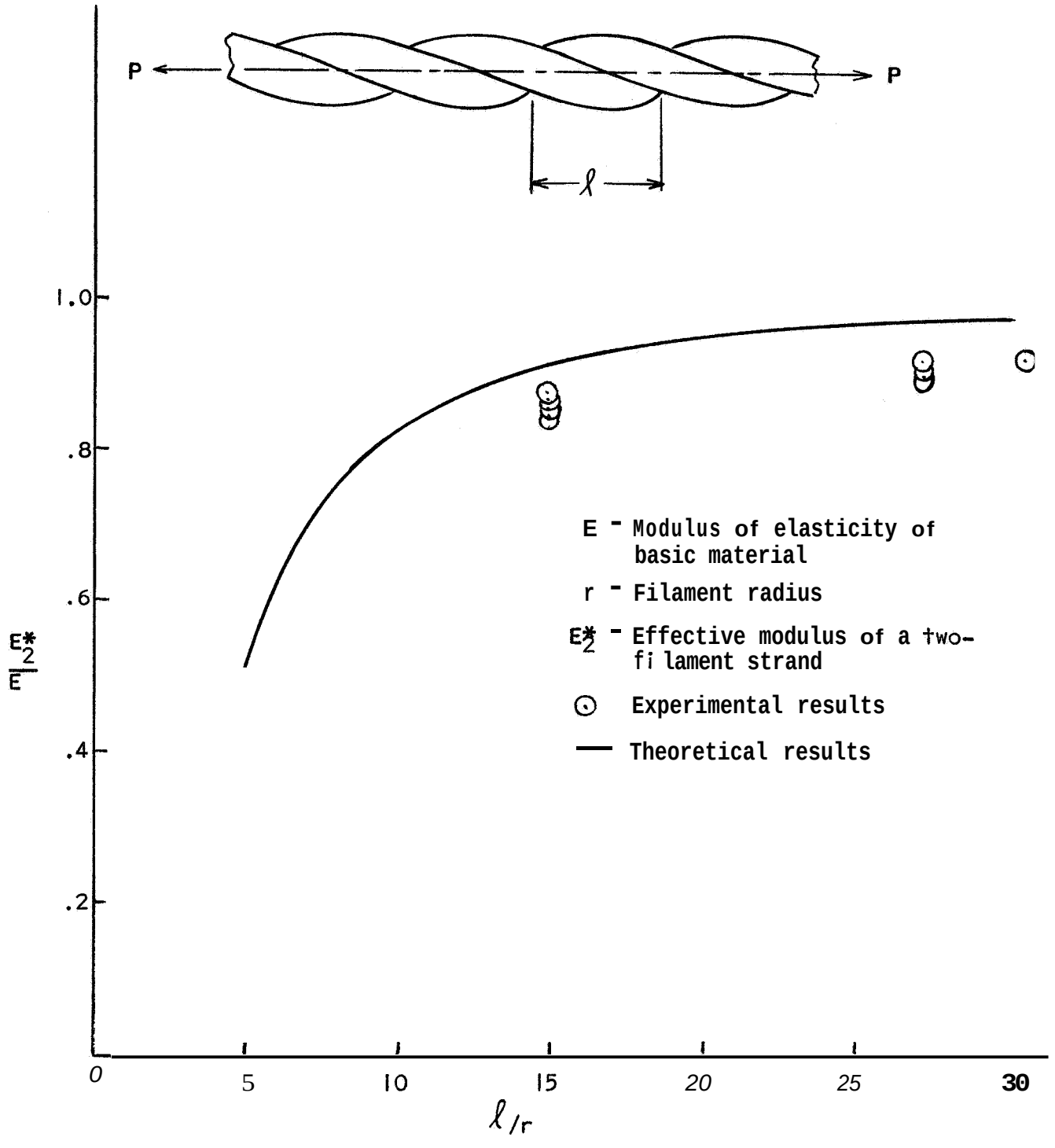

Figure 3-8. Effective Modulus of Elasticity of a Two-Filament Strand

Equation 3.5-7 may be used for estimating effective strength of twisted two-filament strands. As is shown in Reference 3, equations similar to 3.5-5 and 3.5-7 can be applied for investigating Young's modulus and effective strength of multi-fiber cables.

3.6 TRADE-OFF STUDIES

In order to establish what combinations of constituent materials - ceramics and reinforcement-which were investigated during the literature survey give composites with superior strength-to-density characteristics, trade-off studies were conducted, Equations given in Section 3.1 were used for this purpose. The strength and strength-to-density characteristics of various combinations of materials were obtained at room and elevated temperatures. The results of these studies were used to rate strength superiority of composites incorporating various combinations of materials. In view of the discussion given at the end of Section 3.2, the effect of the reinforcement configuration has been neglected in the trade-off studies,

3.6.1 Room Temperature Composite Ratings

The five ceramic materials on which sufficient data were available (see Section 2) for conducting the trade-off studies were: Al_2O_3, ThO_2, ZrO_2, ZrB_2 and ZrC. The five candidate reinforcing materials were: W, Mo, Cb, Re, and Ta. All the materials cited above retain high tensile strengths at elevated temperatures. For any given combination of materials and a given prestress, the tensile strength of the composite was obtained from Equation 3.2-3 and 3.2-4. These results were based on the maximum tensile strength of reinforcing materials (See Figure 2-4). Any prestress due to processing temperature was neglected. The composite strengths that were calculated were the ultimate tensile strengths. The composite ultimate tensile strength is defined as an externally applied stress which causes simultaneous failure in the matrix and the reinforcement. The ultimate strength is achieved by using an initial prestress σ_{wi} of such a magnitude that $\sigma_{(w)}$ and $\sigma_{(c)}$, as computed from Equations 3.2-3 and 3.2-4, are identical. The initial prestress required to satisfy the above condition is given by Equation 3.2-5.

Ultimate tensile strengths were obtained for various combinations of matrix and reinforcing materials, The composites were then rated in order of decreasing strength-density ratios. The results are shown in Figure 3-9. It is readily seen from Figure 3-9 that the order of composite ratings changes with k_w. For $k_w = 0.05$, the three superior ceramic materials are: Al_2O_3, ZrB_2, and ZrO_2; for $k_w = 0.10$ the three superior ceramics are: Al_2O_3, ZrO_2, and ZrB_2. For both cases the three superior reinforcing materials are W, Mo, and Re.

3.6.2 Elevated Temperature Composite Ratings

In view of the low room-temperature ratings of the columbium and tantalum reinforcing materials, they were deleted in the subsequent studies on the strength-to-density characteristics of composites. For the saine reason, thoria was also deleted from any further investigation. The ultimate strength of Composites at elevated temperatures were obtained using equations developed in Section 3.1, in coinbination with the strength properties of constituent materials as given in Section 2 and Figure 2-3, The filament sizes considered in this investigation were those for which elevated temperature tensile strength data were available (Figure 2-3).

The results showing strength-density ratings versus teinperature are shown in Figure 3-10. As can be noted from Figure 3-10, the inaterial rating change with temperature. Consequently, it is impossible to state that one of the five matrixes is the optimum. To reach such a conclusion the use temperature has to be known. For a temperature range of 0 to 3500°F (-17.8 to 1,927°C), zirconium diboride and zirconium carbide composites exhibit superior strength-to-density characteristics. As to the reinforcing material, of the various materials considered, tungsten is conclusively the optimum.

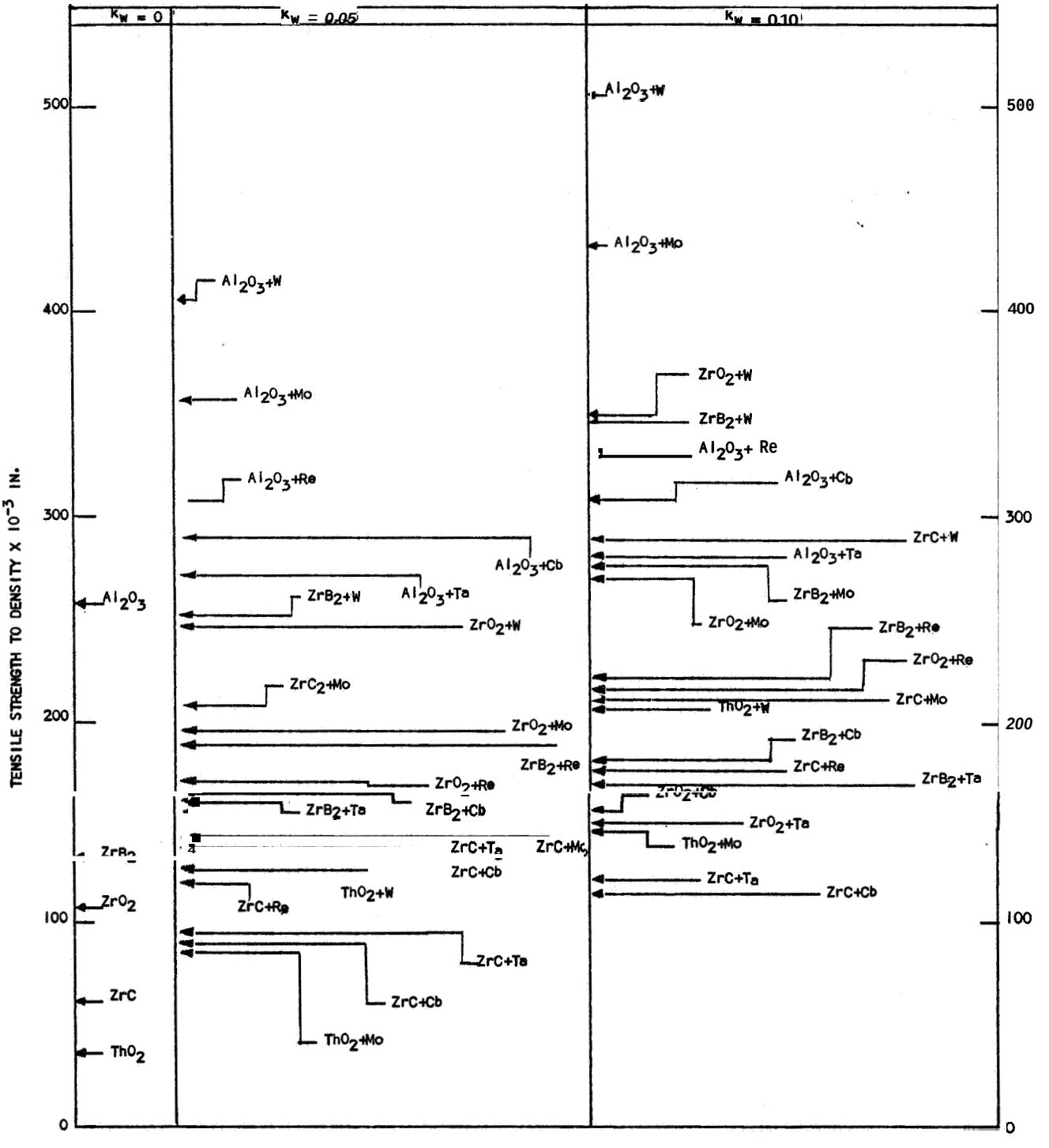

Figure 3-9. Ultimate Tensile Strength to Density Ratings for Prestressed Reinforced Ceramics (k_W = Volume Fraction of Reinforcement)

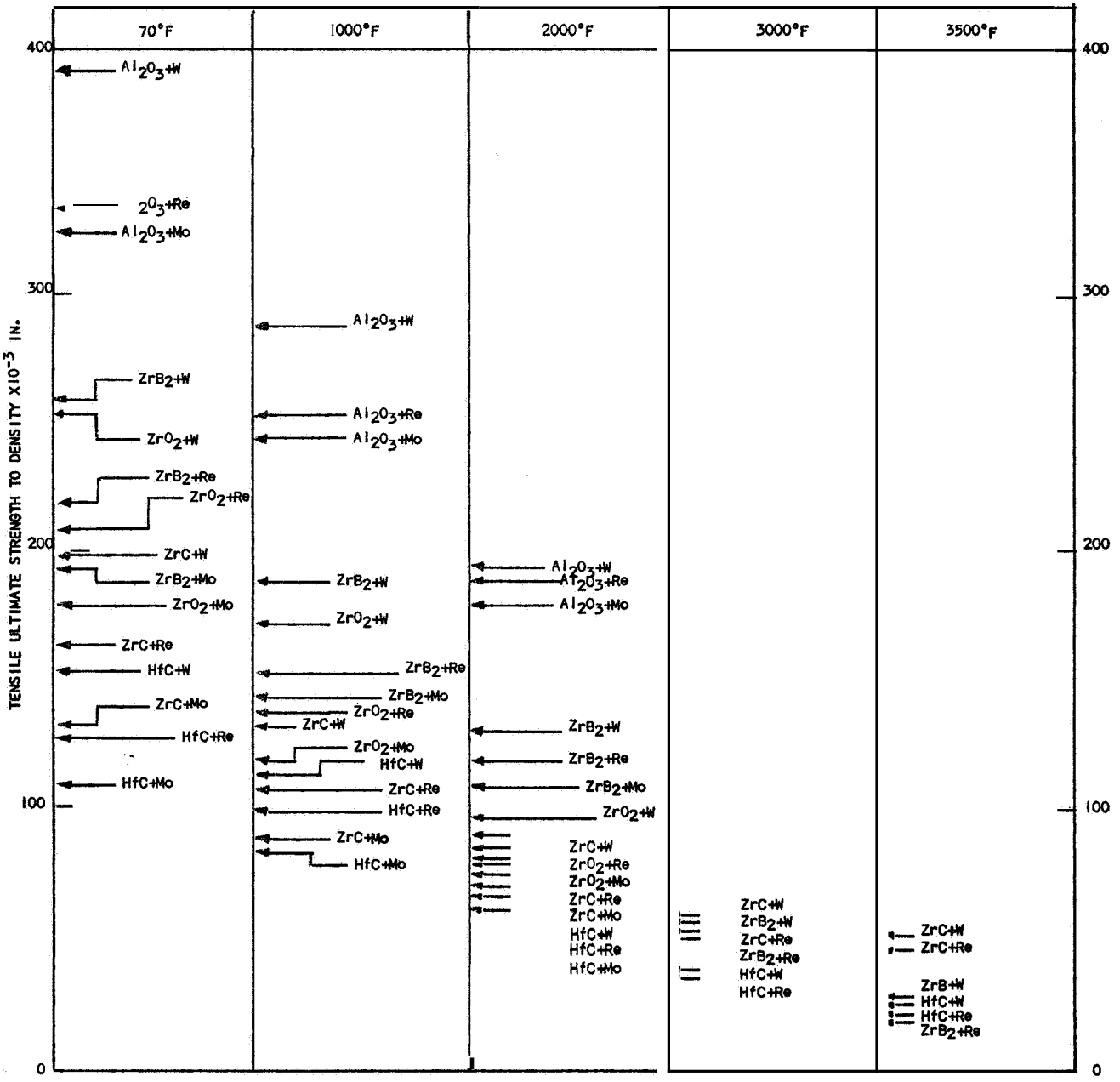

Figure 3-10. Elevated Temperature Strength/Density Rating of Prestressed Reinforced Ceramics (k_W = 0.10 Reinforcement Volume Fraction)

3.7 FURTHER CONSIDERATIONS OF FACTORS GOVERNING THE STRENGTH OF PRESTRESSED REINFORCED CERAMICS

Having selected the ceramic and reinforcement materials for the program, detailed studies were carried out on the internal stresses and strength envelopes for the two ceramic materials (zirconia and alumina) prestressed with tungsten filaments. Whereas in Section 3.6 only the ultimate strengths of composites were given, the more detailed analytical studies involved the determination of the strength envelopes for the prestressed ceramics, as well as the determination of the internal stresses in the constituents. The latter are required when investigating the effect of creep on prestress relaxation. As before, the analysis assumed elastic behavior of the constituents up to failure.

3.7.1 Internal Stresses in the Constituents

For a composite consisting of alumina reinforced with prestressed tungsten fibers, the internal stresses in the constituents are shown in Figure 3-11. The stresses are due to filament prestress and thermal effects only (no external loading). The results shown were calculated from equations given in Section 3.1, using material properties given in Figures 2-1, 2-2, 2-3 and in Table 2-2. The chemical consolidation temperature for alumina was taken as 600°F (316°C). For a given reinforcement prestress and a given temperature, the point where the "no-load failure" curve and the solid curves intersect represents the temperature at which the filaments will fail without applying any external loading to the composite.

3.7.2 Strength Envelopes for Alumina Composite

Using the equations given in Section 3.2, the strength envelope for alumina reinforced with prestressed tungsten filaments was obtained as a function of temperature and filament prestress. The results, shown in Figure 3-12, are typical and were based on the same property data of the constituents and the consolidation temperature as was referenced above. It is shown in Figure 3-12 that for any given application temperature, there is an optimum filament prestress whereby the tensile strength of a composite is a maximum. Conversely, for any given filament prestress, there is an optimum temperature at which the composite exhibits highest tensile strength. If, for a given

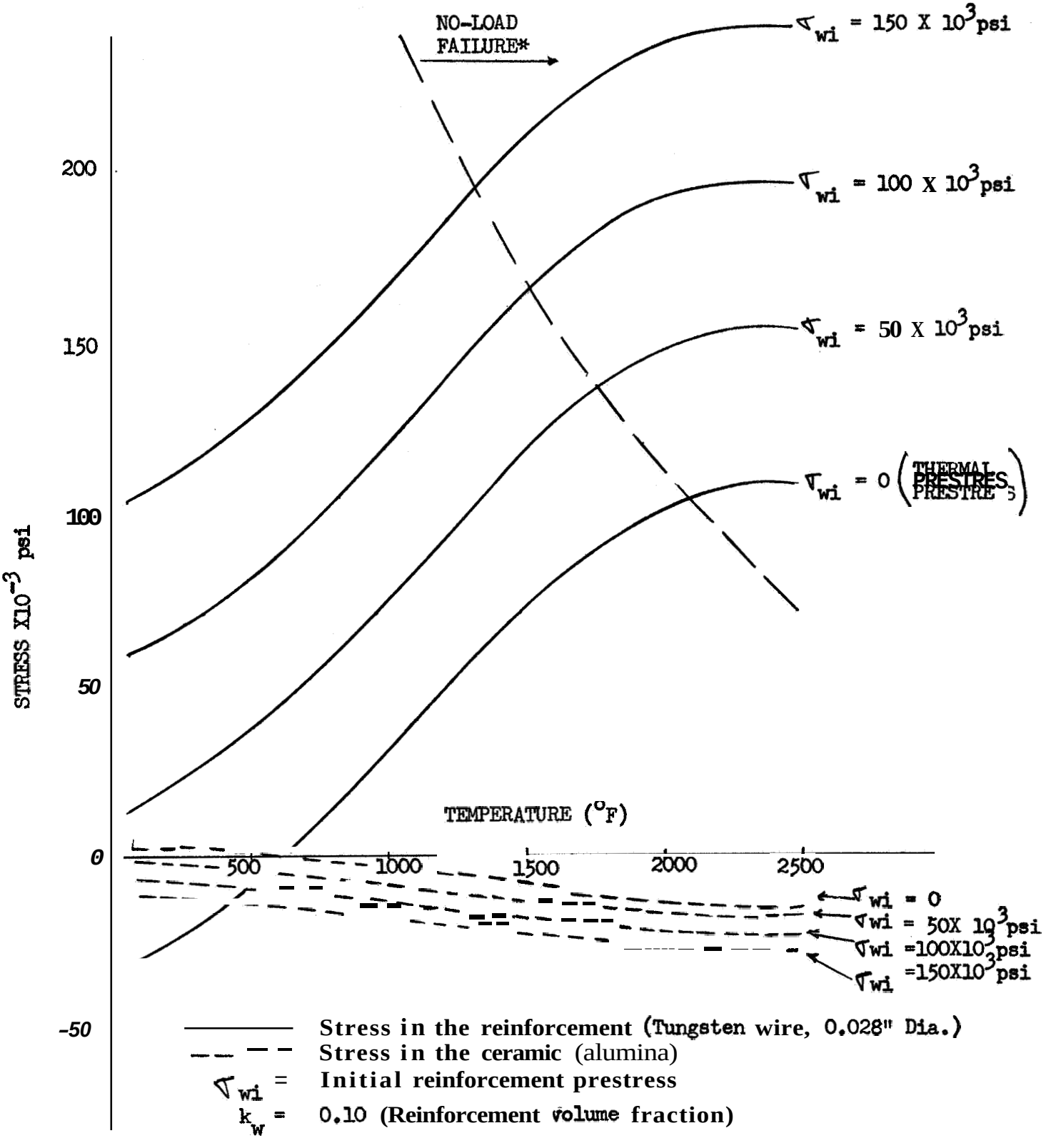

* For any given prestress the composite will fail without applying any external load.

Figure 3-11. Resultant Stresses in the Ceramic and Reinforcement Due to Mechanical and Thermal Prestress

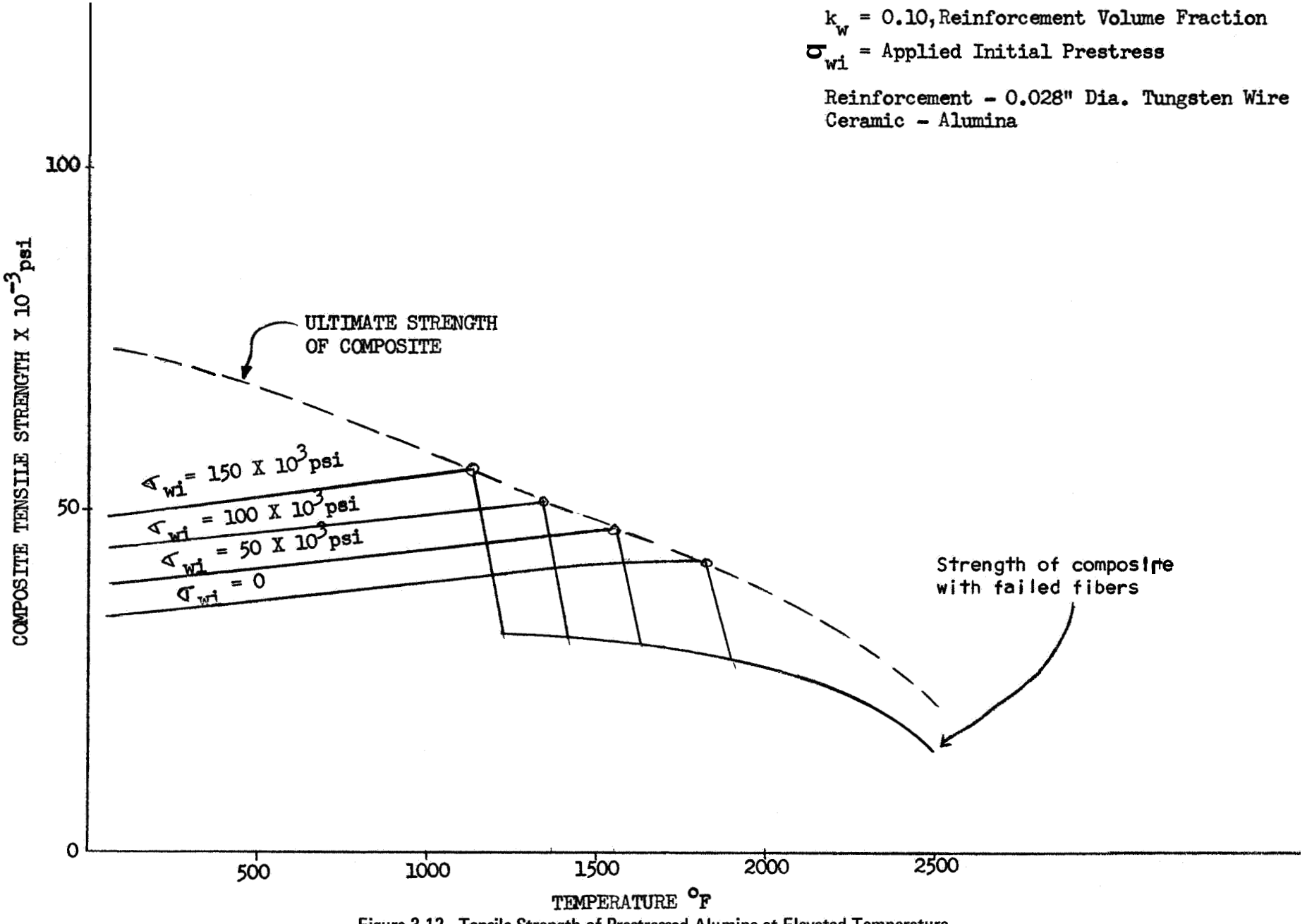

Figure 3-12. Tensile Strength of Prestressed Alumina at Elevated Temperature

filament prestress, the use temperature exceeds the optimum temperature, a sharp decrease in strength of composite occurs. For any given prestress, the relationship between the composite tensile strength and temperature is a "step-type" curve. The curve joining the maxima's represents the ultimate strength of a composite, which was mentioned in the section on trade-off studies. The shape of the strength curve is dependent on the temperature at which the ceramic consolidates, on the moduli of elasticity, tensile strengths, and coefficients of thermal expansion of the constituent materials at room and elevated temperatures, and also on the volume fraction of the reinforcement and the initial filament pretension.

3.7.3 Effect of Creep on Composite Behavior

To establish if creep in the constituents of a composite is an important problem area, studies were initiated on the effect of creep on prestress relaxation and on the overall behavior of a composite. The level of sophistication employed in these studies was similar to that used in Section 3.1.

In contrast to the usual case of creep where a given material undergoes plastic deformation under a constant load, the creep in a prestressed ceramic proceeds under gradually diminishing forces. When a ceramic is prestressed and exposed to an elevated temperature, high tensile stresses exist in the filaments while the ceramic is under a compressive state of stress (Figure 3-11). Due to creep, the ceramic will tend to undergo a negative creep strain while the reinforcement will tend to undergo a positive creep strain. The creep of the constituent materials will cause a relaxation of tensile stresses in the filaments and a decrease in compressive stresses in the ceramic.

The net creep strain of a composite may be negative or positive depending on the properties of the constituents, their creep rates, and the internal stresses in the matrix and the reinforcement. The overall creep strain of a composite, as related to properties of the constituents, is given approximately by the following expression.

$$\bar{\epsilon} \approx \frac{nkw\ \bar{\epsilon}_w - (1 - k_w)\ \bar{\epsilon}_c}{nk_w\ t\ (1 - k_w)} \qquad (3.7.3\text{-}1)$$

where $\bar{\epsilon}$ denotes creep strain of a composite, $\bar{\epsilon}_w$ and $\bar{\epsilon}_c$ denote creep strains in the reinforcement and ceramic respectively, k_w denotes the filament volume fraction, and n is the filament-to-ceramic modulus ratio, The cumulative strain in the constituents required to cause complete prestress relaxation may be readily established to be:

$$\tilde{\epsilon}_w + \tilde{\epsilon}_c = \frac{1}{E_w} \left[\sigma_{wi} + (\alpha_c - \alpha_w) \Delta T E_w \right] \qquad (3.7.3\text{-}2)$$

Some of the typical results on the required cumulative strain in the constituents to cause a complete prestress relaxation are shown in Figure 3-13. The results shown are for a composite consisting of prestressed tungsten filaments (0. 10 fiber volume fraction in an alumina matrix).

The cumulative strain required for a complete prestress relaxation is shown to increase with mechanical fiber prestress, as well as with temperature. The cumulative strains shown are for a condition whereby the stresses in the constituents relax with time. After undergoing the cumulative strains shown in Figure 3-13, the composite would behave as a reinforced material, i. e. , there would be no increase in load carrying ability due to prestress.

To obtain time-to-failure, information on the creep properties of constituents is required, that is, curves for stress vs creep strain vs temperature vs time. Unfortunately such information is not available. Some of the results reported in Reference 4 may be used to obtain a rough estimate for the minimum time-to-failure. For 5-mil diameter tungsten filaments, the stresses (extrapolated from experimental results) required to give rupture time of 1, 10, and 100 hours are shown in Table 3-1. Assuming that the data in Table 3-1 apply approximately to 0. 028-in. diameter tungsten filaments, the minimum time-to-failure may be estimated. The minimum time-to-failure is defined as the time required to cause filament rupture, assuming that the stress remains constant and is equal in magnitude to the initial stress at time t = 0. This obviously is a very conservative estimate. Thus, for a composite consisting of 0. 10 volume fraction of prestressed tungsten fibers ($\sigma_{wi} = 100 \times 10^3$ psi) in an alumina matrix, the stress in the fibers at a temperature of 1,200°F (649°C) is 136×10^3 psi (See Figure 3-11). For that temperature and stress

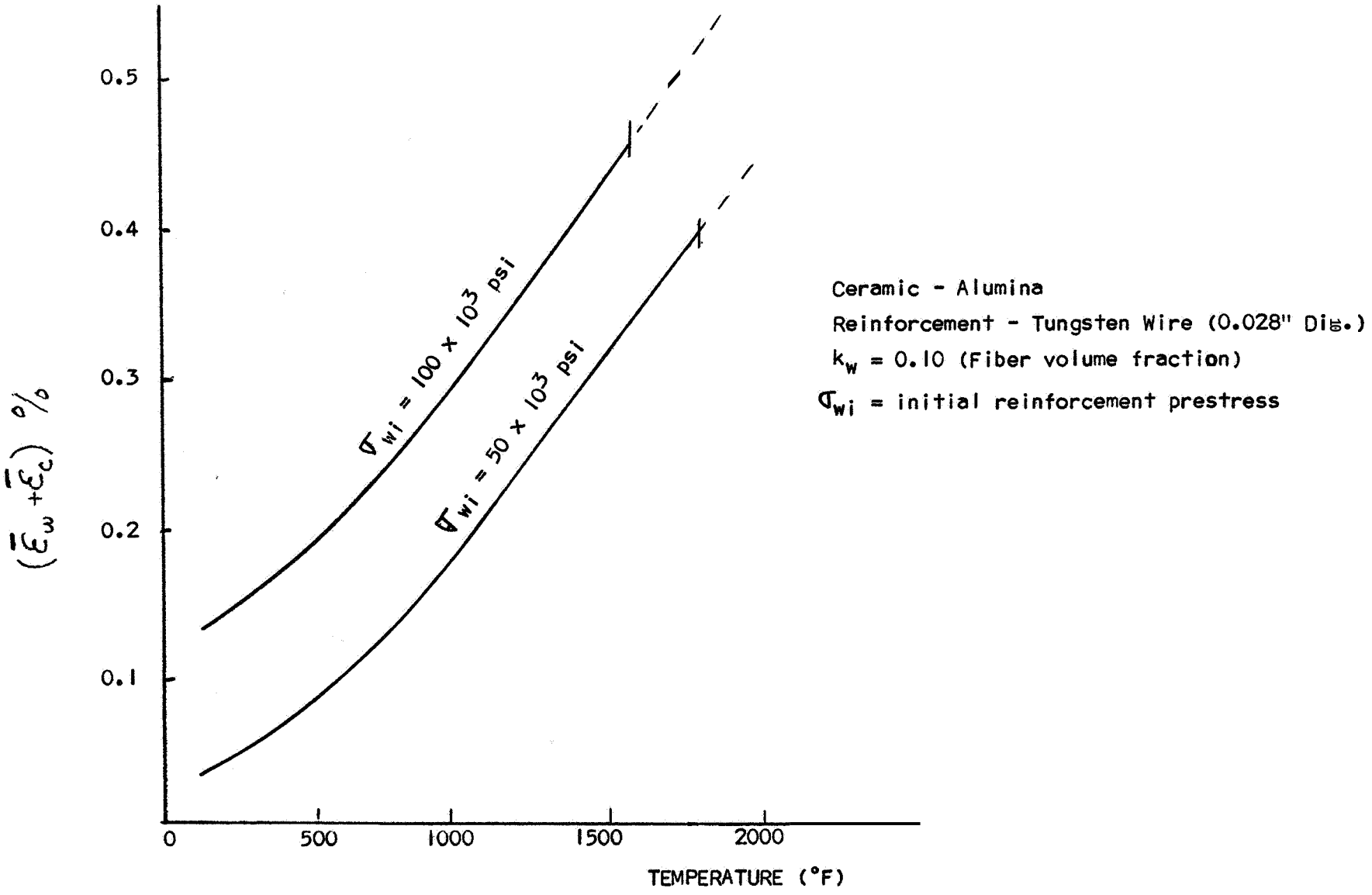

Figure 3-13. Cumulative Creep Strain for a Complete Prestress Relaxation

Table 3-1

STRESSES TO GIVE RUPTURE TIMES OF 1, 10, AND 100 HOURS FOR 5-MIL DIAMETER, AS DRAWN TUNGSTEN WIRE

Temperature °F	Stress For Rupture, psi 1 hr	10 hr	100 hr
1200	199, 100	175,000	154, 800
1500	145, 600	130, 400	116, 700
1800	116,000	104, 500	94,200
2000	88,100	73,300	61,000
2300	62, 800	49,000	38,300
2500	49,000	35,900	26,200

level, the minimum time-to-failure extrapolated from Table 3-1 is $t_{min} > 1,000$ hrs. For an identical composite ($k = 0.10$, $\sigma_{wi} = 100 \times 10^3$ psi) which is subjected to 1,500°F (816°C), the fiber stress is 162×10^3 psi whereas the minimum time-to-failure is approximately $t_{min} > 0.12$ hr, For the case when $k = 0.10$, $\sigma_{wi} = 50 \times 10^3$ psi and the composite is subjected to a temperature of 1,500°F (816°C) $t_{min} > 100$ hr. The above results indicate that for high prestress and high temperatures, creep may be a problem. Due to the lack of creep data for the constituents, a more extensive numerical investigation of this problem is not possible at the present time, Moreover, an extensive investigation of the problem is outside the scope of the present program,

As is pointed out in Reference 5, the creep of alumina is strongly influenced by the nature of the material and test variables. Minor changes in material or conditions to which they are subjected are said to have a drastic influence on the creep rates. Some additional data on creep of alumina has been found in References 6 and 7. The information contained therein is, however, for temperatures and loadings which are of no interest in the present program. As to the information on creep properties of zirconia, it is practically nil, except for a brief mention in Reference 5.

As to the rigorous analysis on prestress relaxation due to creep, various books and journals on prestressed concrete contain valuable information in this area. For example, F. Leonhardt (Reference 8), presents an extensive analytical treatment of the effects of shrinkage and creep of concrete. Methods of analysis of various degrees of complexity are presented therein, including the method proposed by Dischinger (References 9 and 10), Fritz's method (References 11 and 12), Busemann's method (References 13 and 14), as well as various other methods. For consistency with the studies on stresses in, and strength of prestressed composites, the level of sophistication and the analytical model used in the creep investigation may be similar to that used previously for investigating strength of prestressed ceramics. The simple model lends itself to a relatively simple numerical solution, provided that the creep data on the constituents is known.

3.8 REFERENCES FOR SECTION 3

1. E. Hoyer, and E, Friedrich, Beitrag zur Frage der Haftspannung in Eisenbetonbauteilen, Vol. 38, No. 6, Berlin, 1939, 11. 107-110.

2. S, P. Timoshenko, Theory of Plates and Shells, McGraw-Hill Book Co., 1940.

3. M. T. Huber, Pisma, Vol. 11, Państwowe Wydawnictwo Naukowe, Warszawa, 1956, p. 81.

4. D. L, McDanels, and R. A. Signorelli, Stress-Rupture Properties of Tungsten Wire From 1200°F to 2500°F, NASA TN D-3467, July 1966.

5. F. J. Lynch, C. G. Ruderer, and W. H. Duckworth, Engineering Properties of Ceramics - Databook to Guide Materials Selection for Structural Applications, AFML-TR-66-52, June, 1966.

6. J. A. Pask, Mechanical Properties of Ceramic Materials, Chapter 11, Mechanical Behavior of Materials at Elevated Temperatures, edited by J. E. Dorn, McGraw Hill Book Company, New York, 1961.

7. E. M. Passmore, and T. Vasilos, Creep of Dense Pure, Fine-Grained Aluminum Oxide, Journal of the American Ceramic Society, 49 (3), 1966, pp. 166-168.

8. F. Leonhardt, Prestressed Concrete - Design and Construction, Wilhelm Ernst and Sohn, Berlin, 1964, pp. 401-448.

9. F. Dischinger, Untersuchungen uber die Knicksicherheit, die elastische Verformung und das Kriechen des Betons bei Bogenbrucken, Bauingenieur, 18 (1937) No. 33/34, pp. 487-520; No. 35/36, pp. 539-552; No. 39/40, pp. 595-621.

10. F. Dischinger, Elastische und Plastische Verformung der Eisenbeton-tragwerke, Bauingenieur 20 (1939) No. 5/6, pp. 53-63; No. 21/22, pp. 286-294; No. 31/32, pp. 426-437; No. 47/48, pp. 563-572.

11. B. Fritz, Vereinfachtes Berechnungsverfahren für Stahlträger mit einer Botondruckplatte, Bautechnik 27 (1950) No. 2, pp. 39-42.

12. B. Fritz, Gebrauchsfertige Berechnungsformeln für Freiaufliegende Spannbetontragwerke, Osterr, Bauzeitschrift, 1954, No. 8/9.

13. R. Busemann, Kriechberechnung von Verbundträgern unter Benutzung von zwie Kriechfasern, Bauingenieur 25 (1950), No. 11, pp. 418-420.

14. R. Busemann, Anwendung des Kriechfaserverfahrens bei statisch unbestimmten Systemen mit veranderlichen Verbundguerschnitten, Stahlbau 23, (1954), No. 9, pp. 201-206.

Section 4
MATERIALS SELECTION AND MATRIX DEVELOPMENT

As discussed in Section 1.2, alumina and zirconia were selected as the final matrixes, on the basis of trade-off studies and experimental work. The strength of the castable, chemically-consolidated zirconia at room temperature was increased consistent with good casting practices. Alumina exhibited acceptable flexural and tensile strength in the unstressed state. Prestressed flexural specimens developed cracks during processing and as a consequence testing was not considered feasible. The obtainment of tensile data on prestressed alumina was not contractually required.

4.1 OPTIMIZATION AND CHARACTERIZATION OF ZIRCONIA MATRIX

Strength improvement of the zirconia matrix was accomplished by study of particle size distribution, quantity of additives to permit casting of the specimens, and subsequent curing. Attempts to decrease the average pore size in order to obtain equal distribution of applied loads were successful. However, it was found that zirconia with reduced pore size did not exhibit increased flexural strength. Characterization studies included stoichiometry, differential and thermal gravimetric analysis, X-ray diffraction, and chemical composition.

Zirconia has been chemically consolidated with monofluorophosphoric acid (Reference 16) to form hard, dense bodies which exhibited excellent thermal shock resistance. Work performed recently by Bremser and Nelson (Reference 17) has shown that the zirconium pyrophosphate, the bonding medium (Reference 18), is converted to a double phosphate of calcium and zirconium after heating to 1,200°C (2,192°F). In addition, the phosphate-bonded, calcia-stabilized zirconia is converted from the cubic to the monoclinic form after heating at 1,240°C (2,264°F).

The existance of several forms of zirconium phosphate is known (Reference 19). Zirconium pyrophosphate is stable to 1,380°C (2,516°F). The zirconyl pyrophosphate (Equation 4.1-1) formed above this temperature is stable to 1,600°C (2,912°F).

$$2\,ZrP_2O_7 \rightarrow (ZrO)_2\,P_2O_7 + P_2O_5 \qquad (4.1\text{-}1)$$

4. 1. 1 Chemical Reactions for Consolidation

The chemical consolidation of ZrO_2 is produced by reaction with monofluorophosphoric acid (H_2PO_3F). The reaction, as determined by differential thermal analysis and substantiated by X-ray diffraction studies, consists essentially of two phases. Zirconium tetrafluoride (ZrF_4) is formed on the surface of each particle of ZrO_2 accompanied by a subsequent reaction with the phosphate radical to produce the bonding material, zirconium pyrophosphate (ZrP_2O_7).

Although the formula for monofluorophosphoric acid is represented as H_2PO_3F, the as-received acid consists of 70% by weight of H_2PO_3F and 30% by weight of equimolar solutions of difluorophosphoric acid (HPO_2F_2) and orthophosphoric acid (H_3PO_4). The reaction with zirconia is shown in Equation 4. 1.1-1 .

$$1.4\,H_2PO_3F + 0.3\,HPO_2F_2 + 0.3H_3PO_4$$

$$+ ZrO_2 \rightarrow ZrP_2O_7 + 2HF + H_2O \qquad (4.1.1\text{-}1)$$

The stepwise reaction, as determined by differential thermal analysis, is shown in Equations 4.4. 1-2 through 4.4. 1-8. The initial reaction is the hydrolysis of the acid.

$$2.8\,H_2PO_2F_2 + 2.8\,H_2O \rightarrow 2.8\,HF + 2.8\,H_3PO_4 \qquad (4.1.1\text{-}2)$$

$$0.6\ HPO_2F_2 + 1.2\ H_2O \rightarrow 1.2\ HF + 0.6\ H_3PO_4 \qquad (4.1.1\text{-}3)$$

$$0.6\ H_3PO_4 = 0.6\ H_3PO_4 \qquad (4.1.1\text{-}4)$$

$$2.8\ H_2PO_3F + 0.6\ HPO_2F_2 + 0.6\ H_3PO_4 + 4H_2O = 4.0\ HF + 4.0\ H_3PO_4 \qquad (4.1.1\text{-}5)$$

The H_3PO_4 dissociates to form $H_4P_2O_7$, as shown in Equation 4.1.1-6.

$$4H_3PO_4 = 2H_4P_2O_7 + 2H_2O \qquad (4.1.1\text{-}6)$$

The HF, formed from the hydrolysis of the fluorophosphate acids, reacts with ZrO_2 to form ZrF_4, as shown in Equation 4.1.1-7.

$$4HF + ZrO_2 \rightarrow ZrF_4 + 2H_2O \qquad (4.1.1\text{-}7)$$

Only one mole of the $H_4P_2O_7$ is required to react with the one mole of ZrF_4 formed from the reactions of zirconia with the four moles of HF as shown in Equation 4.1.1-8. The excess HF formed upon reaction of ZrF_4 with the $H_4P_2O_7$ is available for further reaction with ZrO_2, and consequently to react with the additional moles of $H_4P_2O_7$. The excess HF is vaporized during the processing of 500° to 600°F (260° to 316°C) after all of the available $H_4P_2O_7$ is reacted.

$$ZrF_4 + H_4P_2O_7 \rightarrow 4HF + Zr P_2O_7 \qquad (4.1.1\text{-}8)$$

The reaction of ZrO_2 with H_2PO_3F is extremely rapid at room temperature. To allow a reasonable time for placement of the matrix in large parts, ammonium dihydrogen phosphate ($NH_4H_2PO_4$) is used as a retarder. The simplified reaction is shown in Equation 4.1.1-9.

$$H_2PO_3F + NH_4H_2PO_4 + ZrO_2 \rightarrow ZrP_2O_7 + HF + NH_3 + 2H_2O \qquad (4.1.1\text{-}9)$$

The validity of the stepwise reaction was verified by promoting a chemical bond for ZrO_2 by exposure to HF and a subsequent reaction with a phosphate radical source as shown in Equations 4.1.1-10 and 4.1.1-11.

$$4HF + ZrO_2 \rightarrow ZrF_4 + 2H_2O \qquad (4.1.1\text{-}10)$$

$$ZrF_4 + 2NH_4H_2PO_4 \rightarrow ZrP_2O_7 + 4HF + 2NH_3 + H_2O \qquad (4.1.1\text{-}11)$$

A typical differential thermal analysis thermogram of a mixture of H_2PO_3F and ZrO_2 is shown in Figure 4-1. The endothermic peak initiating at 75°C (167°F) is consistent with those occurring for mixtures of HF and ZrO_2. This peak is attributed to the volatilization of HF and/or water vapor. The endothermic peak occurring at approximately 100°C (212°F) represents the conversion of orthophosphoric acid (H_3PO_4) to pyrophosphoric acid ($H_4P_2O_7$). The intense exothermic reaction at 150°C (302°F) indicates the formation of ZrP_2O_7 and $ZrF_4 \cdot 3H_2O$. The presence of these compounds has been substantiated by X-ray diffraction studies, thermogravimetric analysis, and stoichiometric studies. The endothermic peak occurring at approximately 230°C (446°F) indicates the conversion of $ZrF_4 \cdot 3H_2O$ to $ZrF_4 \cdot H_2O$. The endothermic peak occurring in the neighborhood of 275°C (526°F) indicates the decomposition of $ZrF_4 \cdot H_2O$.

4.1.2 Development of Maximum Strength

The rate of reaction and the strength of the ceramic after processing is a direct function of the particle size distribution of the matrix material. Flexural strength of chemically consolidated ZrO_2 is increased from 3,000 psi to 4,300 psi as shown in Figure 4-2 by optimizing the particle size distribution. Further studies were undertaken to increase the strength by variation of the concentration of reactants. The systems selected for further studies, based on the results shown in Figure 4-2, were D, H, L, R, and S. It was decided to keep the retarder ($NH_4H_2PO_4$) constant and vary the binder (H_2PO_3F). The results of this study revealed that with the acid variation, the strength was increased to over 5,000 psi with the "S" system as shown in Figure 4-3. The retarder was varied using the "S" system, and the

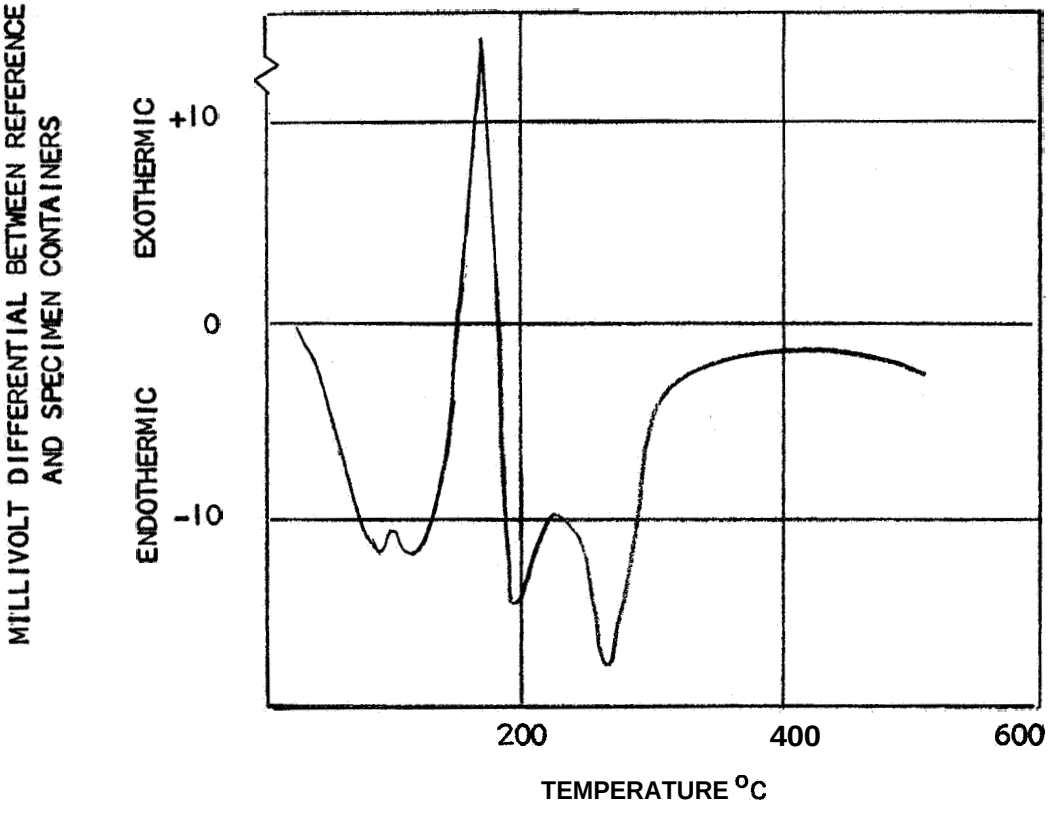

Figure 4-1. Differential Thermal Analysis of $H_2PO_3F + ZrO_2$

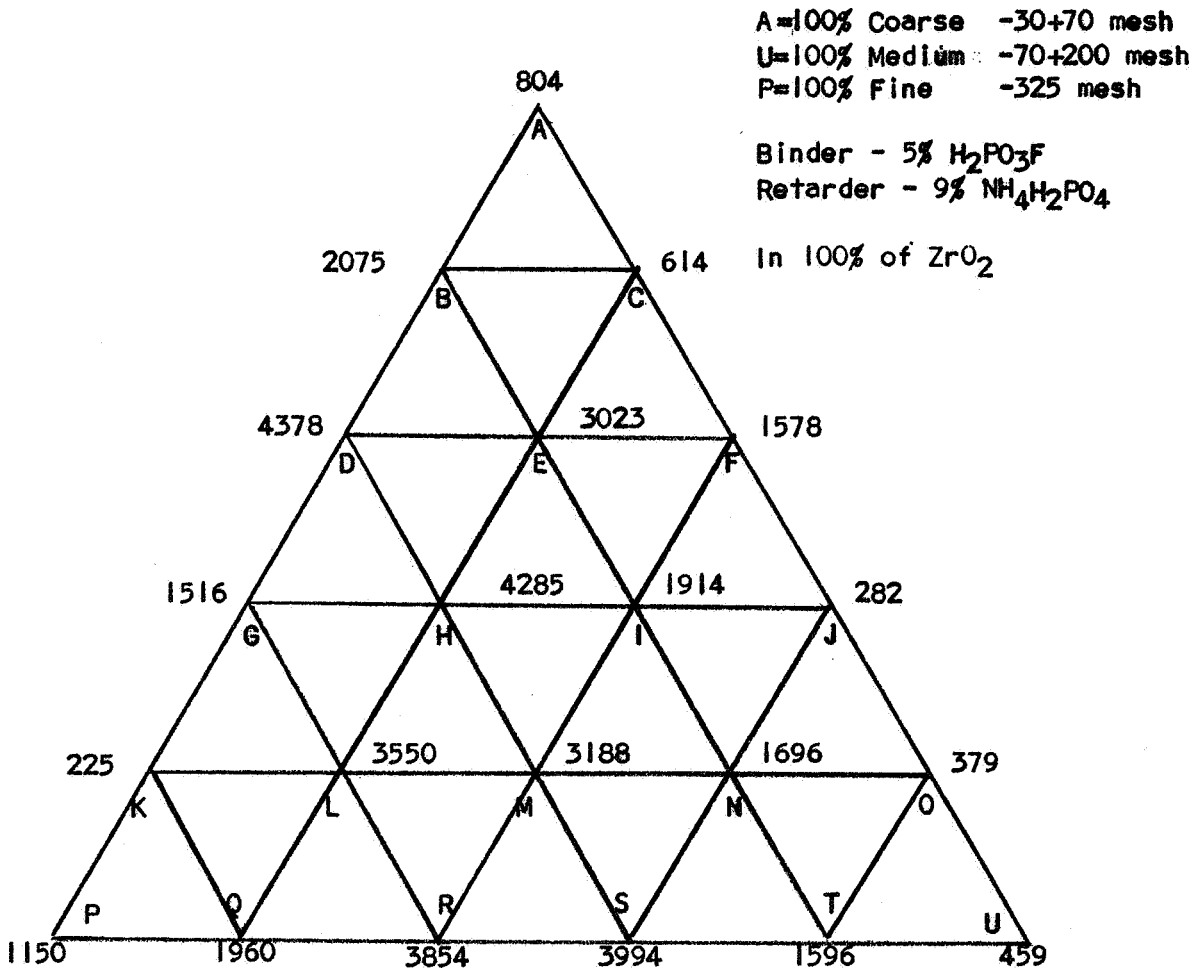

(1) Average of five values (psi) at each mixture.

Figure 4-2. Flexural Strength(1) of Chemically Consolidated Zirconia as a Function of Particle Size Distribution

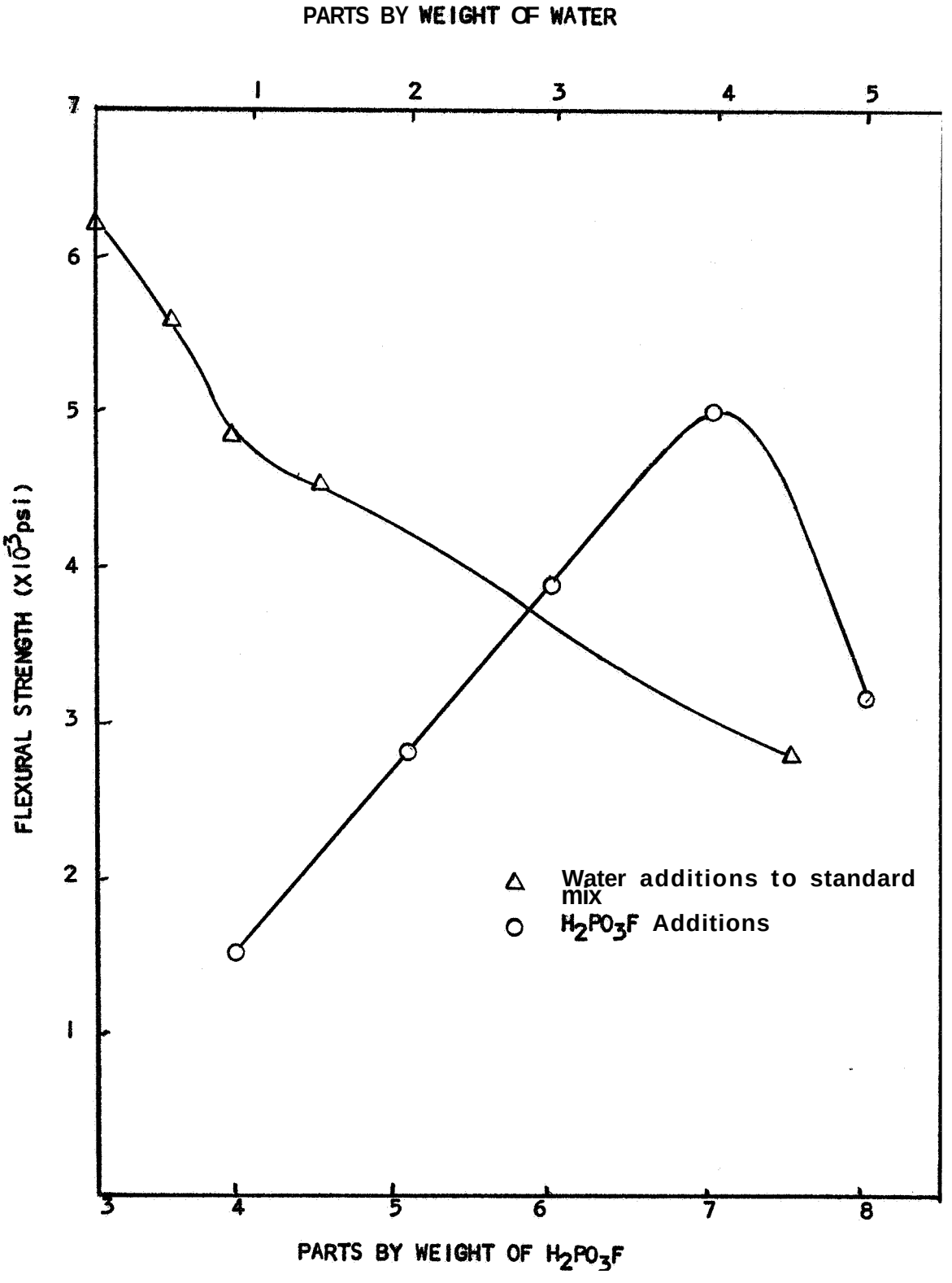

Figure 4-3. Flexural Strength of Chemically Consolidated Zirconia as a Function of H_2PO_3F and Water Contents

strength was increased to 6,200 psi. The "S" particle size distribution, using 7 parts by weight of H_2PO_3F and 6 parts by weight $NH_4H_2PO_4$, was selected as the standard mix. It was determined that a lower viscosity mix was required for satisfactory distribution of the mix around the wires used for prestressing. As it was determined that the addition of an excess of binder would not produce the desired viscosity, a series of chemically consolidated castable ZrO_2 specimens were prepared by varying the quantity of added water. It was conclusively shown that the addition of water to the standard mix reduced the flexural strength. It was determined that 2 weight percent of water added to the standard mix lowered the viscosity but when cured had a tendency to bloat or expand slightly leaving larger voids in the matrix, which probably accounts for the loss of strength.

A series of specimens were prepared using **3** weight percent isopropyl alcohol $[(CH_3)CHOH,]$ as a substitution material of low surface tension for water which would allow the gases to escape more readily, thus reducing bloating, These specimens also exhibited low viscosity, although bloating did not occur. However, the mixture set up rapidly; and when making a large number of specimens, it tended to set up slightly during casting.

A mixture was prepared composed of the standard mix with 2 weight percent $(CH_3)CHOH$ plus one weight percent water. This formulation exhibited excellent flow characteristics and a reasonable shelf life for casting a large volume of material. Figures 4-4 and 4-5 are macrographs of a chemically consolidated ZrO_2 matrix with 3 weight percent water and 2 weight percent (CH_3) CHOH with 1 weight percent water, respectively. It may be seen that the pores are smaller and fewer in number in the mix containing alcohol.

Flexural tests on the zirconia matrix revealed abnormally low (1,800 psi) strength values, indicating that the alcohol used in the formulation had adversely affected the strength of the mix. This finding necessitated a re-evaluation of the castable formulation to provide a castable mix possessing good flow characteristics and acceptable flexural strength. Flexural test specimens were

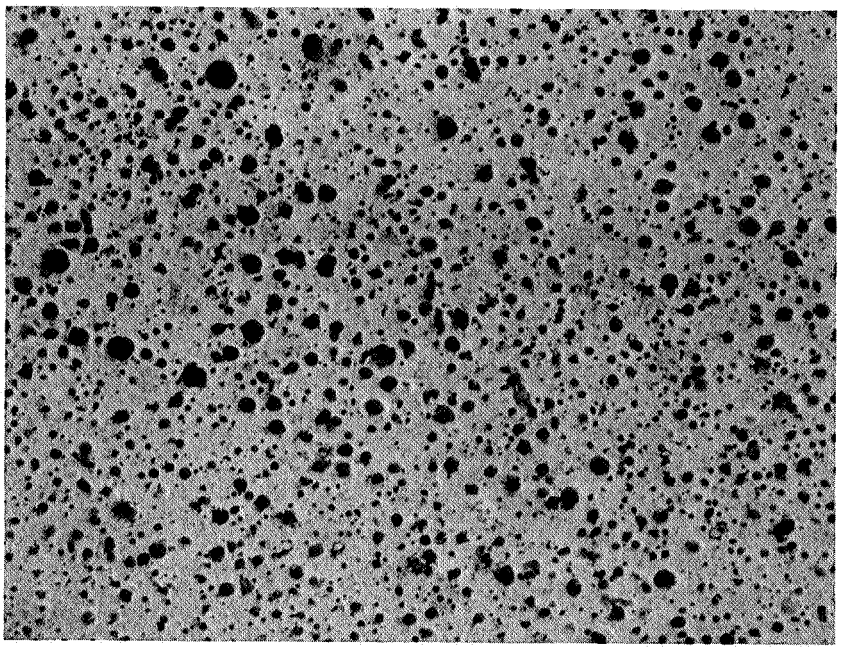

Mag. 7X

Figure 44. ZrO_2 Matrix with 3 Weight Percent Water Added

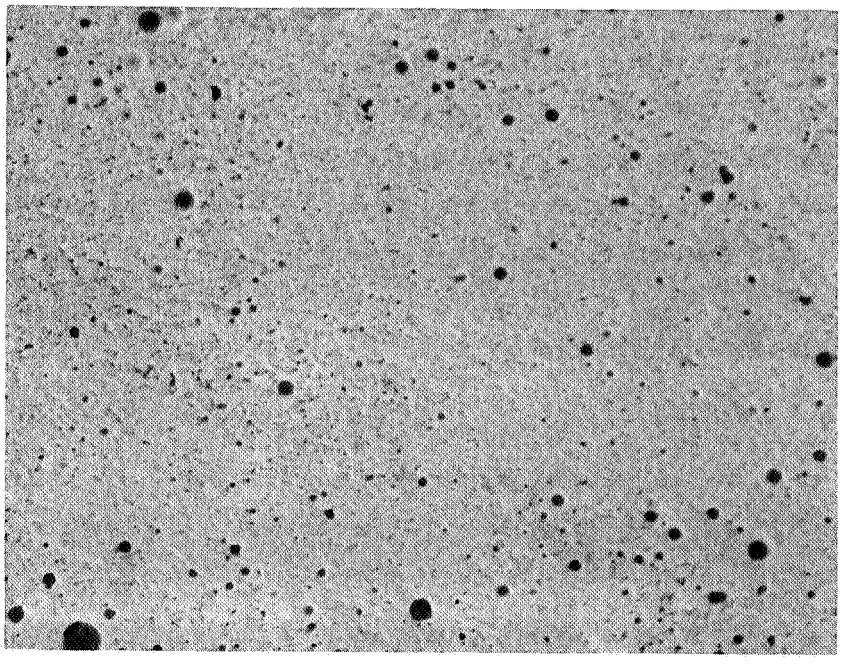

Mag. 7X

Figure 4-5. ZrO_2 Matrix with 2 Weight Percent (CH_3) CHOH + 1 Weight Percent Water Added

prepared from a series of formulations which incorporated variations in retarder content, acid content, and processing methods. The results of the study are summarized in Table 4-1. These test specimens were for the determination of relative strengths and were therefore not precision ground. On the basis of these results, zirconia Mix No. 4 was selected as the standard for future matrixes and prestressing evaluations for this program. Further tests were conducted to determine the effect of specimen orientation in the test fixture and cure treatment upon the flexural strength of the specimens. These results are summarized in Table 4-2. On the basis of these results, it was decided to (1) cure all specimens to 600°F (316°C) and (2) grind all surfaces to eliminate possible skin effects.

4.1.3 Characterization of Zirconia

Raw material characterization is an important part of any material development program. Reproducibility of strength properties of brittle materials is difficult to obtain even when close control of raw materials and processing techniques are employed. Steps were taken to characterize the matrix materials. The nominal formulation for chemically consolidated zirconia consists of 60 parts by weight of -60 t 200 mesh and 40 parts by weight of -325 mesh of fused, calcia-stabilized zirconia supplied by the Norton Co. Particle-size count, true density, and calcia content for -325 mesh Norton ZrO_2 was determined previously by Douglas and a description of the procedures used and test results are presented. The particle-size count on the -60 + 200 mesh was determined in the present program.

4.1.3.1 Particle-Size and Density

-60 t 200 mesh - ZrO_2

Three batches of 1,000 gms each were screened using U.S. Standard Sieves, Nos, 60, 80, 100, 120, 140 and 200. The average quantity of material between the particle sizes indicated are shown in Table 4-3.

Table 4-1

FLEXURAL STRENGTH OF VARIOUS CASTABLE ZIRCONIA MIXES AT ROOM TEMPERATURE

Mix Number	Formulation[1] ZrO_2 -60 +200 Mesh	ZrO_2 -325 Mesh	$NH_4H_2PO_4$	H_2PO_3F	H_2O	Process[2] Used	No. of Specimens	Flexural Strength (psi) Max	Min	Average
1	60	40	3	7	7	DB	4	2180	1820	1920
						BM	4	1740	1570	1620
2	60	40	6			DB	4	4860	3000	3520
						BM	4	3000	2790	2900
3	60	40	9	7	2	DB	4	4260	3780	4040
3						BM	4	3810	3390	3510
						DB and V	6	4410	3830	4050
4	60	40	0	16	0	DB	6	5180	3900	4310

(1) Parts by weight
(2) DB = blended for 1/2 hour
BM = ball milled for 1/2 hour
V = cured in vacuum bag

Table 4-2

FLEXURAL STRENGTH[1] OF ZIRCONIA SPECIMENS AS A FUNCTION OF SPECIMEN ORIENTATION AND CURE TREATMENT

Specimen No.	Room Temp. Flexure Strength (psi)	Average psi	Orientation and Treatment
1	2740		As-cast surface in
2	2950	2760	tension, cured to
3	2585		450° (232°C)
4	4072		Ground surface in
5	3272		tension cured to
6	3260	3120	450°F (232°C)
7	2946		
8	2050		
9	4272		Ground surface in
10	4750		tension, cured to
11	3890	4360	600°F (316°C)
12	4439		
13	4465		

(1) All bars made from same batch and cured to 450°F (232°C) except where noted.

Note: All specimens were 0.3" thick, 1" wide and loaded on a 4" span using 3 point loading.

Table 4-3

PARTICLE SIZE ANALYSIS FOR -60 + 200 MESH ZrO_2

Particle Size Range, Microns	% of Count Average of 3 Batches
>250	0
177 to 250	0
149 to 177	5.7
125 to 149	35.5
105 to 125	14.5
74 to 105	41.5
<74	3.0

-325 mesh ZrO_2

Since -325 mesh zirconia powders were smaller than available sieve sizes, another method for particle-size count was employed. Samples from each of three, 50-lb batches were analyzed microscopically. This technique involves the suspension of the particles in a dense liquid with low surface tension (Freon). The suspension is then poured onto a Millipore filter calibrated with a grid. The particles are then physically counted by size using a microscope. The average particle sizes of the three batches are shown in Table 4-4.

Table 4-4
PARTICLE SIZE ANALYSIS FOR -325 MESH ZrO_2

Particle Size Range, Microns	% of Count Average of 3 Batches
>25	0.6
10 to 25	4.8
5 to 10	29.4
<5	65.1

True Density Pycnometer Method

Zirconia density of three independent measurements yielded the values 5.4, 5.5, and 5.6 gm/cc or an average of 5.5 gm/cc. Since this value is the true density of the -325 mesh ZrO_2, the same general values would be expected for the -60 t 200 mesh ZrO_2.

The true density values of the zirconia, reacted with 16 parts of H_2PO_3F, was determined as 4.86 gm/cm^3. As this value was much lower than the true density of the unreacted zirconia, the theoretical density of the reacted zirconia was determined. The calculated theoretical density was determined as 4.84 gm/cm^3 by the following reaction

$$ZrO_2 + 2H_2PO_3F \rightarrow ZrP_2O_7 + H_2O\uparrow + 2HF\uparrow \qquad (4.1.3.1\text{-}1)$$

One hundred grams of ZrO_2, reacted with 16 grams of H_2PO_3F, produces 21.2 grains of ZrP_2O_7 and 90.2 grams of unreacted ZrO_2 of 19% ZrP_2O_7 and 81% ZrO_2. Using 5.5 gm/cm^3 as the density of ZrO_2 and 3.2 gm/cm^3 as the density of ZrP_2O, the theoretical density of the remaining material is 4.84 gm/cm^3. The average bulk density of the chemically consolidated zirconia matrix was determined to be 3.81 gm/cc (0.137 $lb/in.^3$) as determined by ASTM C-20.

4.1.3.2 Calcia Determination

The amount of calcia present in the zirconia powder has a decided effect on the strength and expansion of sintered or chemically consolidated zirconia bodies, Calcia stabilized zirconia, without consolidation additives, does not undergo an allotropic transformation as it has been stabilized in the cubic form. In order to help characterize the material, the weight percent of calcia present was determined.

An X-ray spectrograph sample was prepared to determine the weight by percent of calcia present in the powder (-325 mesh powders were used for the determinations). Synthetic standards were prepared in the following manner. Calculated amounts of calcium sulfate dihydrate were weighed and mixed with sufficient zirconium sulfate to produce a 1.000-gm sample, Three standards were prepared containing 1.00%, 3.00%, and 5.00% calcium, The standards were mixed with 1,500 mg. of lithium tetraborate, pelletized and analyzed.

The goniometer was positioned at 29° 28 Bragg angle corresponding to the K.C. line of calcium, and the intensities were measured for the standard. The chromium target tube, a standard analyzing crystal (PET), and a helium path were used during all measurements. Three, 100-sec counts were taken for each standard. Intensities were plotted against calcium content. The sample was drawn from this blend for analysis. This sample was mixed with 1,500 mg. of lithium tetraborate, pelletized and analyzed in triplicate as previously described.

The weight percent of calcium was determined to be 1.6 ±0.1%. This corresponds to 2.24 weight percent of calcia. The manufacturer's nominal composition is listed as 3.6% to 4.3% of calcia by weight; however, in written communication, the manufacturer stated it was not unusual to have batches of their material with lower calcia contents.

4.2 DEVELOPMENT OF ZIRCONIUM DIBORIDE MATRIX

Zirconium diboride is a very promising matrix material. Preliminary work showed that ZrB_2 powders could be consolidated chemically. The basic material has a melting point of over 5,400°F (2,982°C), low density, good strength retention with temperature, and excellent oxidation resistance to 2,000°F (1,093°C). In addition, ZrB_2 has a high thermal diffusivity.

Work done showed that ZrB_2 could be consolidated chemically using H_2PO_3F and a low temperature cure. Three processing techniques were used.

1. A mixture of 5 parts H_2PO_3F and 100 parts -325 mesh ZrB_2 powder was pre-cured at 300°F (149°C) for 1/2-hour under 16,000 psi pressure and cured at 400°F (204°C) for one hour at ambient pressure.
2. A mixture of 6 parts H_2PO_3F and 100 parts -325 mesh ZrB_2 powder was pressed at room temperature under 16,000 psi and cured at 400°F (204°C) for one hour at ambient pressure.
3. A mixture of 8 parts H_2PO_3F and 100 parts -325 mesh ZrB_2 powders was vibratory cast and cured at 400°F (204°C) for one hour at ambient pressure,

All three processes produced good bonding between particles. The first process resulted in the highest density body, The reaction of the acid on the fine powders was associated with a high degree of gas evolution, probably HF, which produces a foam structure when unrestrained, The large evolution of gas was not surprising, considering the large surface area of the powders entering into the reaction. Larger size particles are necessary for blending

with finer particles to obtain close-packed, high-strength bodies. Bodies were made of proper quantities of large and fine particles to minimize the foaming tendencies of cast bodies.

4.2.1 Chemical Reaction for Consolidation

The reactions occurring for ZrB_2 consolidated with H_2PO_3F were found to be similar to the overall reactions previously established for ZrO_2 consolidated by H_2PO_3F. The ZrB_2 reacts with the fluoride component of H_2PO_3F to form $ZrF_4 \cdot H_2O$, an intermediate reaction product, which in turn reacts with available phosphate to form ZrP_2O_7, the probable bond medium. These findings were obtained by means of X-ray diffraction, differential thermal analysis, and thermogravimetric analysis studies of reactant materials. A limited study of the gaseous reaction products by means of infrared spectrographic analysis indicated the presence of boron trifluoride (BF_3).

4.2.2 Differential Thermal Analysis

Differential thermal analysis studies were conducted for the reaction of ZrB_2 and H_2PO_3F. The overall reaction of ZrB_2 with H_2PO_3F was found to be similar to a series of reactions occurring between ZrB_2 and mixtures of HF and H_3PO_4.

A Robert L. Stone Differential Thermal Analysis apparatus was used in this study, utilizing a heating rate of approximately 8°C/min. The thermogram for the reaction of ZrB_2 with H_2PO_3F is shown in Figure 4-6. Since the compound H_2PO_3F behaves in the manner as a mixture of HF and H_3PO_4, a thermogram (Figure 4-7) was also obtained for ZrB_2 treated with 49% HF, dried, and then reacted with H_3PO_4. The thermogram obtained for the latter reaction is similar to that of the reaction indicated in Figure 4-6 for ZrB_2 with H_2PO_3F. Thermograms were also obtained for reactions occurring between ZrB_2 plus HF and ZrB_2 plus H_3PO_4 (Figures 4-6 and 4-7). The strong endothermic peak shown in Figure 4-6, occurring at approximately 300°C (572°F) for the reaction occurring between ZrB_2 plus HF, would account for the endothermic region at approximately 300°C (572°F) for the

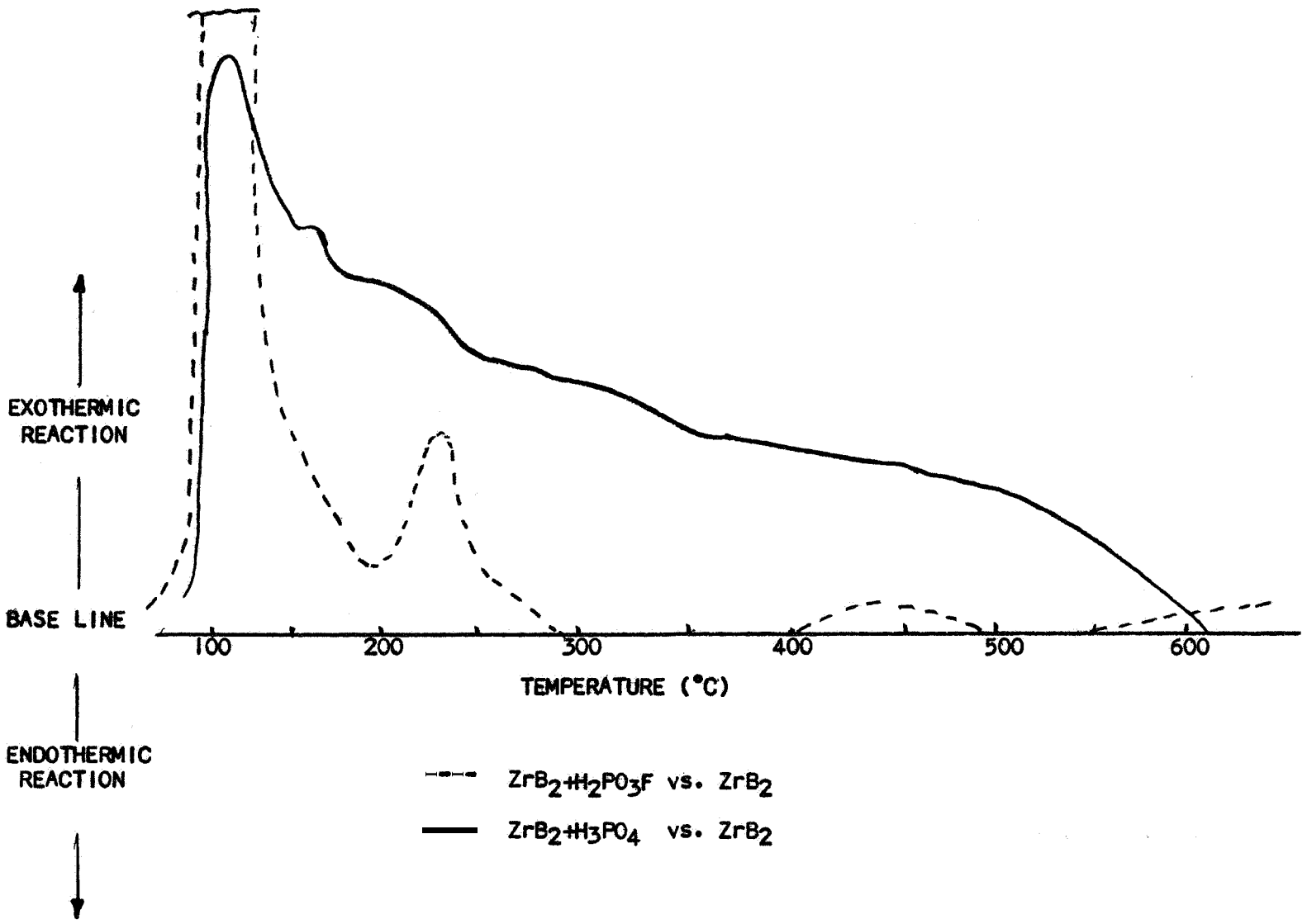

Figure 4-6. Differential Thermal Analysis

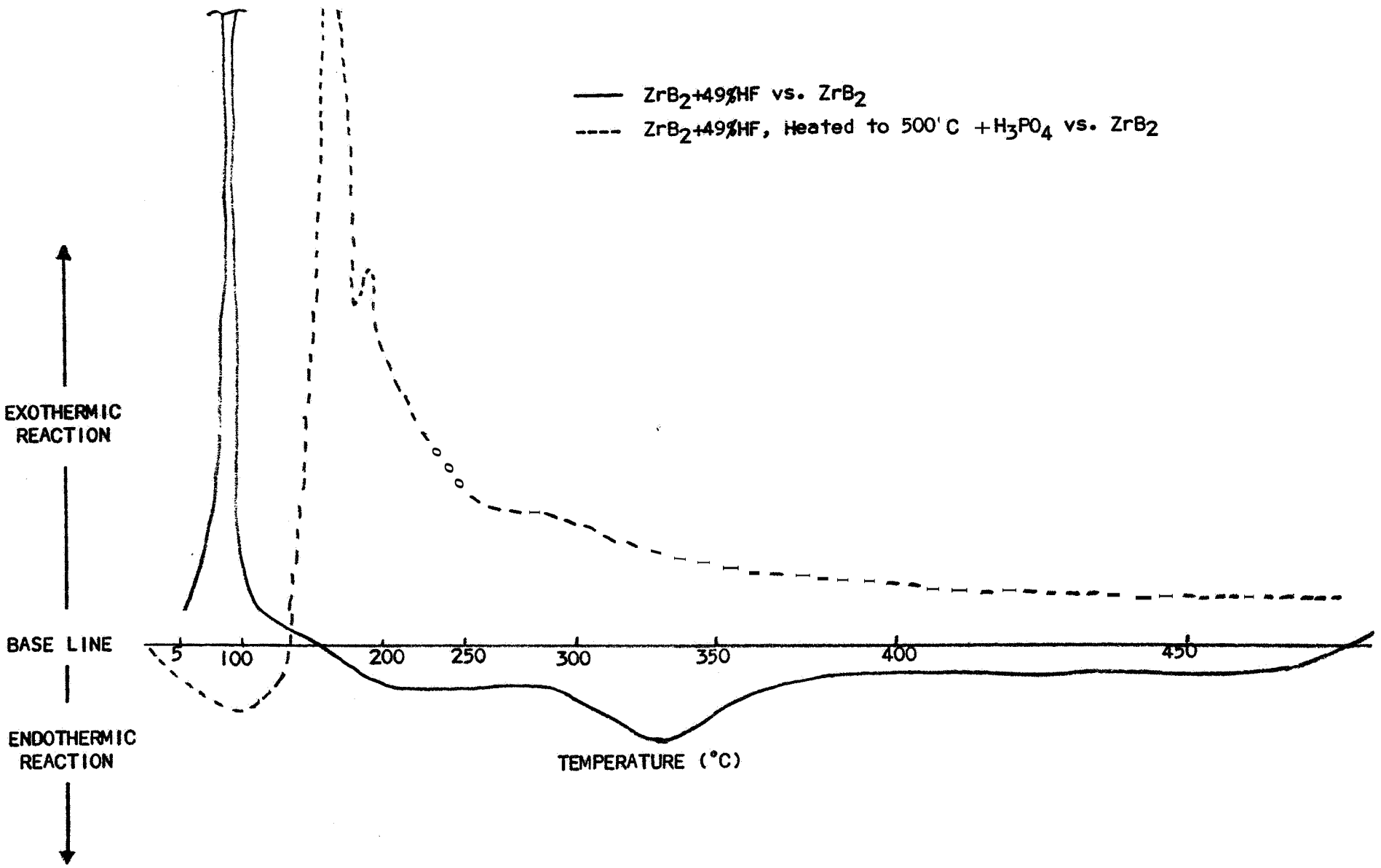

Figure 4-7. Differential Thermal Analysis

ZrB_2 plus H_2PO_3F reaction. The thermogram shown in Figure 4-6 for the ZrB_2 plus H_2PO_4 reaction indicates an exothermic peak at approximately 100°C (212°F), an exothermic peak at approximately 150°C (302°F), and a large, but gradually declining exothermic reaction curve to 600°C (1,112°F). The curves in Figure 4-6 bear a close resemblance, as an exothermic peak occurs at approximately 200°C (412°F), and a large, but gradually declining exothermic curve to 600°C (1,112°F).

4.2.3 Thermogravimetric Analysis

Thermogravimetric analyses were conducted in an attempt to determine the stoichiometry for the reaction between HF and the zirconium in ZrB_2. The studies revealed that the zirconium reacts with HF to form $ZrF_4 \cdot H_2O$ and gaseous reaction product material, The quantity of $ZrF_4 \cdot H_2O$ produced upon reacting varying quantities of HF and ZrB_2 was less than theoretically predicted.

In order to demonstrate that the experimental techniques were adequate, the first series of studies were concerned with thermogravimetric analyses for the ZrO_2 plus HF system whose stoichiometry had been established. A series of mixtures of ZrO_2 plus 49% HF were prepared, reacted by blending, and dried to constant weight at 170°C (338°F). Figure 4-8 is a plot of the weight of product/mole ZrO_2 versus the moles HF/mole ZrO_2. The experimental data are in complete agreement with the theoretical values for the $ZrF_4 \cdot H_2O$ yield. X-ray analysis of the reaction product material revealed the presence of only $ZrF_4 \cdot H_2O$.

A second series of reactions were conducted in a similar manner for mixtures of ZrB_2 plus 49% HF. Figure 4-8 also shows a plot for the weight of product/mole ZrB_2 versus moles HF/mole ZrB_2, In this study the theoretical quantity of $ZrF_4 \cdot H_2O$ was not achieved, The grey color of the reaction product material indicated that perhaps the ZrB_2 had not completely reacted, as $ZrF_4 \cdot H_2O$ is a white powder. X-ray diffraction analysis indicated that both ZrB_2 and $ZrF_4 \cdot H_2O$ were present as reaction product materials. Additional studies are required to account for the less than theoretical yield of $ZrF_4 \cdot H_2O$ for reactions occurring between ZrB_2 and HF.

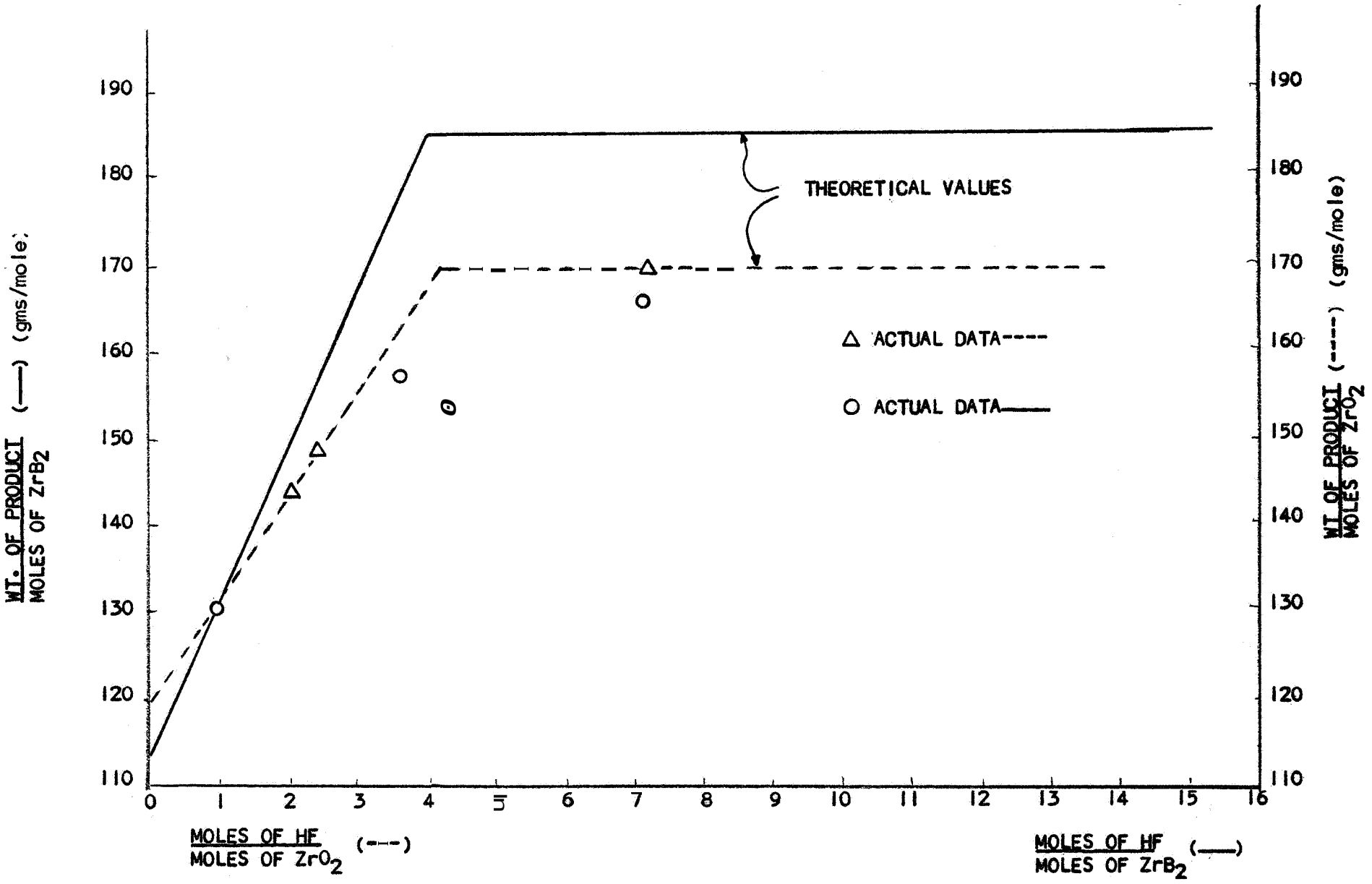

Figure 4-8. Thermogravimetric Studies of ZrB_2 +49% HF and ZrO_2 + 49% HF

4.2.4 X-ray Diffraction Analysis

X-ray diffraction studies were conducted to determine the solid reaction products resulting from ZrB_2 treated with H_2PO_3F. The studies indicate that the reaction between ZrB_2 and H_2PO_3F is a two-step reaction with the formation of $ZrF_4 \cdot H_2O$, an intermediate reaction product, which reacts with available phosphate to form ZrP_2O_7, the likely bond medium.

X-ray diffraction analysis of a ZrB_2 plus 4 weight percent H_2PO_3F mixture heated to 150°C (302°F) did not reveal the presence of any material other than ZrB_2. Therefore ZrB_2 was reacted with an excess of H_2PO_3F sufficient to thoroughly wet all grains, heated to 150°C (302°F), and the reaction product material analyzed. The results are indicated in the following equation:

$$ZrB_2 + H_2PO_3F \rightarrow ZrP_2O_7 + (BF_3, H_2, H_2O, HF, \text{etc.}) \quad (4.2.4\text{-}1)$$

Since H_2PO_3F behaves chemically as a mixture of HF and H_3PO_4, additional reactions were studied for ZrB_2 plus HF and ZrB_2 plus H_3PO_4. A mixture of ZrB_2 plus excess 49% HF was blended, dried at 150°C (302°F), and analyzed. The results are indicated as follows:

$$ZrB_2 + 49\%\ HF = ZrF_4 \cdot H_2O + (BF_3, H_2, H_2O, \text{etc.}) \quad (4.2.4\text{-}2)$$

A mixture of ZrB_2 plus excess 85% H_3PO_4 was blended, dried at 150°C (302°F), and analyzed. The results are indicated in the following equation:

$$ZrB_2 + \underset{\text{(excess)}}{H_3PO_4} \rightarrow ZrP_2O_7 + BPO_4 + \underset{\text{product}}{\text{unidentified}} \quad (4.2.4\text{-}3)$$

Based on the differential thermal analysis studies, two reactions occurring for Equations 4.2.4-1 and 4.2.4-2 are exothermic. The intensity of reaction between HF and ZrB_2 is considerably greater than the reaction between H_3PO_4 and ZrB_2. This indicates that reactions between the fluorine ion in

H_2PO_3F and ZrB_2 tend to form $ZrF_4 \cdot H_2O$ which in turn reacts with available phosphate material to form ZrP_2O_7, the possible bond medium as shown in the following equation:

$$ZrF_4 \cdot H_2O + 2H_3PO_4 \rightarrow ZrP_2O_7 + 4HF + 2H_2O \qquad (4.2.4\text{-}4)$$

4.2. 5 Infrared Spectrographic Study

A study was under taken to determine the role of the boron in ZrB_2 for reactions with H_2PO_3F. As discussed previously, the very reactive fluorine ion of H_2PO_3F initially tends to react with ZrB_2. The fluorine ion of H_2PO_3F could react with the boron in ZrB_2 to form gaseous reaction products. Boron trifluoride (BF_3) and/or diborane (B_2H_6) were considered possible reaction products. Thermodynamic calculations indicate that the free energies of formation for these materials are:

$$\Delta°F\ B_2H_6 = +\ 400\ K\ calories$$

$$\Delta°F\ BF_3 = -\ 434\ K\ calories$$

The large negative value of free energy of formation for BF_3 indicates the higher probability of formation. To determine the gaseous reaction products formed, infrared spectrographic analyses were undertaken. A sketch of the reaction apparatus and trap system is shown in Figure 4-9. The reactant materials (ZrB_2 plus H_2PO_3F) were placed in a platinum cup. The interior of the system was coated with paraffin wax to prevent etching of the system by HF. A Perkin Elmer spectrophotometer was used to obtain infrared spectrographic data, A CaF_2 cell was used to contain the gaseous reaction product material. Positive identification of the compound BF_3 was obtained.

4.2. 6 Matrix Fabrication

Preliminary work was restricted to the use of -325 mesh ZrB_2 pending receipt of coarser particle size fractions. This work dealt with the preparation of small compacts, 1" OD, prepared by (1) mechanical pressing and

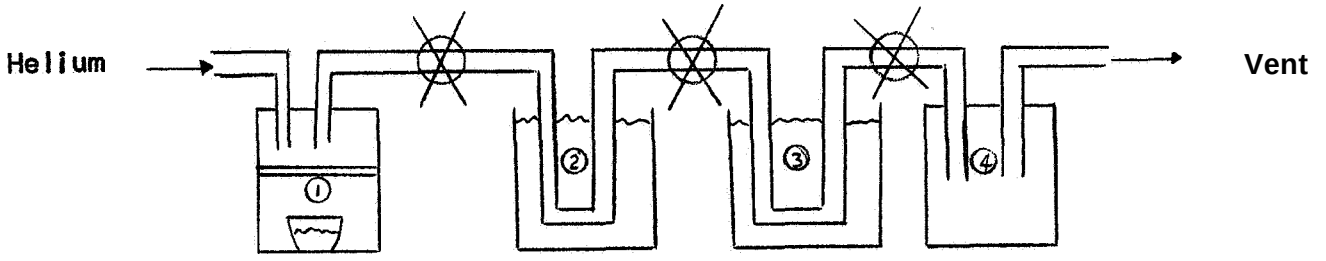

1. Platinum cup containing H_2PO_3F + ZrB_2
2. Dry Ice–Alcohol Trap to Condense HF, H_2O
3. Liquid Nitrogen Trap to Condense Gaseous Products (BF_3)
4. Exhaust Trap (H_2O to Trap H_2 and BF_3)

Figure 4-9. Gaseous Reaction Separation Apparatus

curing while under pressure and (2) vibratory compaction followed by curing. Upon curing, all specimens were well consolidated. Although the particles of the vibratory cast material were consolidated, the compacts were bloated due to the evolution of gas during the cure cycle, The reaction of the acid on the fine powders was associated with a high degree of gas evolution which produces a foam structure when unrestrained.

Upon receipt of the coarse fraction powders (-150 + 325 mesh), work was undertaken to eliminate the bloating and obtain a dense body, The initial attempt to compound a non-foaming chemically consolidated castable ZrB_2 was made using 60 parts by weight of -150 plus 325 mesh ZrB_2, 40 parts by weight -325 mesh ZrB_2, 5 parts by weight $NH_4H_2PO_4$, and 4 parts by weight H_2PO_3F. The high viscosity of the mix precluded the possibility of casting, but a hard, apparently dense, dry pressed body was formed. The viscosity was decreased by increasing the acid content and adding water, but the mixture still bloated during the cure cycle.

Several attempts were made to decrease the bloating tendencies of the material by additives to the water to decrease the surface tension and thus allow the gases to be vented more readily. Traces of Aerosol-OT, a wetting agent, were added to the mixture but the foaming was not retarded. The addition of a wetting agent with a trace of Dupont D anti-foaming agent did not reduce the bloating during the cure,

To further explore the effect of lower surface tension liquid, Isopropyl alcohol was substituted for water in several pellets, and a decrease in the foaming was achieved when the $NH_4H_2PO_4$ was omitted. Although a decrease was achieved in the volume change due to foaming, large pores still existed. Table 4-5 is a record of the formulations used in this study showing the results of addition variation. It became apparent that development studies beyond the scope of this program would be required to obtain a suitable chemically consolidated ZrB_2 matrix.

Table 4-5

FORMULATIONS OF ZrB_2 MATRIX STUDIES*

ZrB_2 -150 +325	ZrB_2 -325	$NH_4H_2PO_4$	H_2PO_3F	$(CH_3)CHOH$	Aerosol Wetting Agent	Dupont-D Defoaming Agent	H_2O	Remarks
60	40	5	4	---	--	--	-	Hard pellet formed by pressing
60	40	5	5				3	Foamed During Air Dry (Too Dry)
60	40	--	5	---	--	--	3	Foamed During Air Dry (Too Dry)
60	40	--	6	---	--	--	3	Foamed
60	40	5	6	---	--	--	3	Foamed
60	40	10	6	---	--	--	2	Foamed
60	40	5	6	---	Trace	--	3	Foamed
60	40	--	6	---	Trace	--	3	Foamed
60	40	--	6	---	Trace	Trace	3	Foamed
60	40	--	4	4	--	--	-	Fluid, did not foam (very weak bond)
60	40	5	6	6	--	--	-	Very fluid poor bond (Foamed on heating)
60	40	--	6	6 3	--	--	-	Foamed slightly during heating
60	40	--	4	---	--	--	2	1% Clay Foamed (Fluid)
60	40	5	6	---	--	--	-	10% Sol. Citric Acid (Foamed)

w

4.3 ALUMINA MATRIX

Phosphate bonding of alumina has been described by Gitzen et al. (Reference 5). The reactions of alumina to form aluminum phosphate has been described as follows:

$$2H_3PO_4 \rightarrow H_4P_2O_7 + H_2O \qquad (4.1\text{-}1)$$

$$Al_2O_3 + H_4P_2O_7 \rightarrow 2AlPO_4 + 2H_2O \qquad (4.1\text{-}2)$$

Blocker et al. (Reference 6) developed "trowalable" insulating coatings of alumina, phosphoric acid and clay for which flexural strengths up to 8,500 psi at room temperature and 1,500 psi at 1,800°F (982°C) were claimed. Castable systems exhibit much lower strength, averaging approximately 3, 100 psi,

A castable alumina matrix formulation with good casting properties was developed in this program. The composition of the alumina castable is shown in Table 4-6. The clay addition to the alumina castable provides a slight amount of drying shrinkage to balance a disruptive volume expansion that takes place in the early stages of curing.

Room temperature flexural strength tests were conducted on the alumina matrix, using specimens which were not precision ground, These tests yielded an average flexural strength of 3, 125 psi.

Table 4-6

FORMULATION OF CHEMICALLY CONSOLIDATED ALUMINA

Material		Parts by Weight
T-61 48 mesh	Al_2O_3	50
T-61 -325 mesh	Al_2O_3	30
T-61 -20 micron	Al_2O_3	20
Black Label Clay		0. 5
85% Phosphoric Acid (H_3PO_4)		11
Water		8

4.4 REFERENCES FOR SECTION 4

1. H. Leggett, R. L. Johnson, E. W. Blocker and E, D. Weisert, Development and Evaluation of Insulating Type Ceramic Coatings, WADC Report No. TR-59-102, Part II, October 1960

2. A. H. Bremser, and J. A. Nelson, Phosphate Bonding of Zirconia, Bulletin American Ceramic Society, Vol. 46, No, 3, 1967.

3. V, H, Edlin, Bonding Reaction and Mechanism in Chemically Bonded Zirconia, Scientific and Technical Aerospace Reports 2, Part II, No. 1384, 1964.

4. Encyclopedia of Chemical Technology, Volume 15, p. 307, Edited by R. E, Kirk and D. F. Othmer., The Interscience Encyclopedia Inc., New York, 1956.

5. W, H, Gitzen, L, D, Hard and G. MacZura, Phosphate-Bonded Alumina Castables: Some Properties and Applications, Bulletin American Ceramic Society, Vol. 35, No. 6, 1956.

6. E, W. Blocker, A. V. Levy, C. D. Hauck, and S. A, Sklarew, Part I Development and Evaluation of Insulating Type Ceramic Coatings, WADC Technical Report 59-102, October 1959.

Section 5
MATRIX AND REINFORCING EVALUATION

Despite the stability of zirconium pyrophosphate to 1,380°C (2,516°F) and the stability of the zirconyl phosphate to 1,600°C (2,912°F), as discussed in Section 4.1, strengths of the chemically consolidated zirconia above 2,000°F (1,093°C) were low. Alumina retained good strength up to the latter temperature.

Evaluations of the chemically consolidated zirconia conducted by Bremser and Nelson (Reference 2, Section **4)** indicated a sharp reduction of flexural strength from 3,700 psi at room temperature to 2,000 psi at 1,200°C (2,192°F). X-ray diffraction analysis of the specimens revealed the presence of $CaZr(PO_4)_2$. The new phase was decreased upon further heating to 1,665°C (3,029°F).

The optimized system for ZrO_2, developed in this phase of the work, was based on room temperature flexural strengths. Higher strength, compatible with fabrication techniques, was developed by the use of H_2PO_3F without additions of the $NH_4H_2PO_4$ as the retarding agent. **As** the reaction of H_2PO_3F with ZrO_2 is extremely rapid at room temperature, the initial mixing was conducted with refrigerated acid to retard the reaction rate. The low unexpected values of strength obtained with the zirconia may have been caused by incomplete formation of the ZrF_4, resulting in a decrease of the ZrP_2O_7 as the binding phase. The formation of the $CaZr(PO_4)_2$ by depletion of the calcia, used for stabilization, results in formation of monoclinic zirconia, which has a lower strength than the cubic form and probably accounts for the low values obtained with the calcia stabilized zirconia.

In order to obtain data for the design of the prestressed specimens, evaluations of the bond existing between the matrix and embedded tungsten reinforcing were conducted,

5.1 STRENGTH OF CHEMICAL BOND

A method based upon shear-lag theory of estimating the existence and strength of a chemical bond between the reinforcing and the ceramic is presented. However, the scatter in test data is high and therefore conclusive statements regarding the strength of the chemical bond cannot be made as a result of the experimental program. In view of this scatter, no further efforts were undertaken to establish the true strength of the chemical bond. The reinforcement anchoring was primarily by mechanical means.

5.1.1 Fundamental Theory

The strength of the chemical bond that exists between the filaments and the matrix may be estimated by using the equations of the shear-lag theory in conbination with the test data on the average shear strength of imbedded fibers of various lengths. The parametric relationship between the properties and geometry of the constituents and the shear strength of the bond may be obtained by considering a model shown in Figure 5-1. From such a consideration, the following expression can readily be obtained for the force F in the fiber and the shear stress along the fiber at any point (Reference 1).

$$F = P\,(\cosh ax - \coth \alpha\ell \sinh ax) \qquad (5.1\text{-}1)$$

$$\tau = \frac{P\alpha}{2\pi r}\,(\sinh ax - \coth \alpha\ell \cosh \alpha x) \qquad (5.1\text{-}2)$$

where

$$\alpha = \sqrt{\frac{2G_c}{b_c r E_w}}$$

G_C is the shear modulus of the matrix, E_w is the modulus of elasticity of the fiber, b_C is the adhesive thickness, and r is the fiber radius.

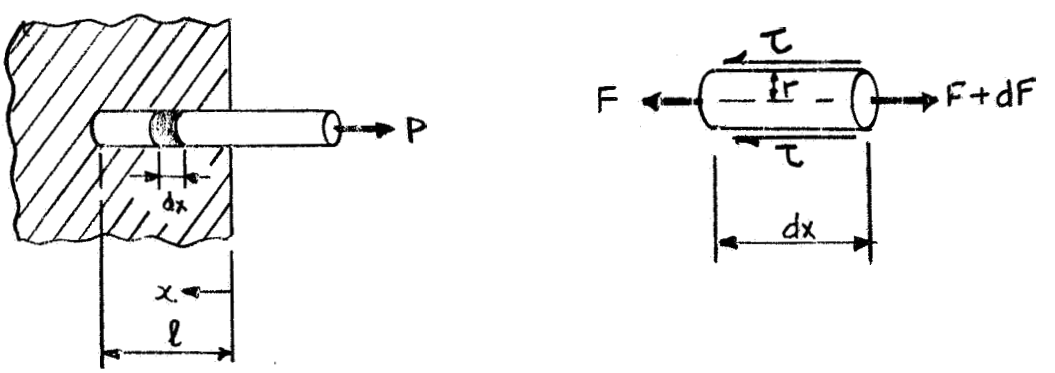

Figure 5-1. Filament Imbedded in a Matrix

Equation 5. 1-2 gives the true shear stress at any point x. The average shear stress due to a load P is

$$\tau_{RVE} = \frac{P}{2\pi r \ell} \qquad (5.1\text{-}3)$$

In view of the above relationship, the true shear stress at any point x can be expressed in terms of average shear stress as follows:

$$\frac{\tau}{\tau_{AVE}} = (\alpha \ell) \left[\sinh \alpha x - \coth \alpha \ell \cosh \alpha x\right] \qquad (5.1\text{-}4)$$

The maximum shear stress will occur at x = 0. Setting **x** = 0 in the above equation and defining the maximum shear stress at τ_c, the stress ratio becomes

$$\frac{\tau_o}{\tau_{AVE}} = -\alpha \ell \coth \alpha \ell \qquad (5.1\text{-}5)$$

It is seen from Equation 5. 1-5, that as $\alpha \ell \to 0$, τ_o approaches τ_{AVE}. This condition may be used in determining the shear strength of the bond. Since, for a given matrix and filament materials, α will remain constant, τ_o/τ_{AVE} will be a function of the embedded length, ℓ, only. By conducting pullout tests on filaments, plotting a curve τ_{AVE} vs ℓ and extrapolating τ_{AVE} at $\ell = 0$, one can estimate the shear strength of the bond.

Some typical theoretical results illustrating this test concept are shown in Figure 5-2 for several materials. The true shear strength was assumed as τ_o = 7, 000 psi. From Figure 5-2 it is quite obvious that if one did not know that τ_o = 7, 000 psi, but knew τ_{AVE} for several values of ℓ, say ℓ = 0.02", 0.04", 0.08", 0.16", then it would be a relatively simple task to obtain the true shear strength of the chemical bond.

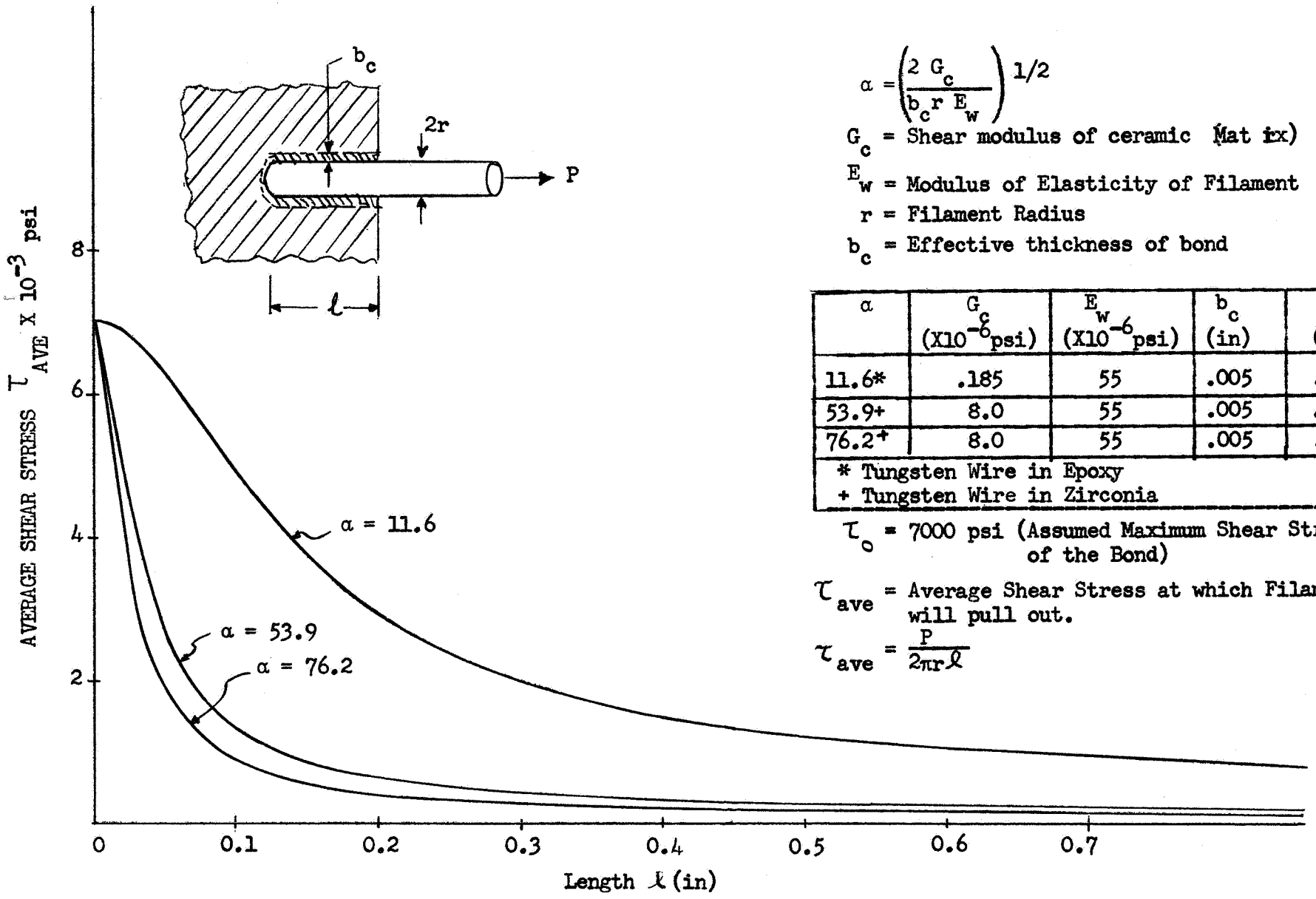

$$\alpha = \left(\frac{2\,G_c}{b_c\,r\,E_w}\right) 1/2$$

G_c = Shear modulus of ceramic Mat rx)

E_w = Modulus of Elasticity of Filament

r = Filament Radius

b_c = Effective thickness of bond

α	G_c ($X10^{-6}$psi)	E_w ($X10^{-6}$psi)	b_c (in)	r (in)
11.6*	.185	55	.005	.010
53.9+	8.0	55	.005	.020
76.2+	8.0	55	.005	.010

* Tungsten Wire in Epoxy
\+ Tungsten Wire in Zirconia

τ_o = 7000 psi (Assumed Maximum Shear Strength of the Bond)

τ_{ave} = Average Shear Stress at which Filament will pull out.

$$\tau_{ave} = \frac{P}{2\pi r \ell}$$

Figure 5-2. Pullout Strength of Embedded Filament

5.1.2 Experimental Results

To experimentally establish the existence of the chemical bond as well as its strength, pullout tests were conducted on tungsten wires. To determine the effective glue line thickness, b_c, pullout tests were conducted on the fiber embedded in an epoxy matrix; next, the fibers were embedded to a predesignated length in a chemically bonded zirconia, and pullout tests were conducted. The results of these tests are shown in Table 5-1. No conclusive statement regarding the true strength of the filament-to-ceramic chemical bond can be made because of the scatter in the data. In the performance of these tests, it was found that the condition of the embedded end of the wire, i.e. the existence of slight irregularities, or barbs, had a decided effect on the pullout load of the embedded wires. Although care was taken to remove irregularities and maintain a constant surface condition, the test results indicate that this condition may not have been achieved. It appears that extreme care must be taken in the preparation and testing of the pullout specimens in order to obtain reliable results. Moreover, a large number of specimens has to be tested. Since the anchoring of the reinforcement in the present program was to be primarily by mechanical means, the dependence of fiber anchoring on chemical bond was of secondary importance, and, therefore, no further attempt was made to establish the true strength of the chemical bond between the fibers and the ceramic.

5.2 MECHANICAL PROPERTIES OF TUNGSTEN REINFORCEMENT

Tensile tests of the reinforcement were conducted with a screw-driven universal testing machine calibrated to ASTM requirements. Tensile properties were determined for single strand 0.012"-diam tungsten wire, 21-strand tungsten cable, and 49-strand tungsten cable at various temperatures as shown in Table 5-2. The cable containing 21 strands consisted of three bundles of seven strands each as shown in Figure 5-3. The 49-strand cable containing 7 bundles of 7 strands each is shown in Figure 5-4. Some of the geometric characteristics of the reinforcement are shown in Figure 5-5. In this figure is also shown a comparison between experimental and theoretical results on the strength and modulus of various reinforcement

Table 5-1

LOAD REQUIRED TO PULL OUT 0.020" DIA. TUNGSTEN WIRES AT VARIOUS DEPTHS IN EPOXY AND CHEMICALLY CONSOLIDATED ZIRCONIA

Material	Depth of Wire (in.)	Load in Pounds
Epoxy	.05	0
	.05	0
	.05	7.2
	.1	6.3
	.1	12.2
	.1	2.4
	.2	8.1
	.2	13.6
	.2	17.2
	.5	11.8
	.5	21.8
	.5	16.4
Zirconia	.25	1
	.5	54
	.5	38
	.5	71 Pullout
	1	33
	1	92.5 Wire failed at grip
	1	71

Head Travel 0.05 in/min

configurations. The theoretical results are based on equations of Section 3.5. Although good agreement exists between experimental and predicted values for the load carrying ability of reinforcement, the agreement between the experimental and predicted values of Young's modules is poor.

Table 5-2

SUMMARY OF TESTS CONDUCTED

Type of Test	Material	TEST TEMPERATURE °F							Total No. Tests
		70	500	1000	1500	2000	2500	3500	
	Matrix								
Tension	Alumina	5	---	6	8	6	---	---	25
	Zirconia	8	---	8	8	--	---	---	24
Flexure	Alumina	4	---	--	4	4	4	---	16
	Zirconia	3	---	3	3	2			11
Ring Bending	Alumina	3	---	--	3	3	3		12
	Zirconia	3	---	3	3	1			10
Shear	Alumina	4	---	1	3	3	3		14
	Zirconia	3	---	3	3	5			14
Thermal Expansion	Alumina	2							2
	Zirconia	2							2
	Reinforcement								
Tension	1 Strand	5	---	--	4	--	3	3	15
	21 Strand	4	---	--	3	--	3	6	16
	49 Strand	6	---	--	3	--	3	4	16
Anchoring Ability	21 Strand	11	---	--	9	8	--	--	28
	49 Strand	11	---	--	6	6	--	--	23
	Prestressed Zirconia								
Tension	21 Strand	4	---	6	6	3	6	--	18
	49 Strand	7	---	5	6	--	1	--	18
Flexure	Zirconia								
	21 Strand	6	3	3	6	--	--	--	18
	49 Strand	6	3	3	6	--	--	--	18

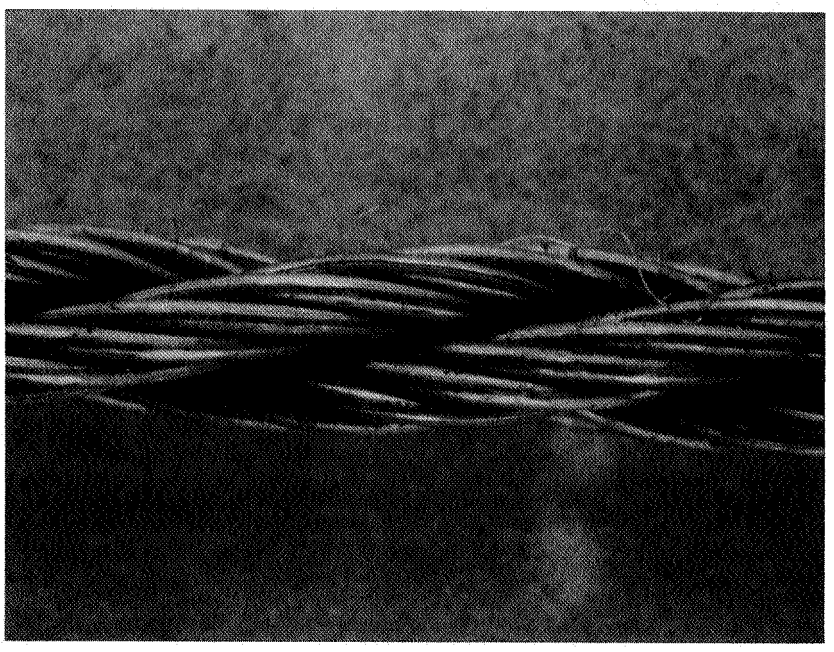

M25160 15X

SIDE VIEW

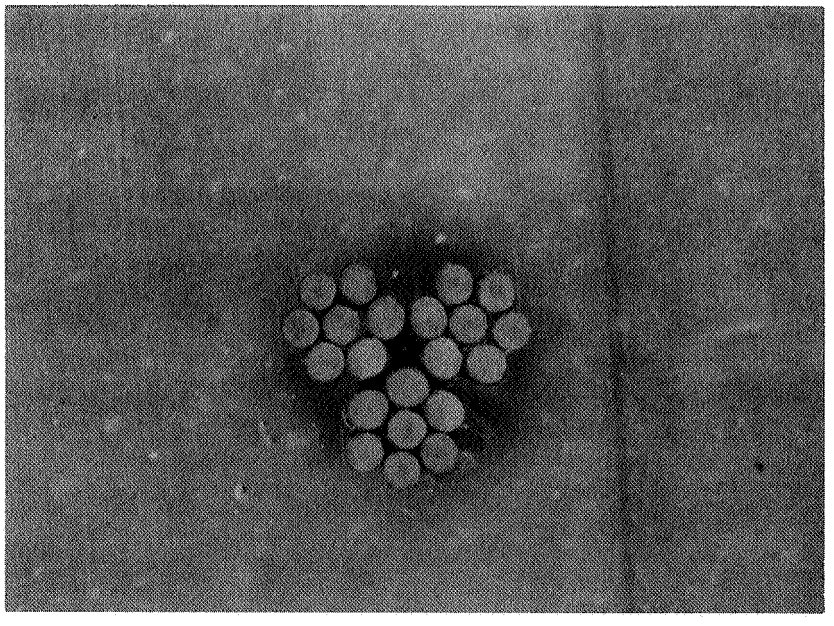

M25162 15X

END VIEW

Figure 5-3. Appearance of 7 x 3 Cable Fabricated From 0.012-in. Diameter Tungsten Wire

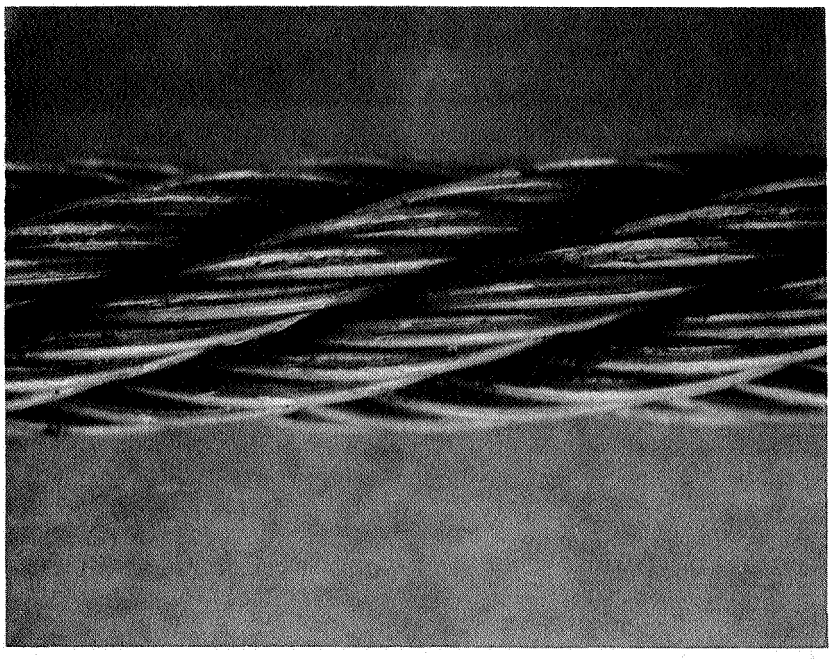

M25161 15X

SIDE VIEW

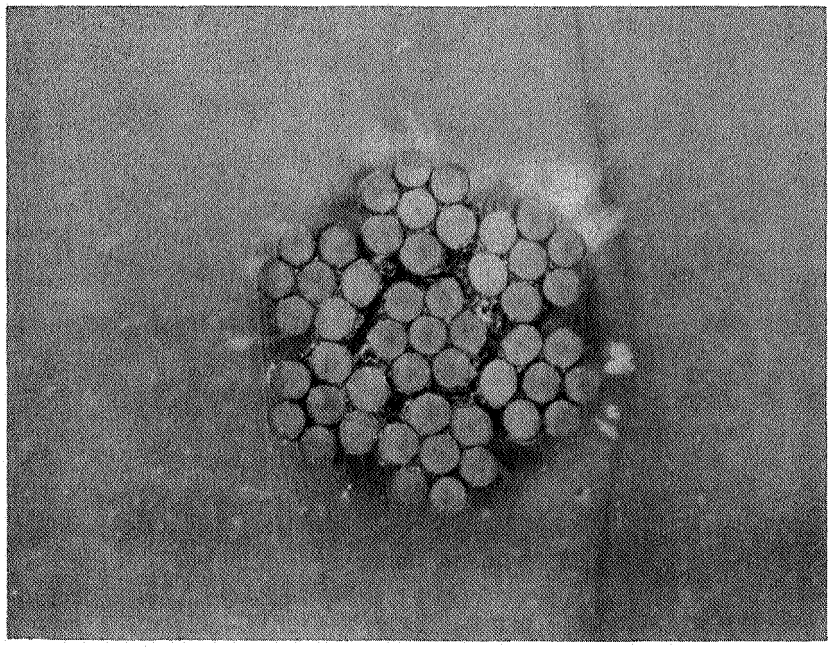

M25 I63 15X

END VIEW

Figure 5-4. 7 x 7 Cable Fabricated of 0.012-in. Diameter Tungsten Wire

Configuration	L(in)	R(in)	β(°)	Theory		Experiment(1)	
				$\frac{E^*}{E_1}$	$\frac{P^*}{P_1}$	$\frac{E^*}{E_1}$	$\frac{P^*}{P_1}$
1	---	---	---	1.000	1.000	1.00	1.00
7	0.318	0.125	13.90	0.905	6.49	---	---
3 x 7	0.555	.0214	13.67	0.808	18.90	0.501	17.60
7 x 7	0.797	.0365	16.00	0.791	41.10	0.439	39.70

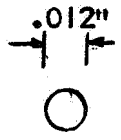

1 Wire

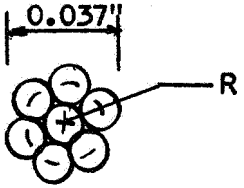

7 Wires
(= 1 strand)

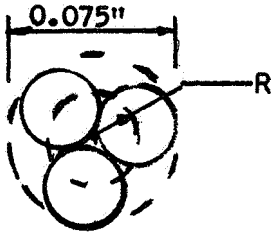

3, 7-Wire strands

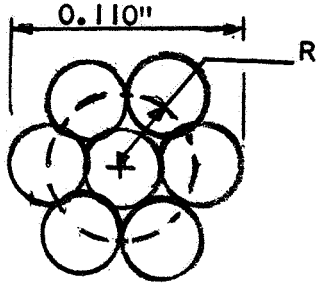

7, 7-Wire strands

E_1 = Modulus of elasticity of single wire

E^* = Modulus of elasticity of a strand

P_1 = Load carrying ability of one wire

P^* = Load carrying ability of a strand

(1) The experimental value of Young's modulus is based on area A^*, where $A^* = nA_1$ is the area of a single fiber, and n is the number of fibers in a strand

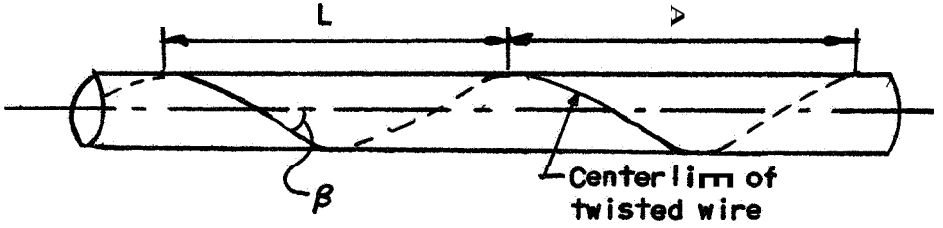

Figure 5-5. Properties of Reinforcement Configurations

The grips for the room temperature tensile tests were string grips, the type normally used for cords. The specimens were tested with 6 inches between grips and a 4-inch gage length at a head travel rate of 0.05 in/min. Autographic recordings were of upper target travel versus lower target travel with load pips at fixed intervals. Stress-strain curves were plotted from the autographic recordings.

For the elevated temperature tests, copper ends were swaged onto the specimen ends and the swaged ends were gripped with clamp-type jaws. Two heating methods were employed for the reinforcement tensile tests. The cables were directly resistance-heated as shown in Figure 5-6. Radiant heating was required with the single-strand tungsten wire, since the targets attached to the wire for strain measurement with the Optron noticeably cooled the specimen at the point of attachment and non-uniform heating within the test section resulted. A platinum wire-wound furnace was used for heating the wire. Temperature was monitored with a microoptical pyrometer in both cases. An argon atmosphere was provided for all elevated temperature tests to prevent oxidation of the tungsten specimens.

Test results for single-strand tungsten cable are shown in Table 5-3 and the results of the 21- and 49-strand cables are shown in Tables 5-4 and 5-5. It should be noted that the areas contained in the latter two tables are a summation of the areas of each individual strand.

The room temperature test specimens failed at the grips and the elevated temperature test specimens failed in the gage length. All cables failed progressively, with failure occurring in the strands.

Total strain could not be measured for the tensile tests of the wire and cable, The magnification required to obtain valid moduli values precluded obtaining total strain on the graph. The strain values reported were recorded to some value beyond the 0.2% offset yield point for the purpose of determining the modulus of elasticity values. The room temperature strain for the single-strand wire was obtained using the Instron light weight attachable extensometer while the Optron was used at elevated temperature.

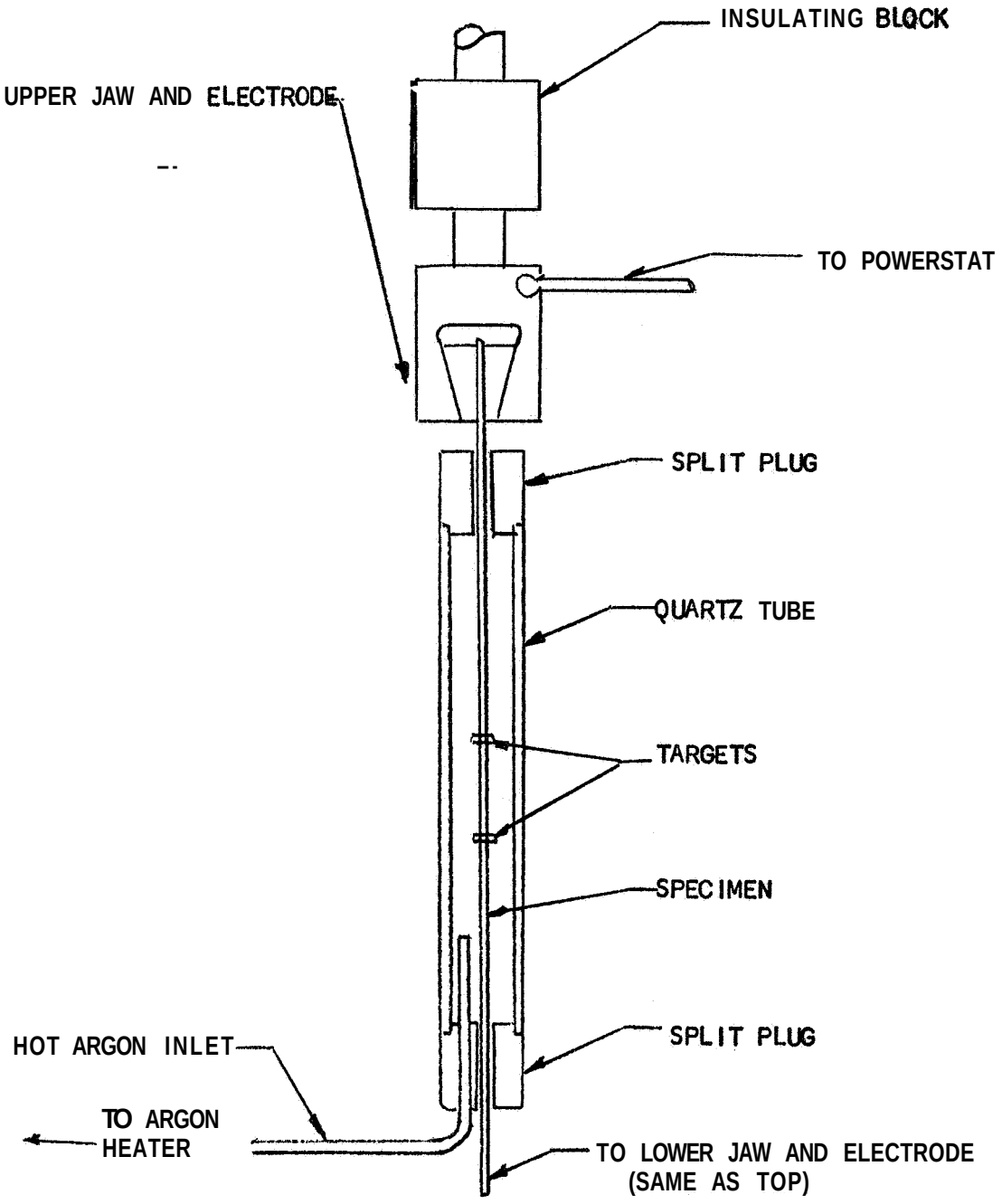

Figure 5-6. Test Apparatus for Determining Elevated Temperature Properties of Reinforcing

Table 5-3

TENSILE PROPERTIES OF SINGLE-STRAND TUNGSTEN WIRE

Nominal Temp. (°F)	Spec. No.	Ult. Load (lbs)	Area (in^2)	Ult. Stress (ksi)	Modulus of Elasticity (psi x 10^{-6})	Point of Failure
70	1	40.5	.000111	365	55.6	At Grips
	2	40.2	.000111	362	54.3	At Grips
	3	40.2	.000111	362	54.3	At Grips
	4	40.5	.000113	358	53.3	At Grips
	5	40.2	.000111	362	53.6	At Grips
1500	1	19.75	,000113	178	23.0	Center
	2	21.70	.000113	192	----	Center
	3	22.5	.000113	203	20.4	Center
	4	21.75	.000113	192	25.6	Center
2500	1	10.0	,000113	88.5	----	Center
	2	12.5	.000113	110.6	----	Center
	3	9.5	.000113	84.1	----	Center
3500	9	2.0	.000113	17.7	----	Center
	10	2.0	.000113	17.7	----	Center
	11	2.3	.000113	18.0	----	Center

5.3 PROPERTIES OF MATRIX MATERIALS

The tensile and flexural properties of the matrix materials were determined for temperatures ranging from 70°F (21.2°C) to 2,000°F (1,093°C). The flexural properties were determined by beam flexure and by ring compression tests. The shear strengths were determined by the double shear method. A 10K Riehle Universal Testing Machine calibrated and certified per ASTM E-4-61T was used for all the mechanical properties tests. The thermal expansion was determined for both matrix materials in the range of 70°F (21.2"C) to approximately 3,000°F (1,649"C).

Table 5-4

TENSILE PROPERTIES OF 21-STRAND TUNGSTEN CABLE

Nominal Temp. (°F)	Spec. No.	Ult. Load (lbs)	Area(1) (in2)	Ult. Stress (ksi)	Modulus of Elasticity (psi X 10^6)	Point of Failure
70	1	700	.00237	296	30.4	At Grips
	2	685	.00237	289	29.1	At Grips
	3	695	.00237	293	21.8	At Grips
	4	695	.00237	295	27.3	At Grips
1500	12	350	.00237	14%	29.5	Center
	13	340	.00237	144	21.8	Center
	14	275	.00237	116	18.0	Center
2500	16	120	.00237	51	10.7	Center
	17	130	.00237	55	11.2	Center
	18	121	.00237	51	13.6	Center
3500	20	35.5	.00237	14.8	10.8	Center
	21	34.2	.00237	14.4	----	Center
	19	33.7	.00237	14.2	----	Center
	22	41.0	.00237	17.3	----	Center
	23	34.0	.00237	14.3	----	Center
	24	32.0	.00237	13.5	----	Center

(1) Area based on sum of the areas of single strands,

5.3.1 Tensile Tests

The furnace used for heating the tensile specimens consists of a water-cooled shell and three resistance heating elements. Fire brick insulation was used to minimize the heat loss to the water-cooled shell. For temperatures to 2,000°F (1,093°C), Kanthal A-1 heating elements were used. At temperatures above 2,000°F (1,093°C) graphite elements were used.

Table 5-5

TENSILE PROPERTIES OF 49-STRAND TUNGSTEN CABLE

Nominal Temp. (°F)	Spec. No.	Ult. Load (lbs)	Area[1] (in^2)	Ult. Stress (ksi)	Modulus of Elasticity (psi X 10^{-6})	Point of Failure
70	9	1580	.00554	286	23.3	At Grips
	10	1565	.00554	283	25.9	At Grips
	11	1675	.00554	303	23.6	At Grips
	12	1570	.00554	284	28.2	At Grips
	13	1555	.00554	281	18.0	At Grips
	14	1580	.00554	286	24.0	At Grips
1500	24	630	.00554	114	18.6	Center
	23	740	.00554	134	21.3	Center
	22	745	.00554	135	19.7	Center
2500	26	280	.00554	51	12.5	Center
	27	274	.00554	45	15.7	Center
	25	380	,00554	69	----	Center
3500	28	104	.00554	18.9	----	Center
	1	120	,00554	21.6	----	Center
	2	90	.00554	16.2	----	Center
	3	93	.00554	16.8	----	Center

(1) Area based on the sum of the areas of single strands.

Since it was necessary to protect the graphite from oxidation, argon gas was introduced into the furnace during the tests. A chromel-alumel thermocouple was cemented to the specimen to monitor the temperature. Above 2,000IF (1,093°C) a micro-optical pyrometer was used. A photograph of the tensile test furnace is shown in Figure 5-7.

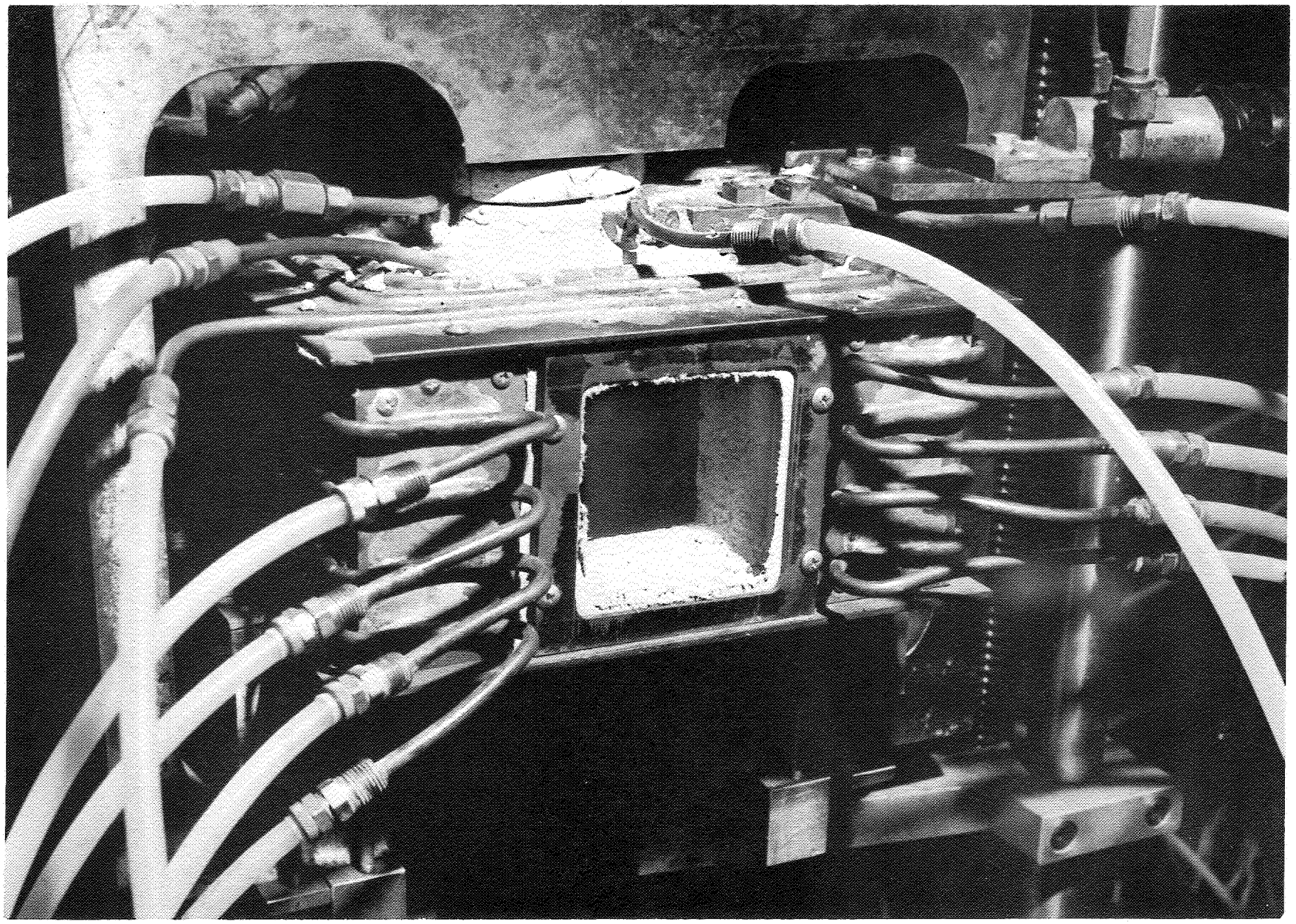

Figure 5-7. Tensile Test Furnace

A dog-bone type of specinien (Figure 5-8) similar to that described in ASTM E3-61T was used. Since the grips were not subjected to high temperature, it was possible to reduce fabrication costs by bonding metallic shoulders onto the specimen ends.

The gripping and alignment fixture shown in Figure 5-9 enabled precise alignment of the specimen with the grips. The alignment of the system was based on a completely rigid load train operating through a special die set. The grips act through aligned holes in the die set, thus minimizing lateral movement during the test. **A** photograph showing the alignment fixture after a test is shown in Figure 5-10.

The strain measurements at room temperature were taken with two Aminco-Tuckerman optical strain gages located 180" apart in the test section as shown in Figure 5-11. Two strain gages were used to detect any misalignment caused by improper seating in the grips. The Optron optical extensometer was used for elevated temperature tensile tests. Figure 5-12 is a photograph showing the Optron in place for a test.

The tensile test data obtained are shown in Table 5-6 for the alumina matrix and Table 5-7 is a resume of the data obtained for the zirconia matrix.

The data scatter in tensile evaluation was probably due to the variation in porosity in and between specimens and the presence of large pores. Sufficient precautions were taken to eliminate non-axial stresses due to misalignment and localized stress concentrations which normally arise from gripping or supporting the test specimen. The values of ultimate stress, in spite of the variation in porosity, are generally in fair agreement. Modulus of elasticity values are also reasonably reproducible with the exception of values obtained at 1,000°F (538"C).

5.3.2 Flexural Tests

The flexural tests were conducted to determine flexural strength and flexural modulus of elasticity of the matrix.

NOTE: 1. TOL. FRACTIONS ± 1/16, DECIMALS ± .020.
2. ALL DIAMETERS CONCENTRIC TO .0005".
3. 1 1/2" COLLAR IS BONDED TO SPECIMEN

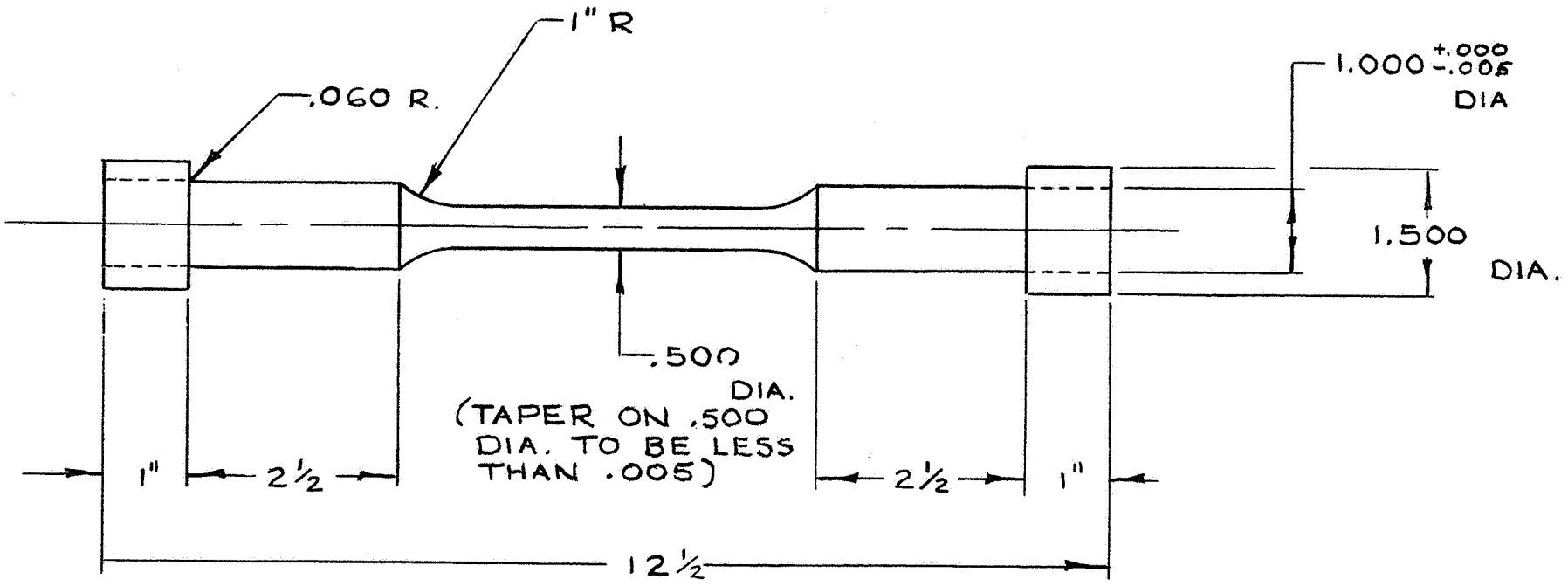

Figure 5-8. Tensile Specimen

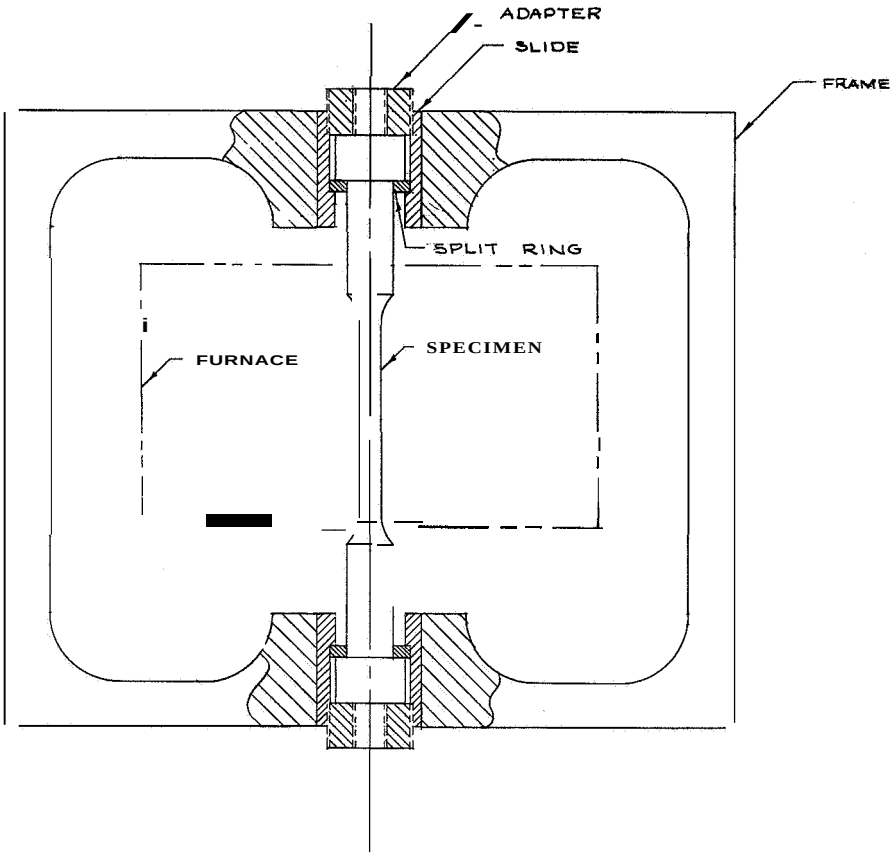

Figure 5-9. Tensile Test Alignment Fixture

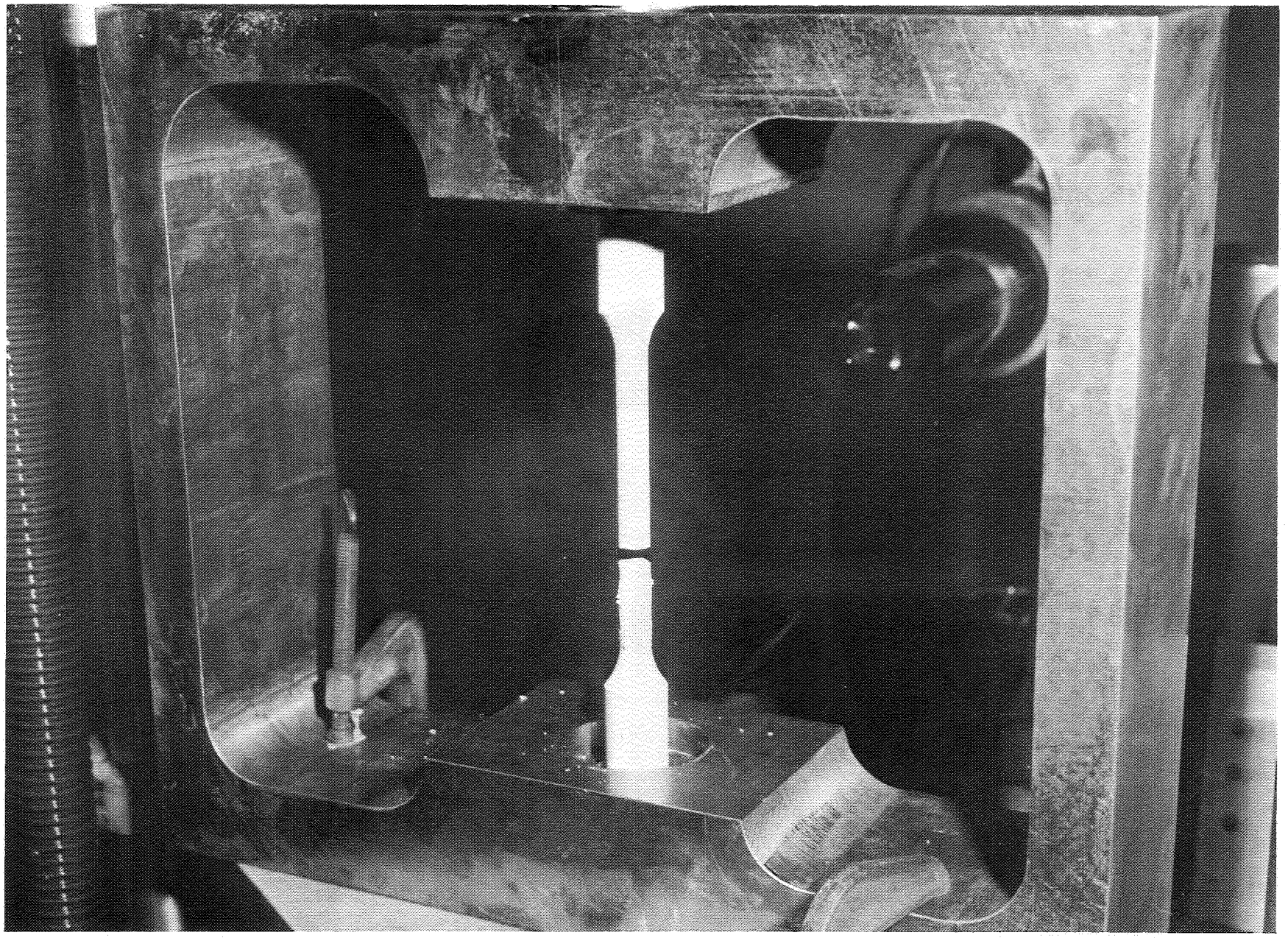

Figure 5-10. Test Specimen in Alignment Fixture – After Test

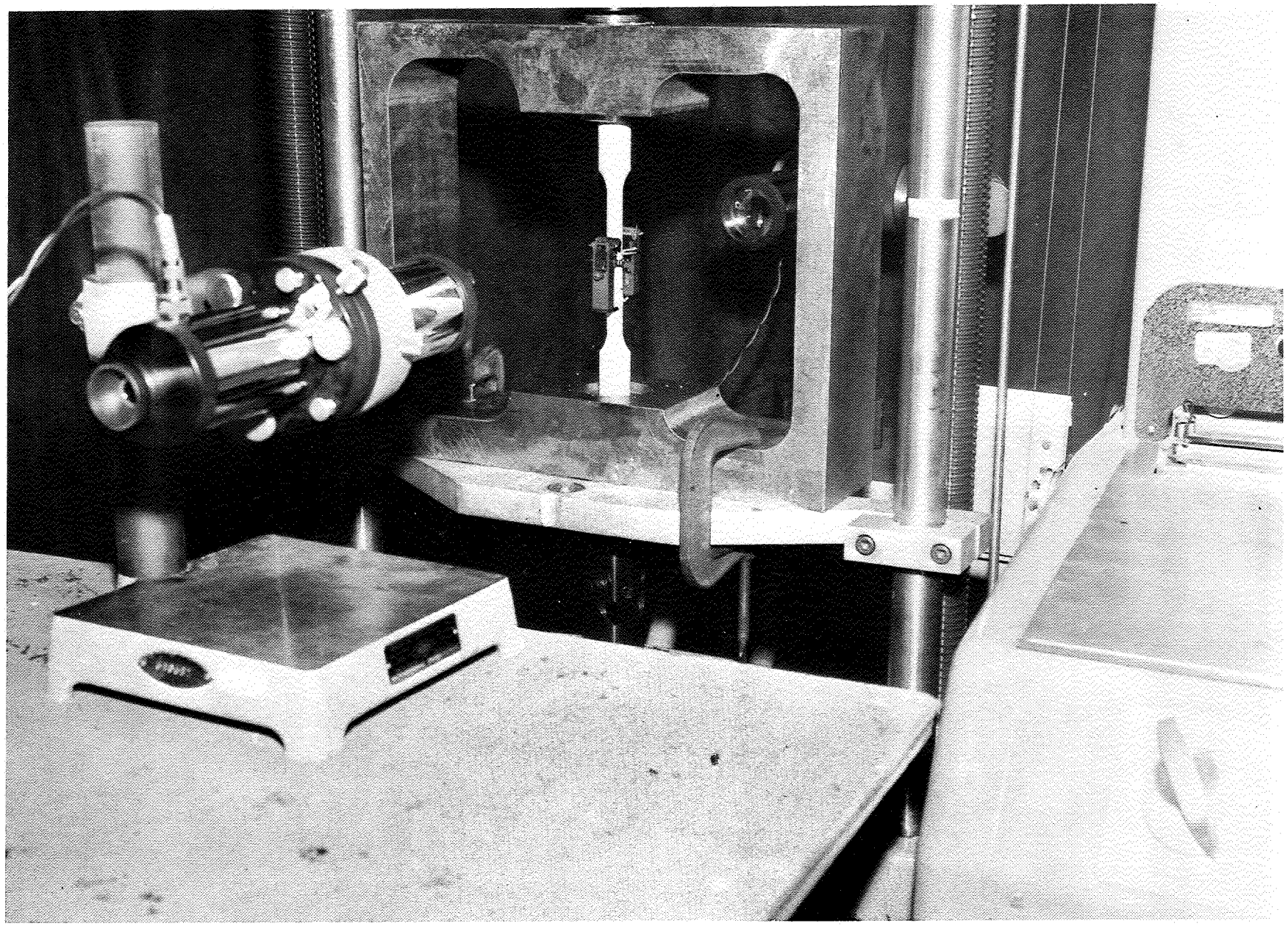

Figure 5-11. Aminco-Tuckermen Optical Strain Gages

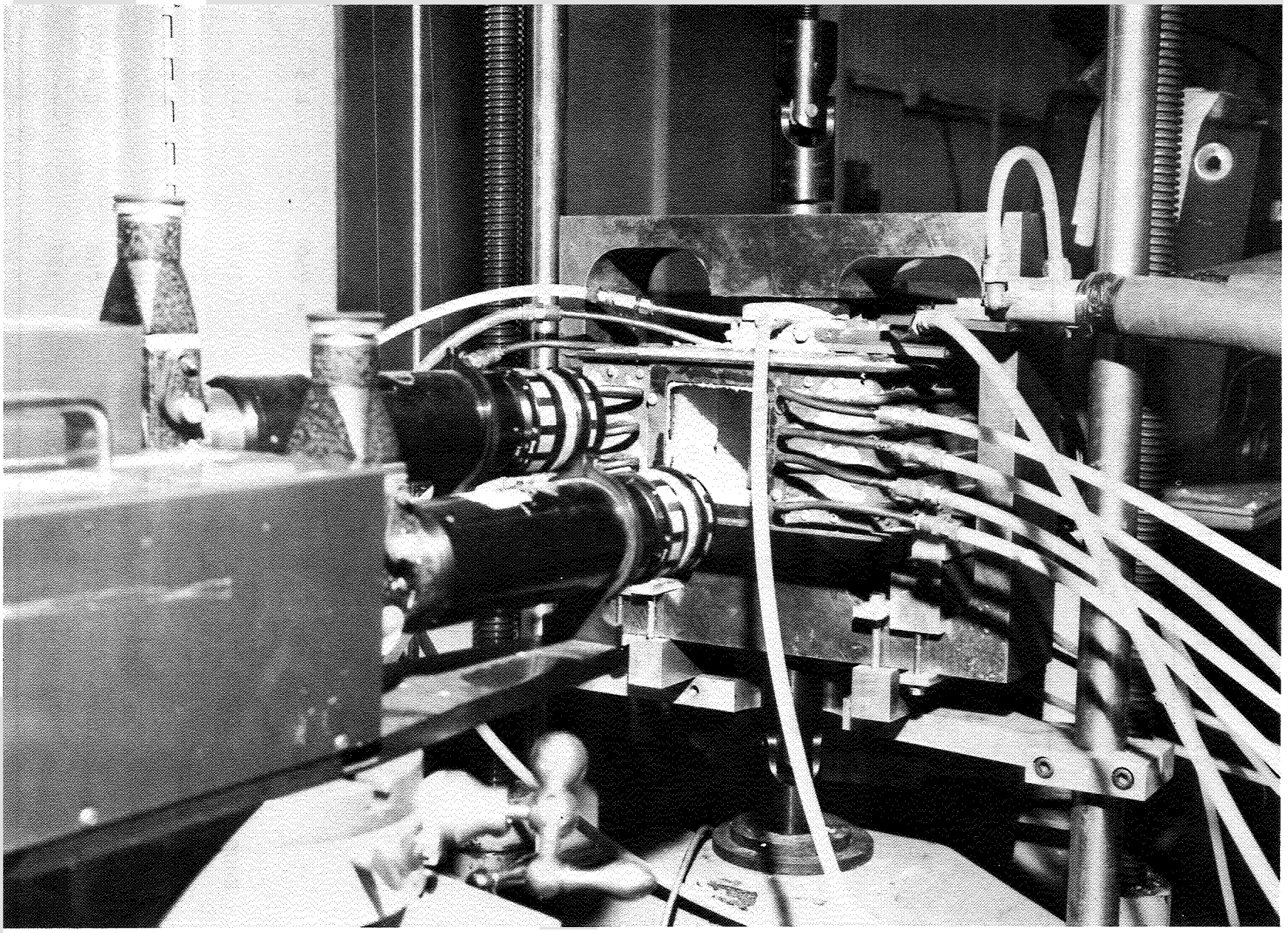

Figure 5-12. Optron Extensometer for Tensile Tests

Table 5-6

TENSILE PROPERTIES OF ALUMINA MATRIX

Nominal Temp. (°F)	Spec. No.	Ult. Load (lbs)	Area (in2)	Ult. Stress (psi)	E (psi X 10^{-6})
70	2	375	0. 197	1900	12. 1
	3	284	0. 196	1476	8. 0
	4	448	0. 196	2280	11.2
	30	303	0.204	1470	10.0
	31	406	0.196	2040	8. 7
1000	40	576	0. 196	2940	8. 1
	41	102	0. 195	512	----
	42	380	0. 197	1930	1. 34
	43	328	0. 197	1660	8. 1
	44	282	0. 197	1430	----
	45	240	0. 195	1230	1.33
1500	14	117	0. 195	896	1. 8
	16	157	0. 195	804	2. 4
	17	123	0. 196	628	1. 3
	18	224	0. 196	1155	1. 3
	19	158	0. 193	820	1. 3
	20	115	0. 195	589	1. 1
	46	167	0. 196	850	1. 6
	47	188	0. 197	950	1. 5
2000	21	21	0. 196	107	----
	22	58	0. 197	295	1. 6
	29	129	0.205	630	0. 25
	48	69	0. 193	357	----
	49	156	0.205	760	0. 83
	50	76	0. 196	387	----

Table 5-7

TENSILE PROPERTIES OF ZIRCONIA MATRIX

Nominal Temp. (°F)	Spec. No.	Ult. Load (lbs)	Area (in^2)	Ult. Stress (psi)	E (psi X 10^{-6})
70	1	780	0. 198	3941	12. 5
	5	648	0. 191	3391(1)	10. 1
	6	270	0. 195	1390(2)	10. 6
	7	600	0. 194	3086	8. 6
	32	700	0. 195	3580	9. 5
	33	500	0. 195	2560	9. 4
	34	700	0. 197	3554	10. 3
	35	700	0. 196	3565	10. 0
1000	8	373	0. 198	1885	5. 4
	9	450	0. 198	2272	6. 1
	11	346	0.195	1775	5. 7
	12	208	0.197	1059	4. 3
	13	428	0. 194	2204	2. 6
	15	437	0.209	2090	4. 0
	38	255	0.205	1225	6. 6
	39	286	0.220	1300	6. 3
1500	23	26	0. 193	135	----
	24	32	0. 195	164	0.476
	25	28	0. 198	142	----
	26	43	0. 196	219	0. 126
	27	43	0. 197	218	0.263
	28	39	0. 195	199	0. 328
	36	26	0. 194	134	----
	37	26	0. 195	133	----

(1) Spec. Broke in Shoulder

(2) Spec, Broke in Radius

The heating unit used for the elevated temperature flexural test is shown in Figure 5-13. The specimens, as shown in Figure 5-14, were radiantly heated by six graphite-resistance heating elements. The same temperature monitoring method as employed for the tensile tests was used. All tests were conducted in an argon atmosphere. The three-point loading method was employed in these tests, as shown in Figure 5-15. The span between supports was 4 inches. Autographic recordings of load as a function of beam deflection were obtained using the Model 680 Optron optical extensometer. The load was plotted on the autographic recording by manually transmitting a signal at fixed load increments. The formulas for computing the reported values of stress, strain, and flexure modulus are:

$$\sigma = \frac{3\ LP}{2\ Wt^2}; \quad \epsilon = \frac{6\ t\ y}{L^2}. \quad E = \frac{\sigma}{\epsilon} = \frac{L^3 P}{Wt\ 3y}$$

where:

σ = Stress in psi
ϵ = Strain in inches/inch
E = Flexural modulus in psi
L = Span in inches
P = Load in pounds
W = Specimen width in inches
t = Specimen thickness in inches
y = Beam deflection in inches

Flexural properties of the alumina matrix are shown in Table 5-8 and for the zirconia matrix in Table 5-9.

Test results in simple, three-point loading flexural tests exhibit much less scatter than the results obtained with tensile tests. Variation in test results can be attributed primarily to variation in the specimen as slight increases in porosity markedly affect strength. Concentrations of large pores, which were apparent in some test specimens, markedly affect test results.

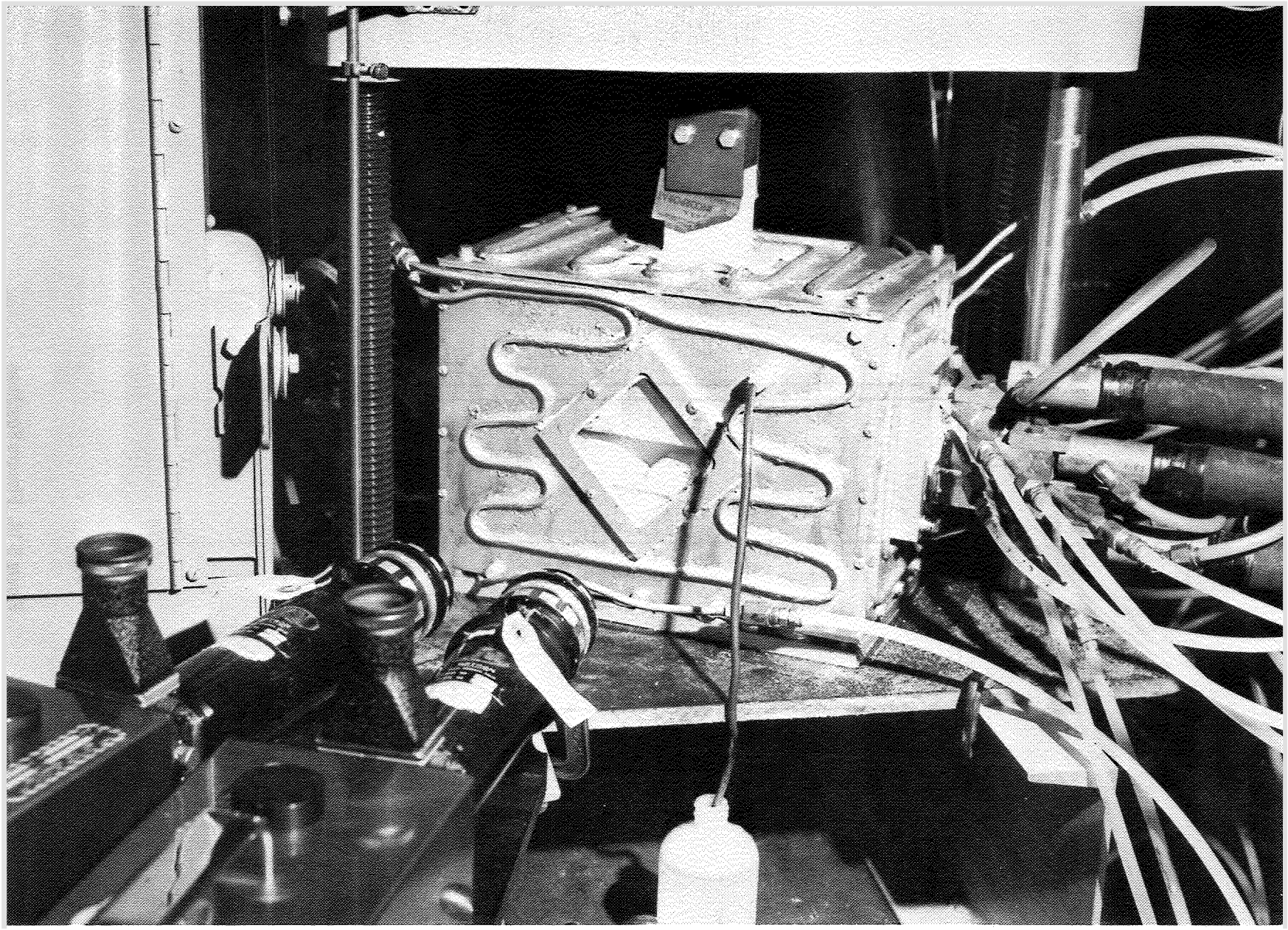

Figure 5-13. Flexure Test Furnace with Optron Extensometer

NOTE: 1. TOL. ± 1/16

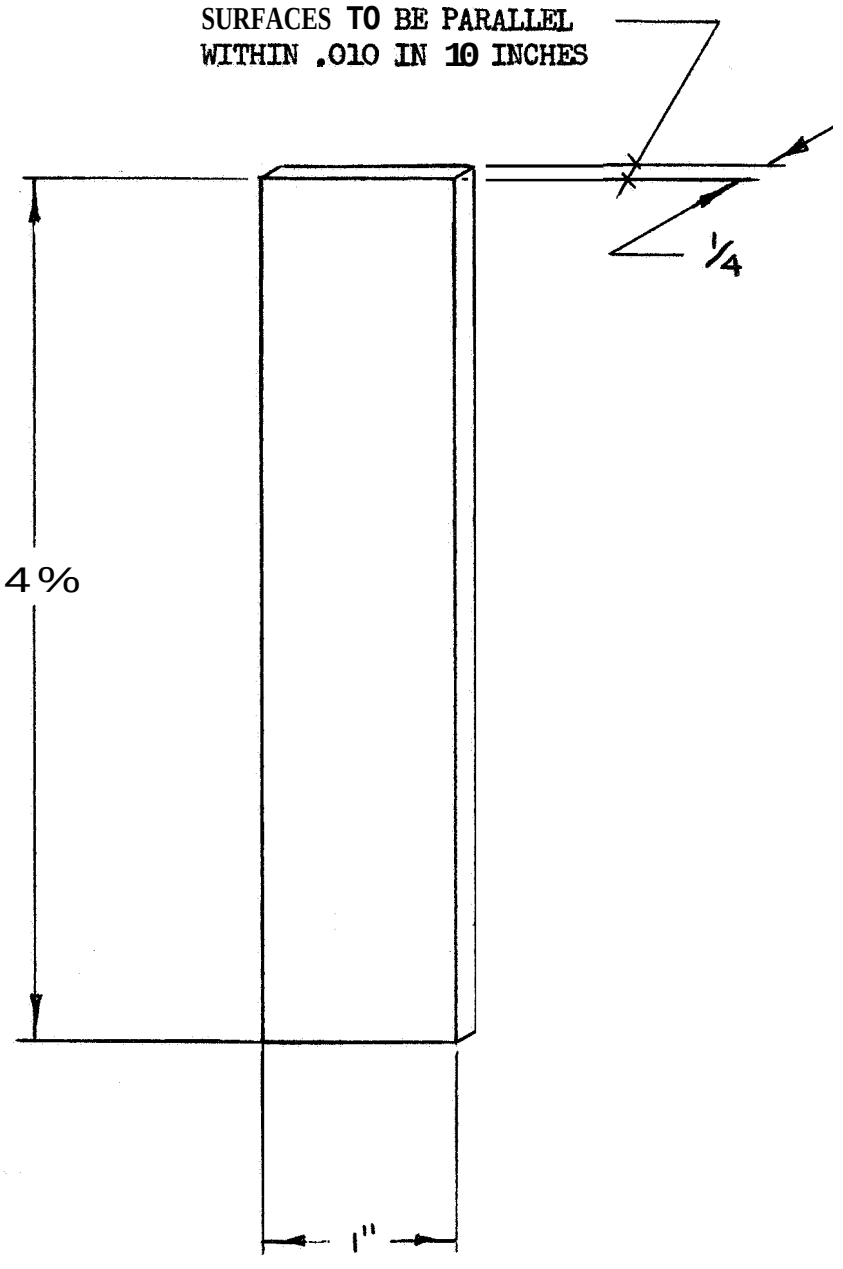

figure 5-14. Flexure Specimen

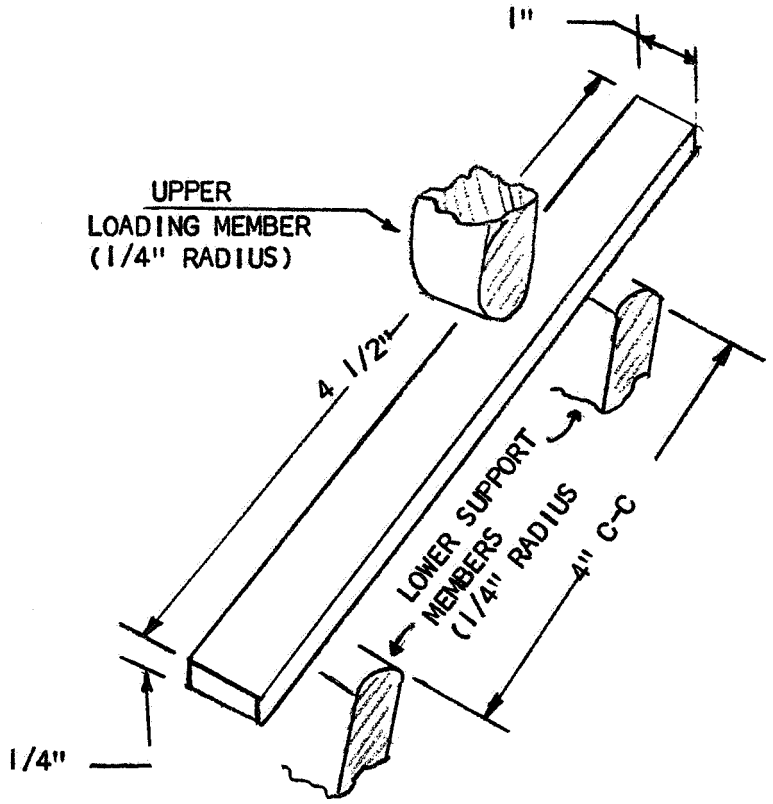

Figure 5-15. Flexural T[redacted]ng of Specimens

Table 5-8
FLEXURAL PROPERTIES OF ALUMINA MATRIX

Nominal Temp. (°F)	Spec. No.	Width (in.)	Depth (in.)	Load (lbs)	Flexure Strength (psi)	Flexure Modulus (psi X 10^{-6})
70	25	1.004	0.2530	31.0	2900	15.2
	26	1.001	0.2522	25.0	2400	13.3
	27	1.004	0.2543	64.5	6000	16.7
	29	1.004	0.2550	44.5	4100	19.2
1500	13	1.004	0.2553	28.0	2600	7.3
	14	1.005	0.2560	20.0	1800	3.7
	15	1.005	0.2558	21.5	2000	3.5
	24	1.004	0.2552	29.0	2700	4.1
2000	20	1.006	0.2560	34.5	3200	2.7
	21	1.006	0.2563	33.5	3000	3.8
	22	1.002	0.2553	19.0	1800	3.3
	23	1.005	0.2562	33.5	3100	3.7
2500	16	1.005	0.2553	3.0	280	0.48
	17	1.006	0.2552	3.5	320	0.49
	18	1.004	0.2554	4.0	370	0.38
	19	1.005	0.2535	4.0	360	0.33

5.3.3 Ring Compression Test

The ring compression tests were conducted to determine the flexural strength, flexural modulus of elasticity, and Poisson's Ratio. The ring specimen is shown in Figure 5-16.

The same furnace and temperature monitoring equipment described for flexural testing, Section 5.3.2, was used for the ring compression tests.

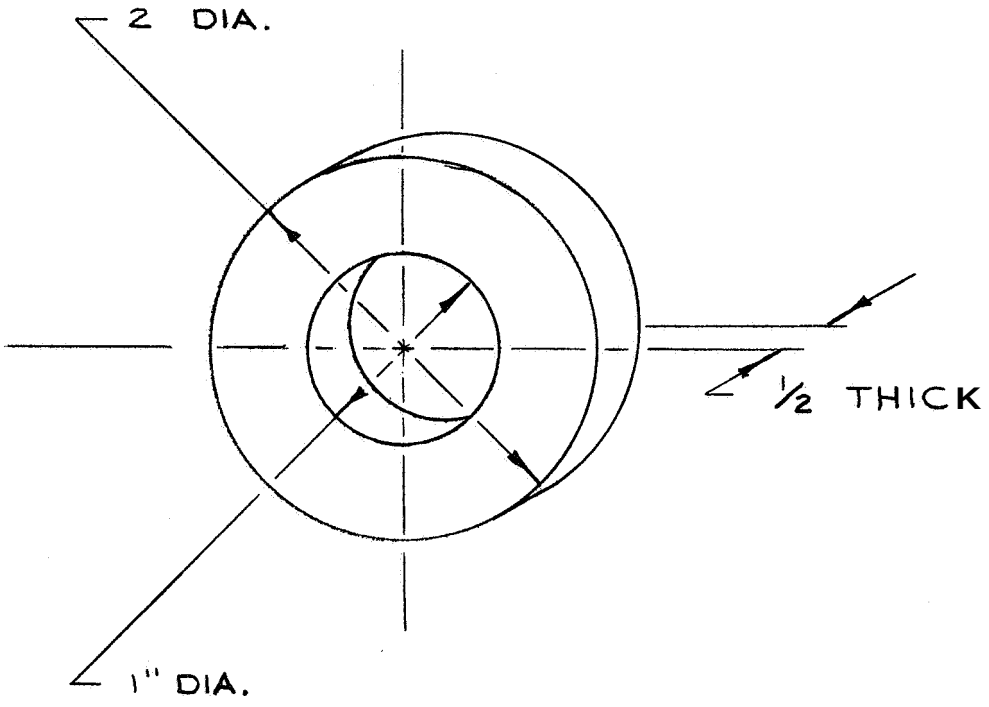

NOTE: 1, O.D. & I.D. TO BE CONCENTRIC WITHIN .005 T.I.R.
2. TOL. ± 1/32

Figure 5-16. Ring Compression Specimen

Table 5-9

FLEXURAL PROPERTIES OF ZIRCONIA MATRIX

Nominal Temp. (°F)	Spec. No.	Width (in.)	Depth (in.)	Load (lbs)	Flexure Strength (psi)	Flexure Modulus (psi X 10^{-6})
70	6	1.028	0.2956	63	4200	6.6
	7	1.028	0.3025	63	4100	6.3
	8	1.026	0.3035	56	3600	6.4
1000	9	1.029	0.3033	65.5	4200	7.2
	10	1.026	0.3015	76.0	4900	7.1
	11	1.025	0.3060	53.5	3300	8.0
1500	5	1.025	0.3043	16.5	1000	0.9
	4	1.035	0.3021	16.0	1000	0.8
	3	1.035	0.3022	25.0	1600	0.9
2000	12	1.031	0.3025	3.5	230	---
	13	1.028	0.3022	1.5	100	---

Major problems were encountered in the ring compression tests while trying to measure Poisson's ratio. Although the instrumentation was sensitive enough to detect the ring deformations under load applied across the diameter, the measured deformations were found to be very scattered. Two types of instruments were investigated and both failed to yield reliable data.

For the room temperature tests two Aminco-Tuckerman optical strain gages were tried. These instruments are capable of measuring deformations to the nearest 0.000008 inch. With one strain gage mounted to measure deformation perpendicular to the loading direction and the other mounted to measure deformation parallel to the applied load, readings were taken at various load increments. A linear relationship between deformation and applied load could

not be established, due to the large scatter in the data points. On some of the tests a linear relationship could be established, but the deformation in the parallel direction was less than the deformation perpendicular to the direction of loading; therefore, it was not possible to obtain acceptable values for Poisson's Ratio. Two Gaertner optical travel-indicating scopes were also used in an attempt to resolve the problem encountered with the Aminco-Tuckerman equipment. The results with the Gaertner's were the same as with Tuckerman gages. The Gaertner's were calibrated and found to have an accuracy of 40 micro-inches. The Gaertner scopes were used at room and elevated temperature.

The loading method was examined as a possible cause of the problem. It was felt that the load train was shifting and causing the erratic behavior and deformation. To eliminate the possibility, a die set was used to load the specimen. The results of this test did not differ from those obtained by the original loading method. It is felt that local crushing of the specimen was the source of the problem. As local crushing occurs, the point of load application on the specimen shifts and causes erratic deformation to occur.

Although values for Poisson's Ratio could not be obtained from the ring compression tests, the flexural strength values were obtained. The data obtained from the ring compression tests for alumina are shown in Table 5-10 and the data for zirconia are presented in Table 5-11.

5.3.4 Shear Tests

The shear test fixture was composed of two pieces; the bottom or solid piece was 1" x 4 1/2" with a 1 cavity in the center. The top or ram was 1" square and applied the load across the entire section between the notches. The notches on the specimens were 0.050" deep, and the area for determining the shear strength was computed using the area at the notches. The fixture was cast from the same material as that being tested. The same furnace and temperature monitoring devices were used for the shear tests as were described for the flexure tests. In the shear testing, it was found that notching of the specimens at the shear planes was required to assure failure at the desired location (Figure 5-17). Without the notches, the specimens had a tendency

Table 5-10

RING COMPRESSION TEST DATA FOR ALUMINA MATRIX

Nominal Temp. (°F)	Spec. No.	Width t (in.)	Thickness b (in.)	Radius R (in.)	Load P (lbs)	Flexural Stress (psi)
70	1	0. 503	0. 5106	0.753	334	4640
	4	0. 504	0. 5107	0.753	307	4257
	5	-----	----	---	---	----
	6	0. 506	0. 5109	0.754	323	4518
1500	11	0. 505	0. 5089	0.754	172	2390
	12	0. 503	0. 5082	0.753	202	2434
	16	0. 505	0. 5024	0.754	168	2364
2000	8	0.499	0. 5058	0. 749	266	3749
	14	0. 503	0. 5103	0.753	188	2609
	15	0. 506	0. 5113	0.755	171	2357
2500	21	0. 503	0.4983	0. 752	44	626
	22	0. 503	0.4985	0. 752	25	356
	23	0. 503	0. 5001	0.753	32	454

$$\text{Flexure } \sigma = \frac{P}{A\pi\left[1 + Z\right]}\left[1 - \frac{1}{Z}\left(\frac{t}{2R-t}\right)\right]$$

Where: A = bt

$$Z = \frac{1}{3}\left(\frac{t}{2R}\right)^2 + \frac{1}{5}\left(\frac{t}{2R}\right)^4 + \frac{1}{7}\left(\frac{t}{2R}\right)^7$$

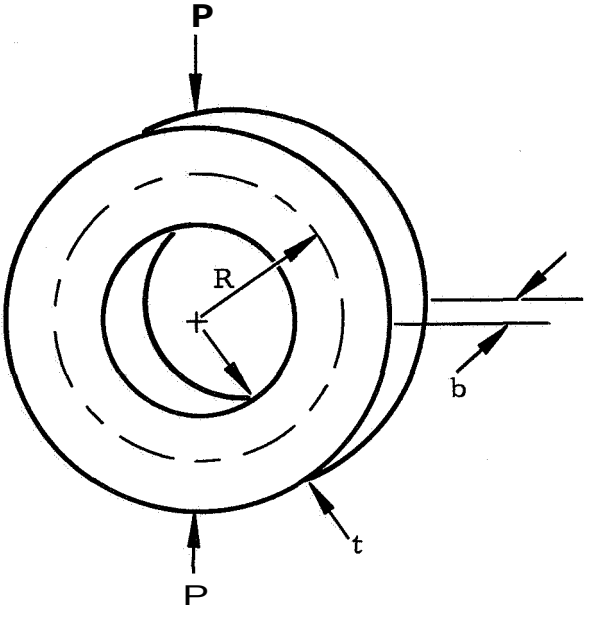

Table 5-11

RING COMPRESSION TEST DATA FOR ZIRCONIA MATRIX

Nominal Temp. (°F)	Spec. No.	Width t (in.)	Thickness b (in.)	Radius R (in.)	Load P (lbs)	Flexure Stress (psi)
70	2	0. 503	0. 5100	0.753	298	4148
	3	0. 503	0. 5098	0.753	280	3899
	7	0. 503	0. 5090	0. 751	242	3385
1000	18	0. 504	0. 5090	0.753	340	4730
	19	0. 503	0. 5100	0.753	392	5452
	20	0. 503	0. 5085	0.755	318	4432
1500	10	0. 503	0. 5089	0.753	70	975
	13	0. 501	0. 5094	0. 751	116	1620
	17	0. 501	0. 5075	0.751	64	897
2000	9	0. 503	0. 5102	0.753	22	306

to fail in bending at the midpoint between the shear planes. All shear tests were conducted with notched specimens. The results obtained for the alumina shear tests are shown in Table 5-12, and the shear test results for zirconia are presented in Table 5-13. In view of the mode of failure and the possibility of stress concentration due to the notch, these data are considered questionable.

5. 3. 5 Anchoring of the Reinforcement

To establish the anchoring strength of the reinforcement, preliminary tests were first conducted on the loads required to pull out from the zirconia matrix a 49-strand steel cable cons'isting of 0. 010" diameter wires. The embedment length of the cables ranged from 0. 75" to 2. 03". A linear relationship was found to exist between the pullout load and the embedded lengths. Assuming

NOTE: 1. TOL. ± 1/16

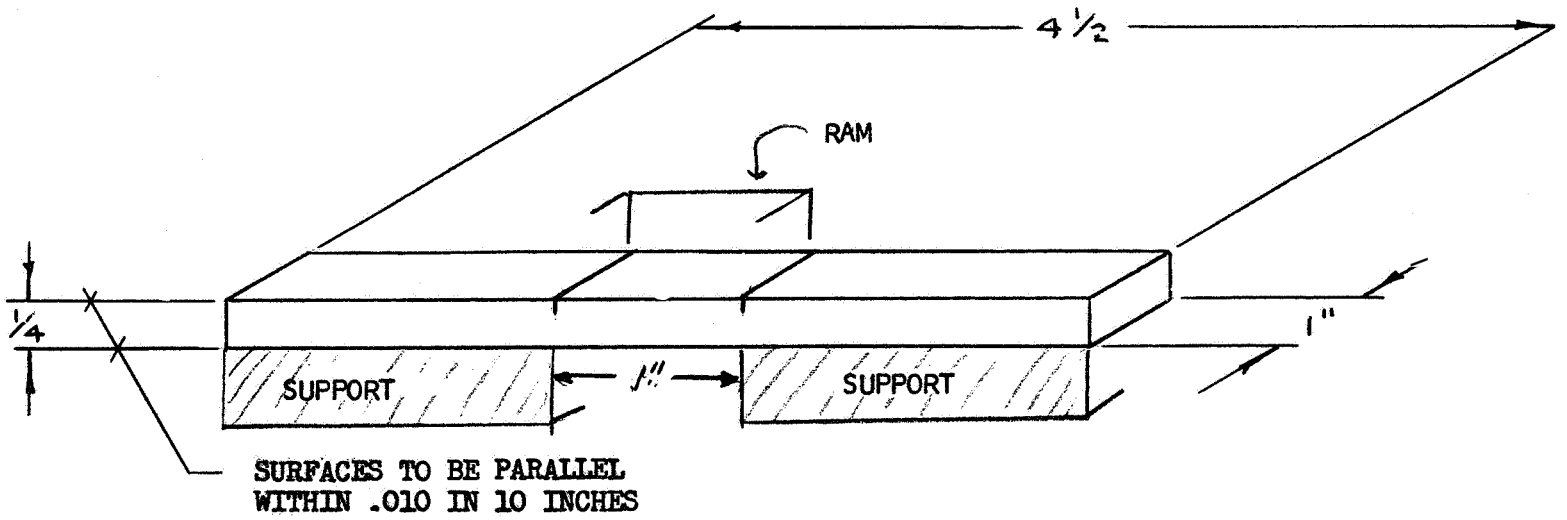

Figure 5-17. Shear Specimen

Table 5-12

SHEAR PROPERTIES OF ALUMINA MATRIX

Nominal Temp. (°F)	Spec. No.	Width W (in.)	Thickness t (in.)	Area A (in^2)	Load P (lbs)	Stress (psi)
70	1	1.000	0.1325	0.265	230	870
	3	1.004	0. 1493	0.300	120	400
	15	1.004	0. 1456	0.293	180	615
	16	1.001	0. 1234	0.247	165	668
1000	22	1. 002	0. 1272	0.255	235	920
1500	14	1.006	0. 1481	0.297	75	252
	18	1.001	0. 1381	0.264	158	600
	19	1. 001	0. 1277	0.255	64	250
2000	5	1.004	0. 1434	0.288	61	212
	23	1.002	0. 1274	0.235	109	475
	20	1.007	0. 1316	0.265	12	45
2500	24	1.005	0. 1273	0.256	40	156
	25	1.004	0. 1347	0.296	107	362
	26	1.002	0. 1290	0.258	60	233

$$\text{Shear Stress} = \frac{\text{Load}}{\text{Area}}$$

Area = 2 (Width X Thickness)

a triangular shear load transfer distribution from the cables to the matrix, the following equation was found to govern the pullout strength for the range investigated:

$$P = 3940\ \pi R \ell \qquad (5.3.5\text{-}1)$$

Table 5-13

SHEAR PROPERTIES OF ZIRCONIA MATRIX

Nominal Temp. (°F)	Spec. No.	Width W (in.)	Thickness t (in.)	Area A (in.)	Load P (lbs)	Stress (psi)
70	1	1.010	0.1588	0.320	201	627
	2	1.010	0.1557	0.320	223	698
	3	1.010	0.1559	0.319	80	251
1000	21	1.040	0.1526	0.317	172	542
	4	1.010	0.1585	0.325	95	292
	5	1.010	0.1563	0.316	107	339
1500	11	1.027	0.1334	0.274	14	51
	13	1.028	0.1669	0.343	195	568
	20	1.043	0.1573	0.320	101	316
2000	6	1.025	0.1489	0.305	18	59
	7	1.025	0.1571	0.321	10	35
	8	1.025	0.1652	0.338	44	130
	10	1.025	0.1656	0.320	45	140
	17	1.027	0.1523	0.312	46	147

Where P is the pullout load, ℓ is the embedment length of the cable, and R is the radius of the shear circle; that is, the smallest circle which includes all the wires of the 49-strand cable. The constant in the above equation represents the maximum shear strength. The highest average shear strength that was developed was $\tau_{AVE} = 2,180$ psi. Using the results of the tests on steel cable and the theoretical results of Section 5.1, embedment lengths for the tungsten cables were determined so as to achieve good mechanical anchoring.

The chemically consolidated castable zirconia was cast into a 1" x 1" x 5" die cavity reinforced with a 21-strand cable at each of the four corners. Holes were drilled in the center of each end of the mold to introduce the test cables, At one end of the mold, measured lengths of the test cable were introduced into the "as-cast" matrix through the holes. At the other end of the mold, cables were placed at a greater depth to assurepullout of the measured length, if pullout occurred. A ten-inch length of cable was retained on each end to allow for gripping. **A** photograph of the anchoring test specimens is shown in Figure 5-18.

The furnace used for the elevated temperature anchoring test was a small, Douglas-built, platinum wire-wound furnace. The free ends of the cables were gripped outside the furnace to eliminate the problems associated with hot gripping. The cables were gripped with wedge action jaws. The anchoring tests consisted of loading the cables in tension until shear failure between the cable and matrix occurred, or the cable failed in tension. The elevated temperature test specimens were heated to test temperature, allowed to stabilized, and the load was then applied.

The experimental results on the anchoring ability of tungsten cables at room and elevated temperatures are shown in Tables 5-14 and 5-15. Several important observations can be made from the data contained in these tables. The reinforcement configurations were sufficient to develop the full load-carrying ability of the cables at room temperature. The stresses at which the cables failed during the pullout tests were higher than those reported in Tables 5-4 and 5-5. For a 49-strand cable, the average stress at which cable failure occurred was 315×10^3 psi as compared to a value of 293×10^3 psi reported in Table 5-5. For a 21-strand cable, the average stress at which cable failure occurred was 316×10^3 psi as compared to a value of 287×10^3 psi given in Table 5-4. From the data presented in Table 5-15 it appears that the true shear strength of the ceramic is greater than 6,880 psi. This value is almost an order of magnitude higher than the measured values of shear strength reported in Table 5-12.

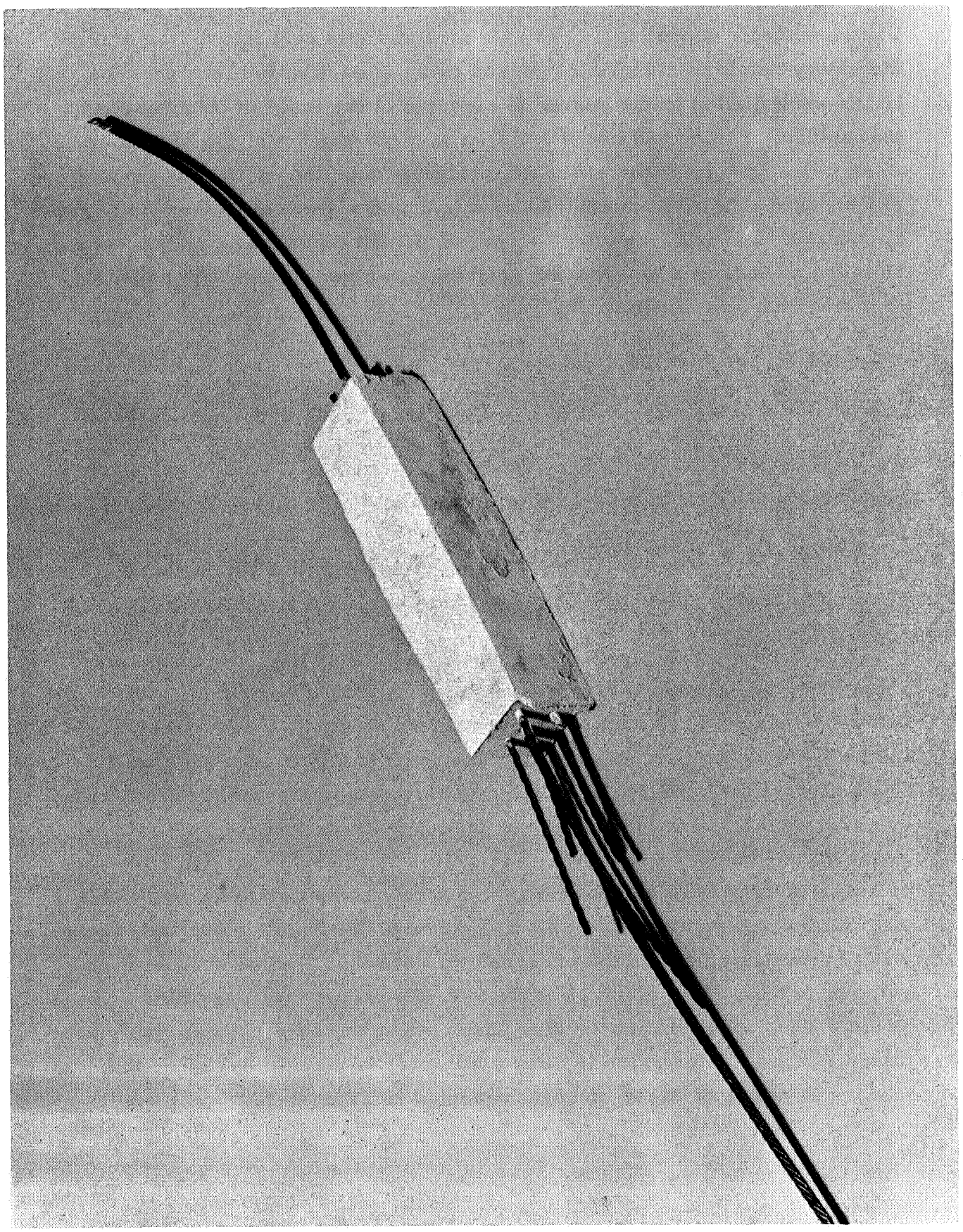

Figure 5-18. Anchoring Test Specimen (1/2x)

LOADS REQUIRED TO PULL OUT 21-STRAND TUNGSTEN CABLE FROM ZIRCONIA MATRIX

Temperature (°F)	Specimen No.	Imbedment Depth (in)	Pullout Load (lbs)	Wire Stress at Failure X 10^{-3} psi	Average Shear* Stress At Failure (X 10^{-3} psi)	Remarks
70°	1	1.62	750	316	1.97	Cable failure
	2	1.60	750	316	1.99	Cable failure
	3	1.61	755	318	1.99	Cable failure
	4	1.10	750	316	2.90	Cable failure
	5	1.10	750	316	2.90	Cable failure
	6	1.12	740	312	2.80	Cable failure
	7	1.10	750	316	2.90	Cable failure
	8	0.68	750	316	4.68	Cable failure
	9	0.71	755	318	4.51	Cable failure
	10	0.70	755	318	4.58	Cable failure
	11	0.69	660	278	4.05	Ceramic fracture
1500	12	1.6	80.4	33.8	0.21	Pullout
	13	1.6	192	81.0	0.51	Ceramic fracture
	14	1.6	214	90.0	0.57	Pullout
	16	1.1	82	34.5	0.32	Catastrophic ceramic failure
	17	1.1	90	37.9	0.35	Pullout
	18	0.7	160	67.5	0.97	Cable oxidized
	19	0.7	166	70.0	1.01	Pullout
	20	0.7	97	40.8	0.59	Pullout
2000	22	1.6	36.2	15.2	0.096	Ceramic fracture
	23	1.6	60.4	25.4	0.16	Cable oxidized
	24	1.1	76.2	32.1	0.29	Ceramic fracture
	25	1.1	39.0	16.4	0.15	Cable failure
	26	0.7	34.0	14.3	0.13	Pullout
	27	0.7	45.6	19.2	0.28	Ceramic fracture
	28	0.7	44	18.5	0.27	Ceramic fracture
	29	0.7	16.6	7.0	0.10	Cable oxidized

*The radius of the shear circle for the 21-strand cable was 0.038"

Table 5-15

LOADS REQUIRED TO PULL OUT 49-STRAND CABLE FROM ZIRCONIA MATRIX

Temperature (°F)	Specimen No.	Imbedment Depth (in)	Pullout Load (lbs)	Wire Stress at Failure X 10^{-3} psi	Average Shear* Stress at Failure (X 10^{-3} psi)	Remarks
70°	1	2.49	1355	245	1.57	Cable failure
	2	2.50	1745	315	2.02	Cable failure
	3	2.48	1750	316	2.04	Cable failure
	4	1.50	1745	315	3.36	Cable failure
	5	1.50	1740	315	3.36	Cable failure
	6	1.48	1740	315	3.40	Cable failure
	7	1.48	1730	313	3.38	Cable failure
	8	0.74	1720	311	6.72	Cable failure
	9	0.74	1760	318	6.88	Cable failure
	10	0.76	1750	316	6.68	Ceramic fracture
	11	0.75	1300	235	5.01	Ceramic fracture
1500	12	0.75	65	11.7	0.25	Pullout
	13	0.75	96	17.3	0.37	Pullout
	14	0.75	94	17.0	0.36	Pullout
	15	1.5	66	11.9	0.13	Pullout
	16	1.5	67	12.1	0.13	Pullout
	17	1.75	222	40.0	0.43	Ceramic fracture
2000	18	0.75	62.4	11.3	0.24	Pullout
	19	0.75	25.2	4.6	0.10	Pullout
	21	1.5	83.4	15.1	0.16	Ceramic fracture
	22	1.5	80.6	14.6	0.16	Ceramic fracture
	23	1.5	19.2	3.5	0.04	Pullout

*The radius of the shear circle for the 49-strand cable was 0.055"

5. 3. 6 Compression Modulus of Zirconia Matrix

Three compression modulus specimens of chemically consolidated zirconia (1" x 1" x 2") were prepared using the following composition:

60 parts by weight	-60 + 200 mesh ZrO_2
40 parts by weight	-325 mesh ZrO_2
6 parts by weight	$NH_4H_2PO_4$
8 parts by weight	H_2PO_3F

Compression modulus tests on the three specimens were conducted at room temperature using a 60 K Baldwin Tensile test machine. The specimens were instrumented with strain gages on the 1" x 2" side, the surface of the 1" x 1" sides was lubricated with a dry lubricant to reduce the possibility of retarding the slippage at the surfaces of applied pressure. The results of the tests are presented in Table 5-16.

Table 5-16
COMPRESSION PROPERTIES OF ZIRCONIA MATRIX

Specimen NO.	Compression Strength (psi)	Compression Modulus ($X 10^{-6}$ psi)
1	35,400	10.78
2	30,200	11.37
3	35,000	11.83
Average	33, 530	11.33

5.3.7 Thermal Expansion

The linear thermal expansion of the alumina matrix was determined in the range of 70°F (21.2°C) and 2,800°F (1,538°C) and for zirconia matrix from 70°F (21.2°C) to 3,200°F (1,760°C). The curves obtained for the chemically consolidated matrices are compared to curves for pressed and sintered materials as shown in Figures 5-19 and 5-20. Thermal expansion was determined from room temperature to 1,800°F (982°C) with a silica dilatometer. Above 1,800°F (982°C) the expansion was determined with a dual-image extensometer.

5.4 REFERENCES

1. L. B. Greszczuk, Elastic Constants and Analysis Methods for Filament Wound Shell Structures, Douglas Report SM-45849, January 1964.
2. A. Goldschmitt, Thermophysical Properties of Solid Materials, WADC Technical Report 58-476, Vol. III, Page 45, 1959.
3. Ibid, Page 279.

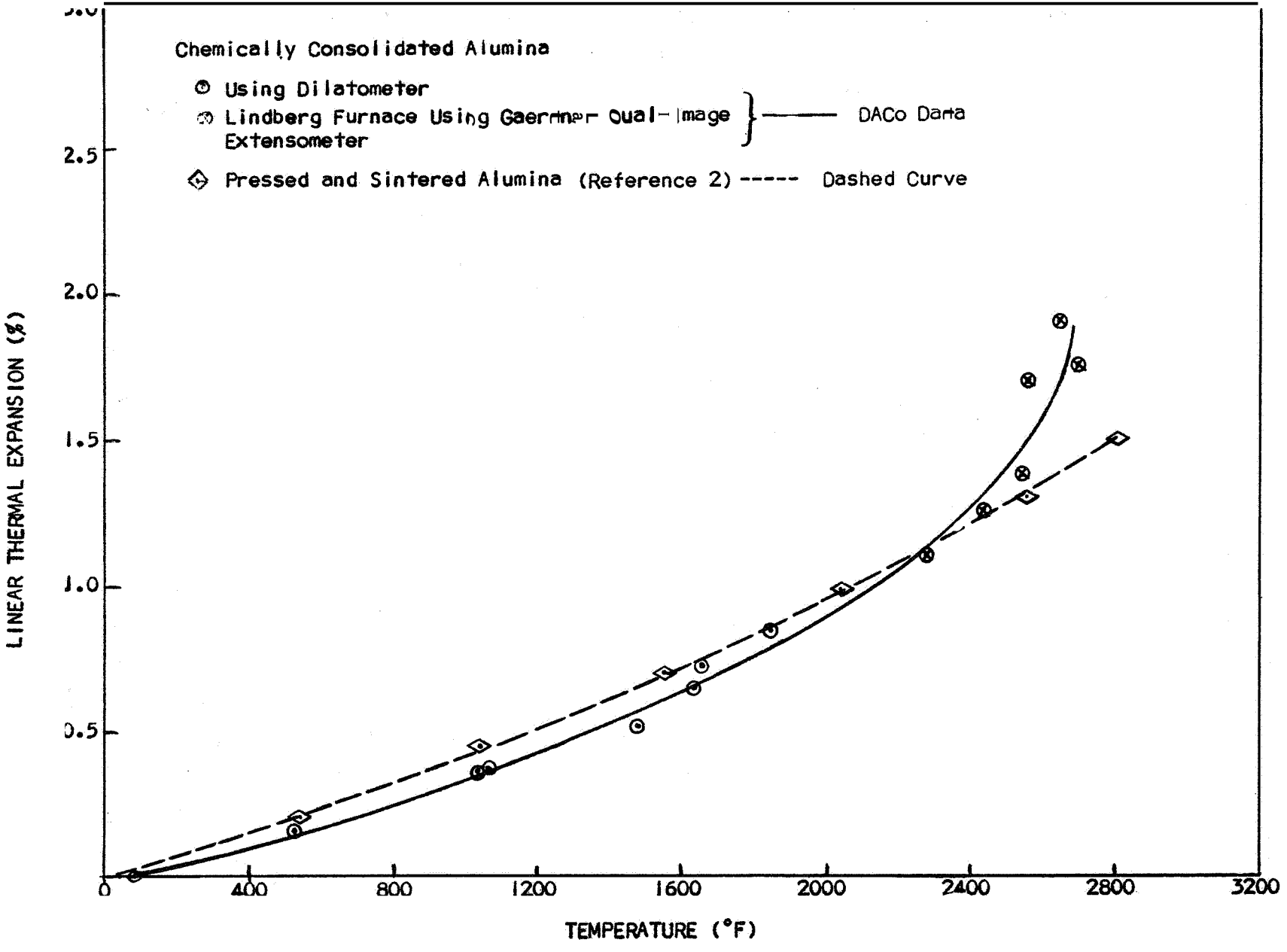

Figure 5-19. Linear Thermal Expansion of Chemically Consolidated Alumina as Compared to Sintered Alumina

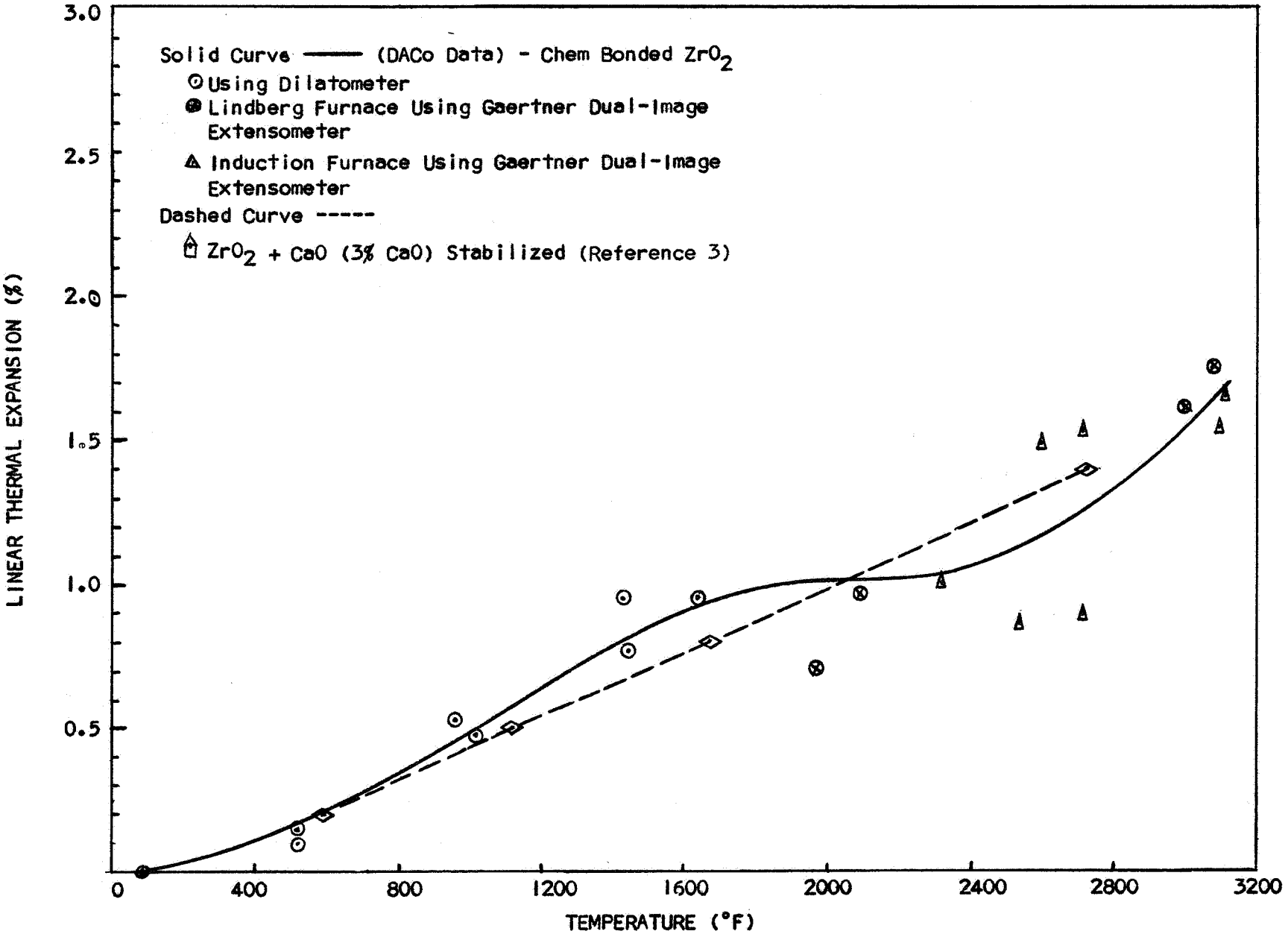

Figure 5-20. Linear Thermal Expansion of Chemically Consolidated Zirconia as Compared to Calcia Stablized Sintered Zirconia

SECTION 6
DESIGN AND FABRICATION OF PRESTRESSED TEST SPECIMENS

To demonstrate the feasibility of prestressing brittle materials, and to verify the theoretically predicted increases in load carrying ability of prestressed ceramics, the specimens were designed, fabricated and tested. The results presented here were based on theoretical analysis developed in Section 3 and the test results given in Section 5. This section also describes the apparatus and methods of imparting prestress.

6.1 DESIGN OF PRESTRESSED TEST SPECIMENS

Using the equations given in Section 3.2 in combination with the experimentally obtained properties of the constituent materials given in Section 5.1 and 5.2, calculations were made on the relationship between composite tensile strength and the initial prestress, temperature, thermal prestress, percent of reinforcement, reinforcement configurations, and the thermal, elastic, and strength properties of the constituents. These calculations were based on properties of ceramics obtained from flexural tests and the experimentally obtained properties of the reinforcement given in Tables 5-4 and 5-5. Typical results are shown in Figures 6-1 and 6-2 where the envelopes for tensile strength of prestressed ceramics are given. In arriving at these results, the variation of material properties with temperature was taken into consideration. The results are, however, based on elastic analysis. The composite stresses shown are the stresses which would initiate the failure in the ceramic or the reinforcement. For any given prestress, the upper horizontal portion of the curve represents the composite stress which will cause failure in the ceramic (without necessarily failing the reinforcement); the steep portion of the curve represents the composite stress required to cause failure of the reinforcement (without necessarily causing failure in the ceramic); and the lower horizontal portion of the curve

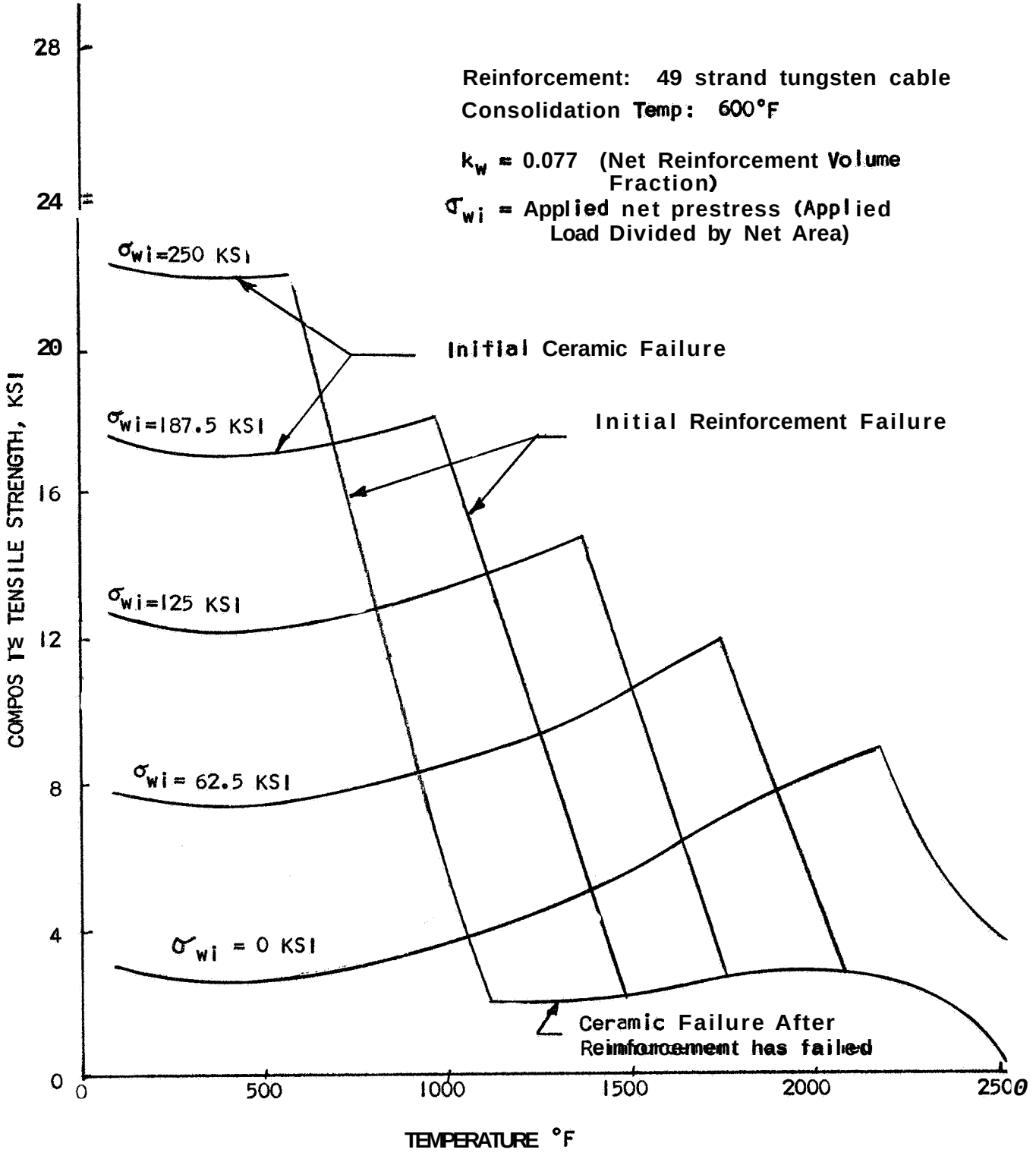

Figure 6-1. Tensile Strength of Prestressed Alumina at Elevated Temperatures

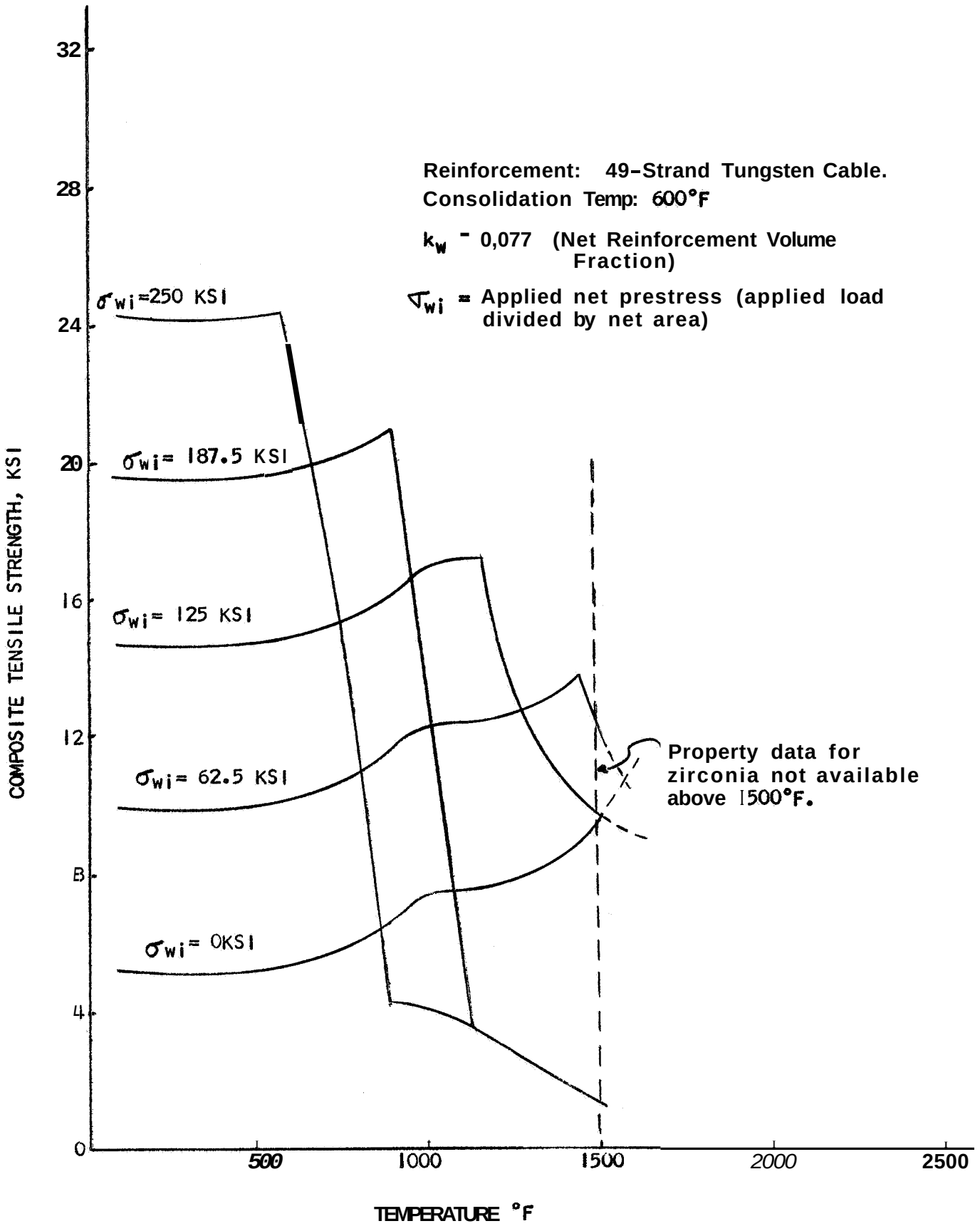

Figure 6-2. Tensile Strength of Prestressed Zirconia at Elevated Temperatures

represents the composite stress required to fail the ceramic after the reinforcement has failed. One more curve could be added to these graphs - the composite stress required to fail the reinforcement, after the ceramic has failed. However, for purposes of clarity, the latter curve has been deleted. It is worth noting here that if the reinforcement breaks or does not develop its load carrying ability due to poor anchoring, then the strength of the reinforced composite will be lower than that of the ceramic by itself, as is shown by the lower horizontal portion of the curve.

From Figures 6-1 and 6-2 it is apparent that for structural applications where temperatures below 600°F (316°C) are encountered, a high mechanical prestress is desirable to obtain a composite of high tensile strength. For high-temperature structural applications, the induced thermal prestress may be sufficient to increase the composite tensile strength to a desired level. For combinations of materials other than those discussed here, the thermal prestress may be detrimental to the composite strength, and therefore high mechanical prestress may be desired to achieve high-strength composites for elevated temperature application.

On the basis of information such as that shown in Figures 6-1 and 6-2, two prestress levels were selected - a prestress of 190×10^3 psi to demonstrate a high composite strength at low temperatures, and a prestress of 50×10^3 psi to demonstrate a high composite strength at high temperatures. When the prestress levels and the reinforcement configurations had been selected, the specimens were fabricated and tested.

6.2 PRESTRESSING FIXTURE DESIGN AND DEVELOPMENT

To fabricate the prestressed ceramic specimens, a fixture was designed to accommodate cables having diameters of 0.075 inch (3 x 7) or 0.110 inch (7 x 7), for flexural or tensile test specimen blanks. A working drawing of the assembled fixture is shown in Figure 6-3. The detailed designs of the load adjustment device, load cells, and cable positioning guide are shown in Figure 6-4. A photograph of the prestressing frame with the mold for casting of specimens mounted in position is shown in Figure 6-5. The frame was designed to permit application of load from either end. The

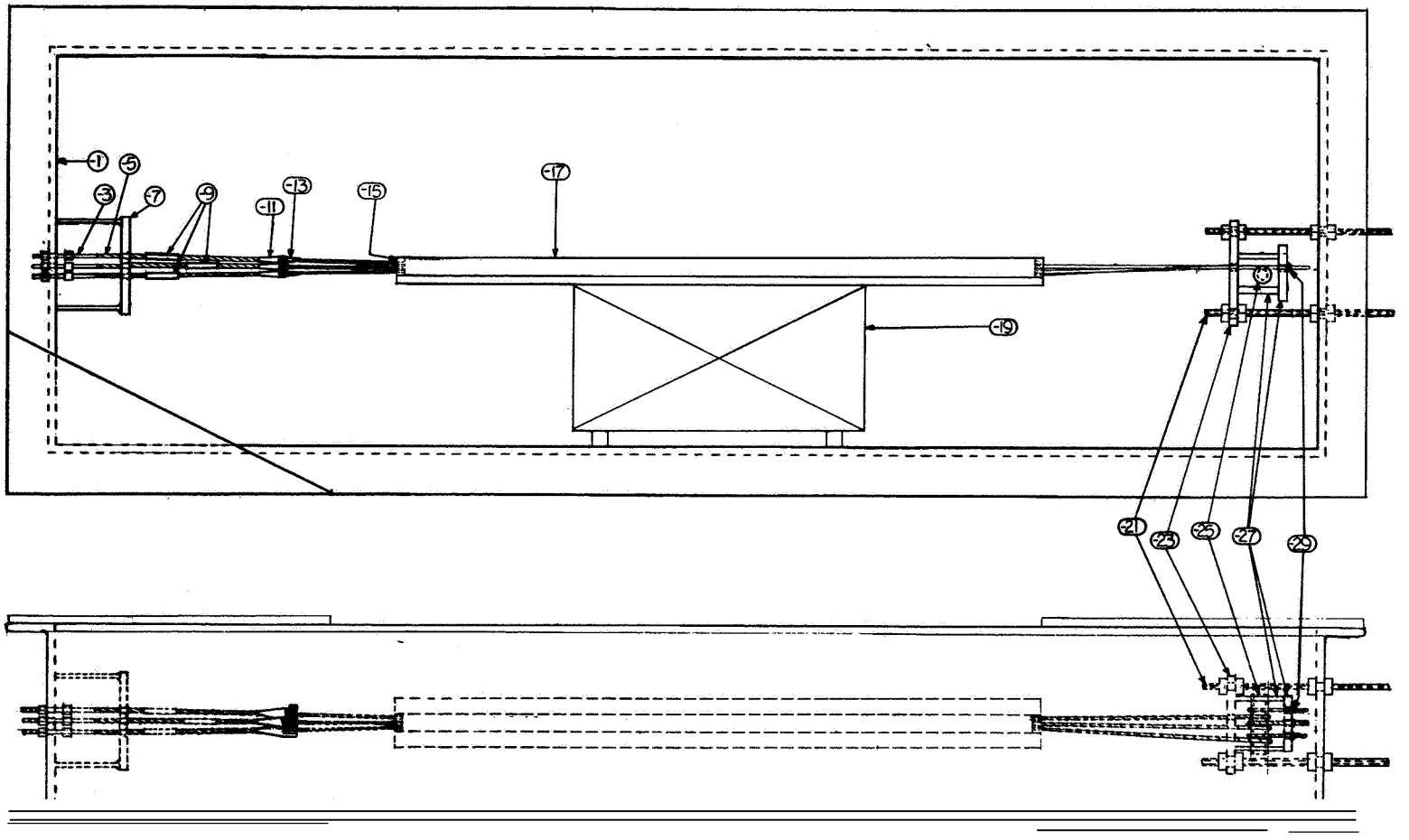

-29	MS 20663 TERMINAL BALL; USED AS A CABLE STOP. HAND SWAGED.
-27	ANCHOR POSITIONING DEVICE; L.C. STEEL.
-25	FRICTION ANCHOR; THREADED STEEL STOCK
-23	REINFORCING CABLE GUIDE; 4340 STEEL
-21	3/4-IN. THREADED BOLTS; 4 REQ'D.
-19	SYNTRON ELETRIC VIBRATOR MODEL VP 30

Figure 6-3. Cable Prestressing Fixture

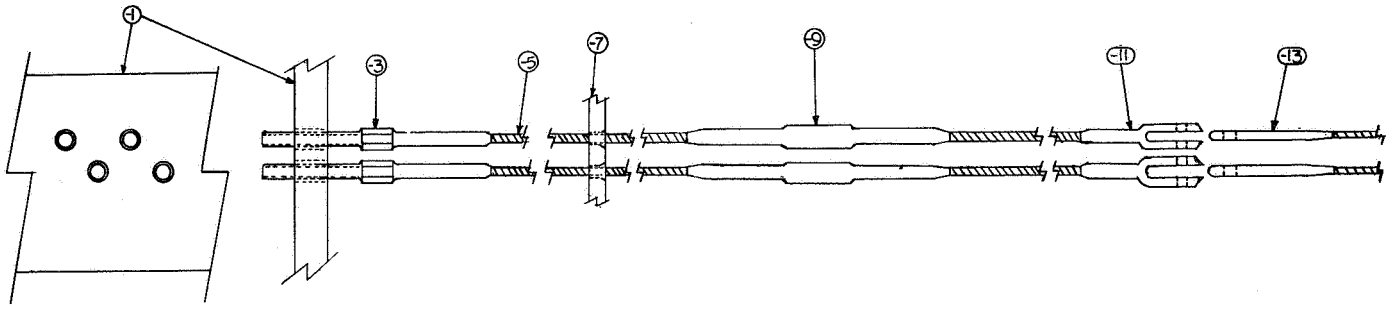

DETAIL OF CABLE TIGHTENING APPARATUS, LOAD CELLS AND CABLE FORKS

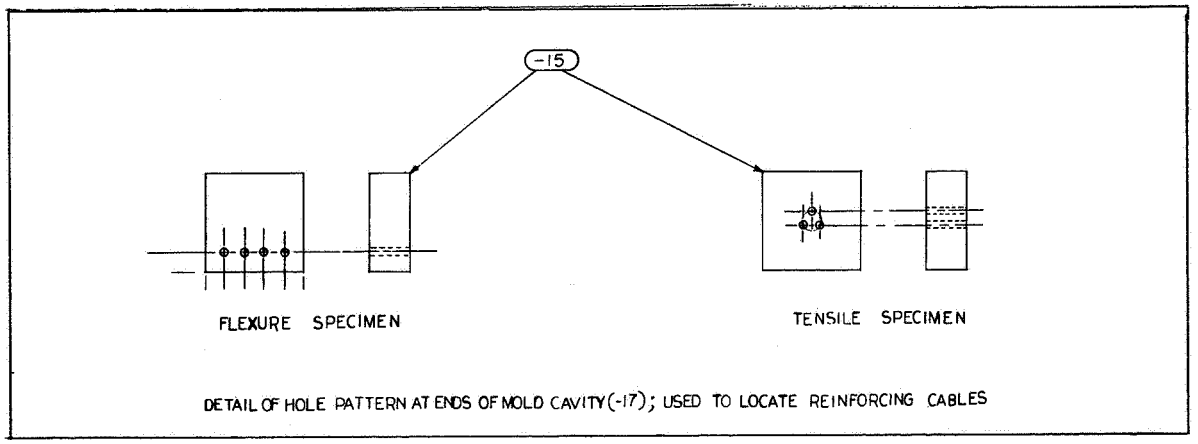

DETAIL OF HOLE PATTERN AT ENDS OF MOLD CAVITY (-17); USED TO LOCATE REINFORCING CABLES

-15	REINFORCING CABLE GUIDES; 2 EACH REQ'D. 4340 STEEL
-13	AN 668 CABLE EYE; OPTIONAL SIZE AS REQ'D. SWAGED PER DPS 10251.
-11	MS 21260-5 CABLE FORK; SWAGED PER DPS 10251
-9	CALIBRATED STAINLESS STEEL LOAD CELLS. SWAGED PER DPS 10251.
-7	LINE GUIDE; IDENTICAL HOLE PATTERN AS -1
-5	5/32-IN. CABLE (MIL-W-1511)
-3	MS 21259-5R; 4 REQ'D. FINE ADJUSTING DEVICE SWAGED PER DPS 10251.
-1	FRAME, SHOWING HOLE PATTERN

Figure 6-4. Detail of Prestressing Fixture

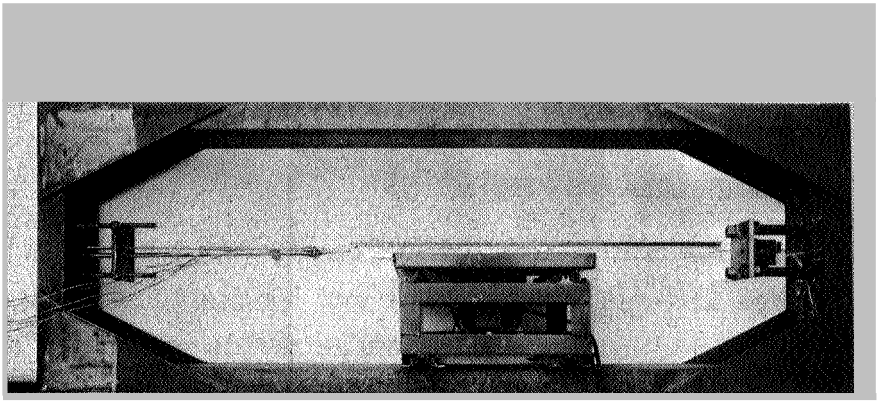

Figure 6-5. Prestressing Fixture Showing Mold Mounted in Position on Vibrating Table with Load Cell on Left

stresses applied on the cables were determined with load cells calibrated from 0 to 1,500 pounds using a Budd Model P-350 resistance bridge indicator.

The load cell is attached to a 5/32-inch diameter steel cable which has a threaded cable terminal on one end and a cable fork on the other. These fittings are swaged to the cable. The cable forks are used to join the tungsten reinforcing cable to the steel cable as shown in Figure 6-4. The threaded cable terminal, in conjunction with a tensioning nut, is used to apply the prestressing loads. The cables are aligned as shown in Figure 6-6 by use of a guide having holes which mate with holes in the frame through which the threaded cable terminals pass. On the other end of the frame, 3/4-inch threaded studs attached to a friction anchor are used for the coarse adjustment as shown in Figure 6-7.

6.3 MOLDS FOR FLEXURAL SPECIMENS

Molds were fabricated of aluminum, with a cavity 3/8 x 1 1/8 x 43 inches, with removable sides and end blocks. The end blocks were designed to be used as positioning guides for the cables. The molds permitted all flexural specimens of one prestress level to be cast at the same time, The finished flexural specimens are 1/4 x 1 x 4 inch reinforced with four equally spaced cables.

Stressing procedures were as described below. The cables were cut into 56-inch lengths, and cable eyes (AN668) were swaged on one end. The cables were threaded through the positioning end blocks. A four-wire positioning end block with cables in place is shown in Figure 6-8. The mold cavity was lined with Teflon tape to provide release of the cast specimen. The dimensions of the mold cavity were oversize to allow for machining of the specimens. After the cables were strung through the positioning blocks, the cable eye was fitted to the cable fork of the steel cable and attached with a steel pin. The free end of the reinforcing cable was passed through an alignment guide, around a threaded friction anchor, and through a stop plate, A cable ball, MS 20663, was hand swaged to the free end of the cable. This procedure was followed for each cable used. The friction anchor

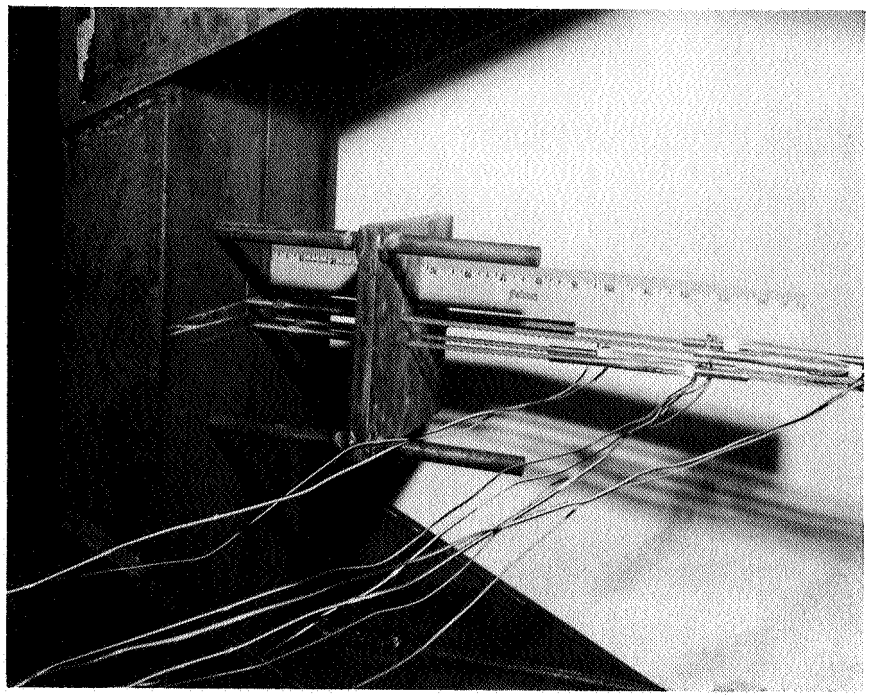

Figure 6-6. **Load Cells and Tensioning Lugs**

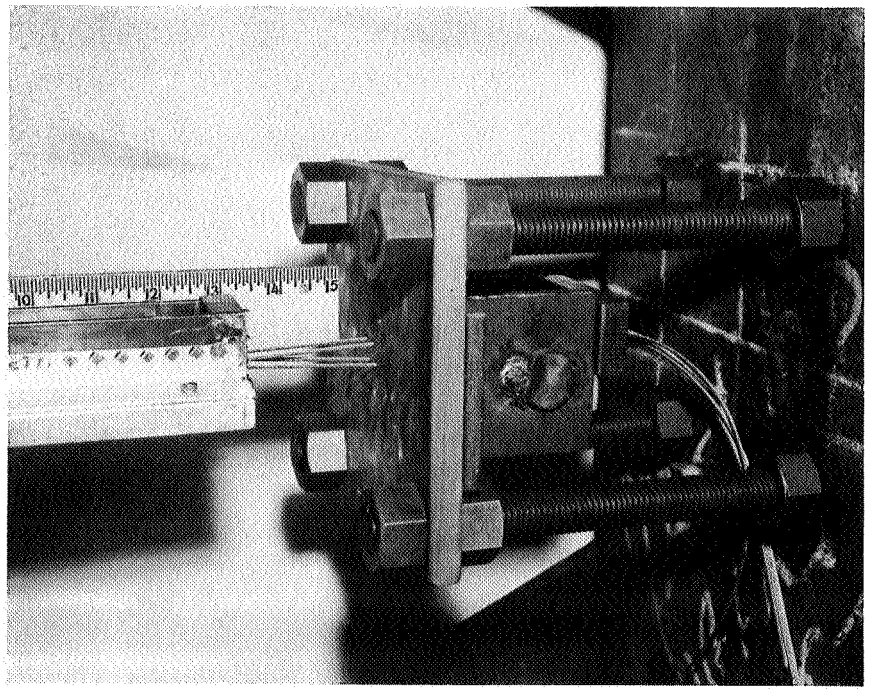

Figure 6-7. Adjustable Cable Anchoring Device

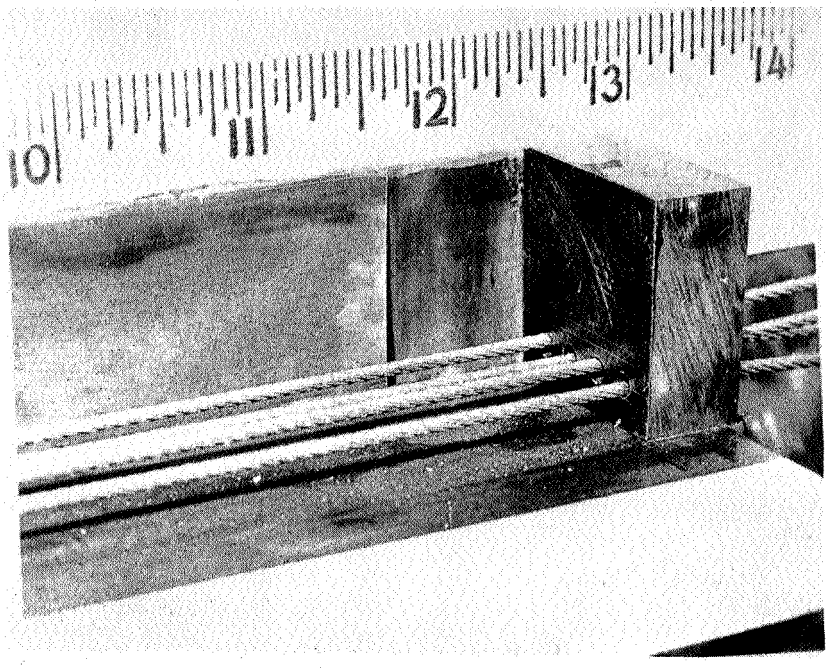

Figure 6-8. Cable Positioning Guide

consists of a piece of threaded steel rod welded in place. The radius of the friction anchor exceeded the minimum bending radius of the tungsten cable.

After the required number of cables were joined and anchored, the coarse adjusting screws were hand tightened. Each cable was tightened by means of a tensioning nut, shown in Figure 6-4, to a predetermined strain indicated by the calibrated load cell. The castable mix was then introduced into the mold cavity, vibrated to obtain flow around the cables, and cured with an electric heater blanket. After curing, strain gages were mounted on two sides of the specimens. The specimens were then placed in compression by loosening the tensioning nut, and the precompression on the ceramic was recorded by the use of strain gages. After recording, the gages were no longer required. The specimen blanks were identified and ground to the test configuration dimensions.

6.4 MOLDS FOR TENSILE SPECIMENS

Molds for the tensile specimens were fabricated of aluminum with a Teflon-tape-lined cavity 13/8" x 13/8" x 39". Each mold produced three tensile specimens of the same level of prestress. The finished tensile specimens were 1-inch diameter in the grip section with 1/2-inch diameter test section, and 12-inches long, reinforced with three cables equally spaced on a 1/8" radius, 120° apart in the 1/2" diameter gage section as shown in Figure 6-9.

The stressing procedure for the tensile specimens is the same as described in 6.3-1 for the flexural specimens.

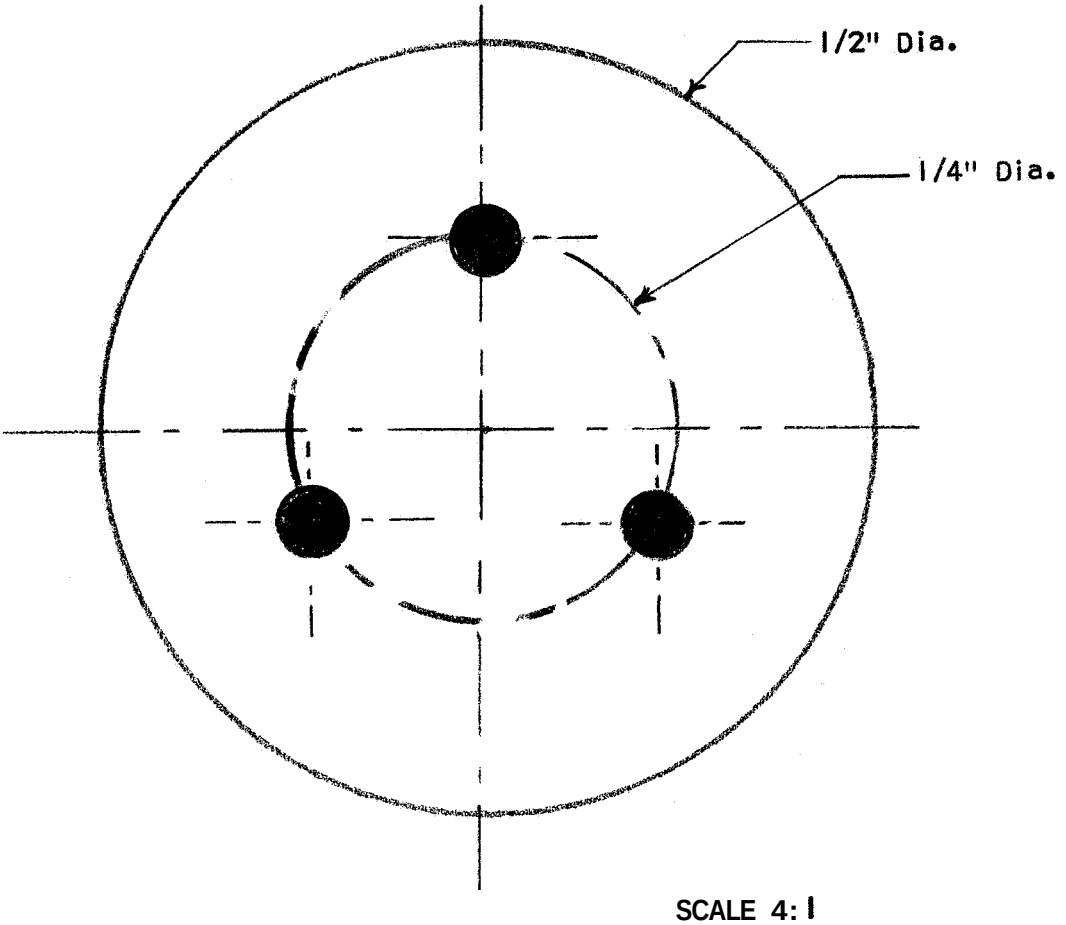

Figure 6-9. Location of Wires in Tensile Specimen

SECTION 7
MECHANICAL PROPERTIES OF PRESTRESSED SPECIMENS

Tensile and flexural properties were determined for the prestressed zirconia matrix. The planned flexural tests of prestressed alumina were not conducted because of excessive cracking of the specimens during the cure cycle. Variation in the cure cycle did not alleviate this condition. Although the cause of the difficulties was not resolved, it is believed that uneven curing due to conversion of the orthophosphoric acid to the pyrophosphoric acid, with the required evolution of water of reaction, was the primary cause.

To establish how valid and adequate is the theory for predicting the strength of prestressed ceramics and to evaluate the efficiency of these materials as well as the increases in strength of prestressed ceramics over unreinforced, unprestressed ceramics, a comparison has been made between the theoretical and experimental results, The strengths of both the tensile as well as flexural specimens were investigated. Although most of the tensile specimens failed as was expected, some unexpected results were, however, obtained while testing the flexural specimens. Perhaps the most important of these was that the ultimate failure of the flexural specimens was in compression.

7.1 TENSILE TESTING PROCEDURE

Tensile tests were conducted on prestressed zirconia at room and elevated temperature with four load levels and two variations in the amount of reinforcement. Load levels were nominally 125, 300, 450 and 1,100 lbs/cable. Reinforcement levels were 3.63 and 8.47 percent by volume.

The tensile tests at room temperature utilized resistance strain gages to measure strain.

Strain measurements for the elevated temperature tensile tests on the composite systems were obtained with the Optron Model 680 optical extensometer.

The stress and strain values at which the matrix cracked were not clearly defined with the optron, however, in most cases, it was discernible.

The furnace used for heating the composite tensile specimens is the same as used for the matrix and is described in Section 5.3. The temperature was monitored by attaching chromel-alumel thermocouples to the specimen with a ceramic cement. The alignment of the tensile test specimens was controlled by using the test fixture described for the matrix in Section 5.3

Since the porosity has a pronounced effect on the strength of the matrix, the relative porosity of the specimens was noted. Three levels of porosity were indicated by examination of the specimens: low, medium, and high. A photograph showing variations is presented in Figure 7-1. Low porosity is shown in Figure 7-1a, medium porosity, in Figure 7-1b, and high porosity is shown in Figure 7-1c.

A resume of the tensile properties obtained for the tests of zirconia composites is presented in Table 7-1 showing the reinforcement preload, the failure mode, and the porosity of each specimen. The failure mode is presented in Figure 7-2, which shows four types of failure as follows: (1) the matrix failure and reinforcement failure at the end of the metal shoulder, (2) the matrix failure at the end of the metal shoulder with the reinforcement pulled out of the matrix, (3) failure of the matrix and reinforcement in the gage length, and (4) failure of the matrix and reinforcement with complete destruction of the matrix.

Several specimens exhibited spalling or flaking during heating prior to application of the test load. In extreme cases, the spallation resulted in destruction of the specimen shoulder. Examples of the flaking are shown in Figure 7-3.

7.2 FLEXURAL TESTING PROCEDURES

Flexural tests were conducted on prestressed zirconia at room and elevated temperature for four prestress load levels with two variations in the amount of reinforcement. Load levels were the same as those used in the tensile tests. Reinforcement volume fractions were 3.4 and 8.0 percent.

Figure 7-1. Variations in Porosity of Tensile Specimens; (a) Low, (b) Medium, (c) High

Table -1

TENSILE PROPERTIES OF PRESTRESSED ZIRCONIA

Nominal Temp. (°F)	Cable Size	Nominal Pre-Load (lb/cable)	Specimen Number	Load at Failure (lbs)	Area (in^2)	Stress at Failure[7] (psi)	E (psi x 10^{-6})	Porosity[1]	Failure Location[2][7]	Remarks
[illegible]	7 × 3	116	ZT3-5	500	0.1971	2,500	---	M	T	
		294	ZT3-14	2240	0.1987	11,270	9.1	H	B	
		413	ZT3-19	2240	0.1987	11,270	13.1	L	B	
		413	ZT3-21	2240	0.1979	11,340	13.3	L	B	
	7 × 7	269	ZT-2	4200	0.1979	21,220	14.9	L	B	
		308	ZT-4	2980	0.1971	15,200	16.7	M	T	Crack
		308	ZT-5	3200	0.1971	16,300	12.8	M	T	Crack
		308	ZT-6	2110	0.1971	10,800	15.0	M	B	Crack
		908	ZT-14	5250	0.1971	26,640	13.7	M	B	
		908	ZT-15	5320	0.1964	27,100	11.8	M	T	All ceramic broke off
		1160	ZT-19	5120	0.1948	26,280	14.8	L	B	
1000	7 × 3	116	ZT3-4	645	0.1971	3,270	(3)	H	T	Crack
		123	ZT3-10	1655	0.1948	8,450	(3)	M	C	
		123	ZT3-11	1685	0.1979	8,600	(3)	H	C	
		294	ZT3-15	1720	0.1956	8,790	16.0	M	C	
		502	ZT3-16	1785	0.1956	9,130	(3)	L	C	
		502	ZT3-17	1930	0.1948	9,910	5.6	L	C	
	7 × 7	269	ZT-1	2170	0.1956	11,090	8.1	M	B	
		269	ZT-3	2635	0.1971	13,370	(3)	M	B	3 Cycles
		298	ZT-9	1290	0.1964	6,560	(3)	L	T	
		1040	ZT-16	3590	0.1979	18,300	(3)	M	T	Crack,Hole
		1040	ZT-17	1965	0.1956	10,050	12.5	M	T	Crack
1[illegible]0	7 × 3	128	ZT3-2	1080	0.1987	5,500	1.92	M	C	LF (6)
		128	ZT3-3	1075	0.1979	5,490	1.92	M	C	LF (6)
		123	ZT3-12	1140	0.1971	5,810	1.66	M	C	
		294	ZT3-13	1175	0.1956	6,010	0.77	M	C	
		502	ZT3-18	1225	0.1956	6,260	2.90	L	C	
		413	ZT3-20	1185	0.1987	5,960	1.20	M	C	
	7 × 7	298	ZT-7	1230	0.1987	6,280	(3)	L	T	
		307	ZT-10	2520	0.1956	12,900	5.95	L	C	
		307	ZT-12	2645	0.1971	13,500	14.50	M	C	Heated Twice
		908	ZT-13	2665	0.1979	13,470	(3)	H	C	
		1160	ZT-20	2680	0.1971	13,600	2.0	M	C	
		1160	ZT-21	3110	0.1964	15,840	3.1	L	C	
20[illegible]	7 x 3	417	ZT3-25	630	0.1964	3,210	3.6	M	C	HF (6)
		417	ZT3-26	695	0.1956	3,550	1.8	M	C	MF (6)
		417	ZT3-27	705	0.1987	3,600	1.16	M	C	MF (6)
25[illegible]	7 × 3	370	ZT3-22	520	0.1956	2,250	(4)	L	C	HF (6)
		370	ZT3-23	441	0.1979	2,350	(4)	L	C	HF (6)
		370	ZT3-24	461	0.1979	2,650	(4)	L	C	HF (6)
		128 (5)	ZT3-1[5]	655	0.1956	3,340	(4)	M	C	LF (6)
		116	ZT3-7	467	0.1971	2,380	(4)	M	C	Crack
		116	ZT3-8	450	0.1964	2,300	(4)	M	T	Crack
	7 × 7	307	ZT-11	775	0.1971	3,960		M	C	Heated 3 Times

NOTES:
(1) L = Low, M = Medium, H = High
(2) T = Top, C = Center, B = Bottom
(3) Autographic recordings poor, data not determined
(4) Ultimate strength only no strain recorded
(5) This specimen tested at 2100°F (1149°C)
(6) LF = Low Flaking, MF = Medium Flaking, HF = High Flaking
7 See Table 7-3 for more detailed definitions of failure

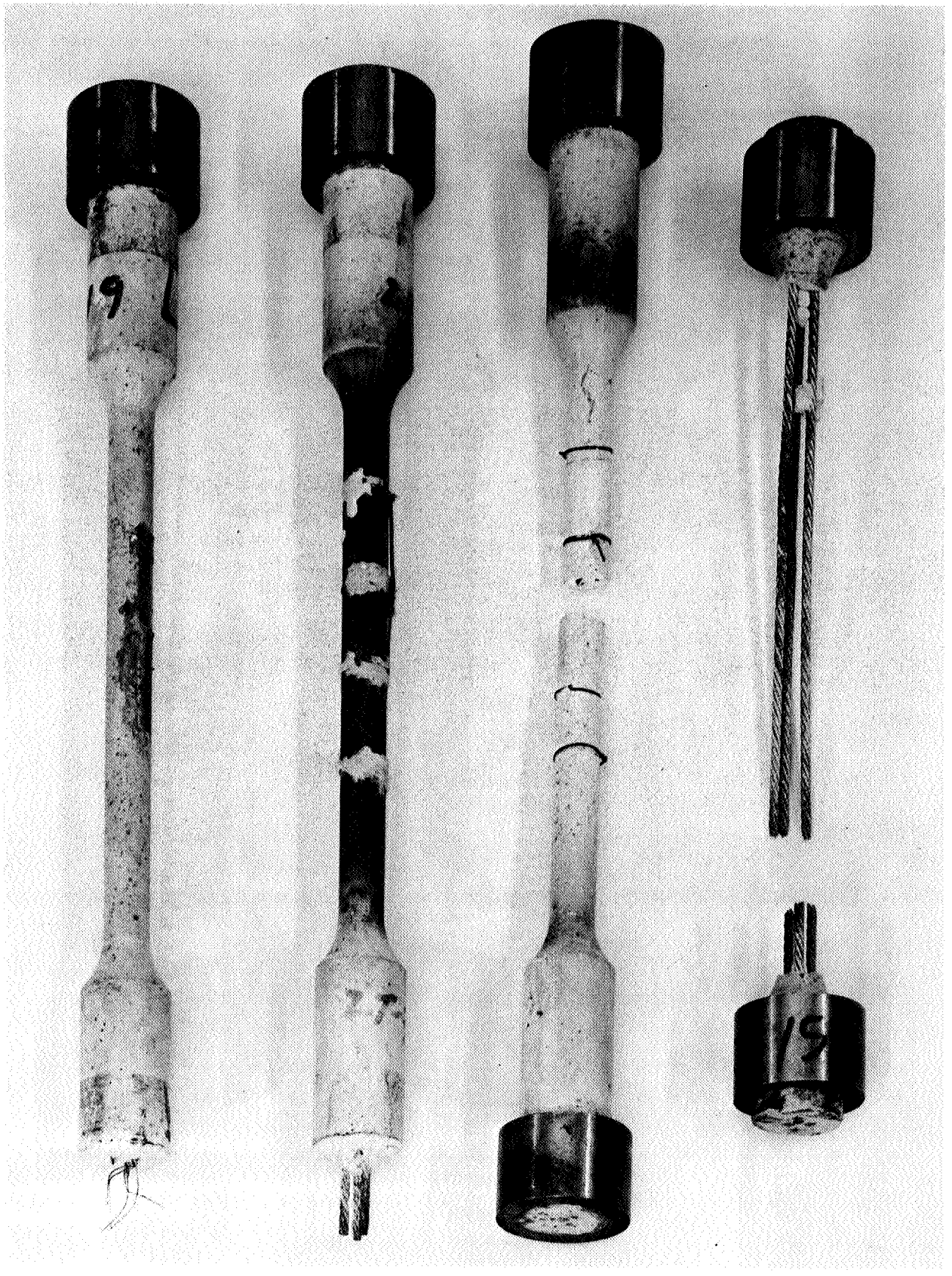

Figure 7-2. Failure Modes of Prestressed Tensile Specimens

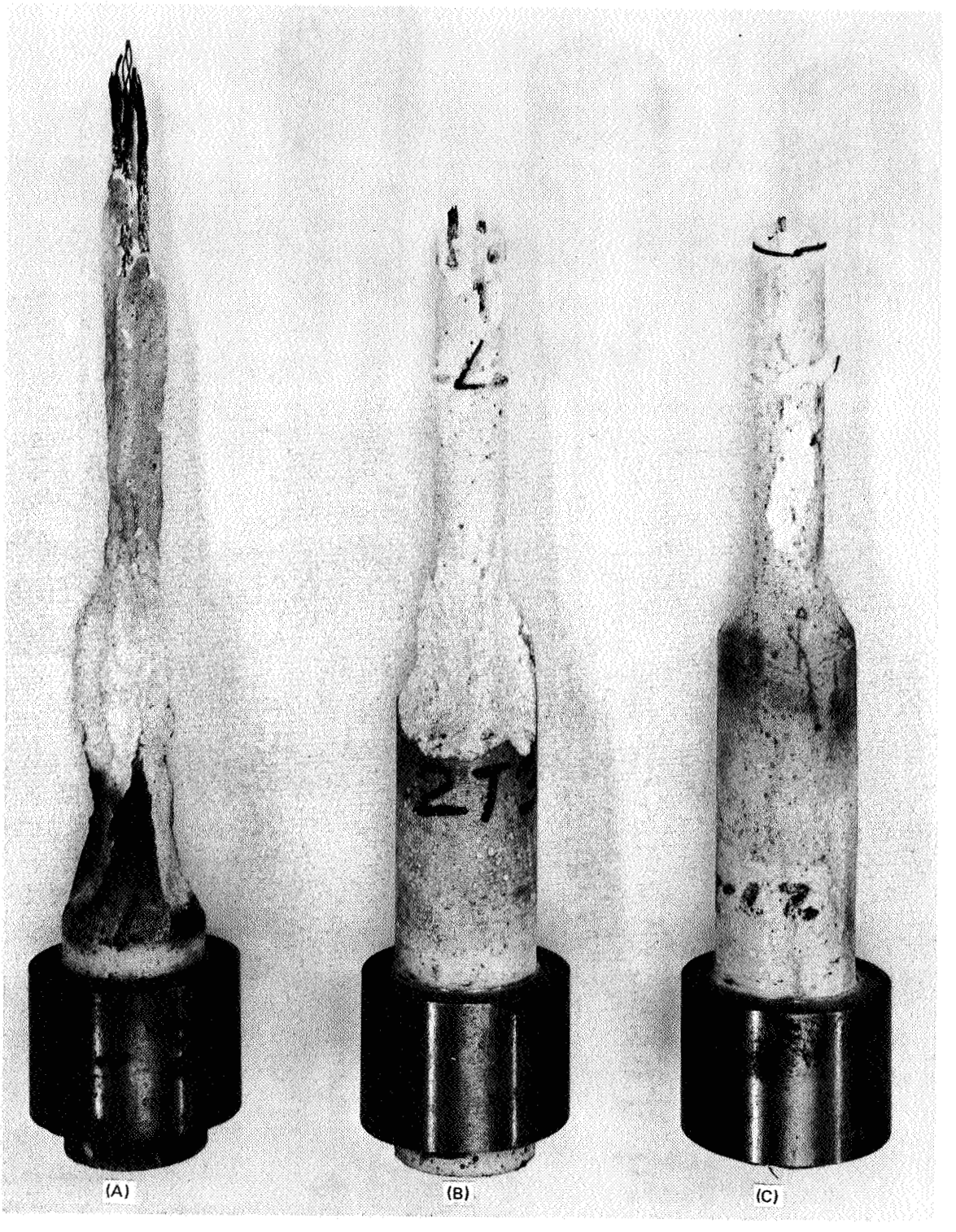

Figure 7-3. Degree of Flaking; (a) High, (b) Medium, (c) Low

Two types of instrumentation were used to measure strains of the room temperature flexural specimens containing highly prestressed 7x3 and 7 x 7 cables. The bottom or tensile side of the flexural specimens had strain gages cemented under the point of applied load. Simultaneously, an Optron tracking scope was used to monitor the deflection. The two types of instrumentation were used to cross check the results. As may be seen upon examination of Table 7-2, the moduli were very different. The elevated temperature flexural tests were conducted using the Optron Model 680 optical extensometer. The furnace used for heating the elevated temperature flexural specimens during testing is described in Section 5. 2. The temperature was monitored with a micro-optical pyrometer.

In general, two distinct failure modes were observed while testing prestressed flexural specimens. In most of the specimens, the initial failure was cracking of the ceramic under the point of the application of load where the maximum tensile stress occurred. (Figure 7-4a, top.) This was followed by compressive failure of the ceramic at the top surface. (Figure 7-4a, bottom.) The ultimate flexural strength (the flexural stress at which compressive failure occurred), was generally much higher than the cracking stress (the stress at which initial cracking of the ceramic was observed). Six specimens were found to have what appear to be cracks in the periphery of the plane which contained the reinforcement; these specimens failed in interlaminar shear through the plane containing the reinforcement as shown in Figure 7-4b. For some highly prestressed specimens with abnormally high porosity, it appeared that the initial failure was by compression of the top surface which was then followed by tensile failure at the bottom surface. Finally, some of the specimens which were tested at elevated temperatures failed by excessive deformations. Figure 7-4c depicts a specimen which failed by excessive deformation, i. e., it deflected to the bottom of the fixture without apparent ceramic or reinforcement failure. It should be noted that in some cases as shown in Figure 7-4c, the side of the specimen exposed to maximum tensile stress during the test exhibited many cracks after the

Table 7-2

FLEXURAL PROPERTIES OF ZrO_2 COMPOSITE

Temp. (°F)	Cable	Nominal Pre-Load (lbs/cable)	Specimen Number	Ultimate Stress at Failure (psi)	Distance of Wire From Bottom (in)	Flexural Modulus (psi x 10^{-6}) Strain Gage	Optron	Failure Location[1][2] and Remarks
70	7 × 3	116	Z3-1	18,400	0.141		16.8	C-
			Z3-2	17,600	0.125		11.0	C
			Z3-3	22,600	0.109		16.8	C
		474	Z3-16	37,400	0.100	7	5.2	1/2" off Center
			Z3-17	11,300	0.083	5	2.6	C
			Z3-18	11,500	0.110	6	3.7	C-Shear
	7 × 7	292	Z-1	26,500	0.125		14.3	C
			Z-2	30,000	0.109		14.3	C
			Z-3	25,500	0.141		15.4	C
		1042	Z-16	27,400	0.110	9.1	4.0	C
			Z-17	20,000	0.110	11.8	4.6	C
			Z-18	22,900	0.110	9.5	4.3	C
500	7 x 3	474	Z3-10	35,730	0.060		5.6	C-Shear
			Z3-11	27,500	0.120		9.1	1/2" C-Shear
			Z3-12	29,700	0.110		8.9	C-Shear
	7 × 7	1042	Z-10	23,600	0.130		4.1	1/4" off Center
			Z-11	28,300	0.130		4.6	1/2" off Center
			Z-12	26,800	0.130		4.8	1/4" off Center
1000	7 x 3	116	Z3-4	18,200	0.100		10.6	C
			Z3-5	19,200	0.130		5.7	C
			Z3-6	26,000	0.120		10.0	C
	7 × 7	292	Z-4	25,033	0.156		10.0	(800°F) C
			Z-5	40,500	0.094		7.7	Support Failure
			Z-6	31,500	0.125		6.8	C
1500	7 × 3	116	Z3-7	1,600	0.130		--	No Failure
			Z3-8	12,600	0.140		3.7	(1330°F) Center
			Z3-9	1,200	0.160		--	No Failure
		474	Z3-13	17,300	0.100		2.8	C-Shear
			Z3-14	11,600	0.110		3.6	C-Shear
			Z3-15	24,600	0.110		5.2	C-Shear
	7 × 7	292	Z-7	1,900	0.080		---	No Failure
			Z-8	2,070	0.120		---	No Failure
			Z-9	2,180	0.130		---	No Failure
		1042	Z-13	11,400	0.130		1.4	1/4" off Center
			Z-14	8,700	0.110		1.3	1/4" off Center
			Z-15	13,450	0.130		1.4	1/4" off Center

NOTES: (1) Specimens failed in tension initially and in compression ultimately unless otherwise designated
(2) C = Center

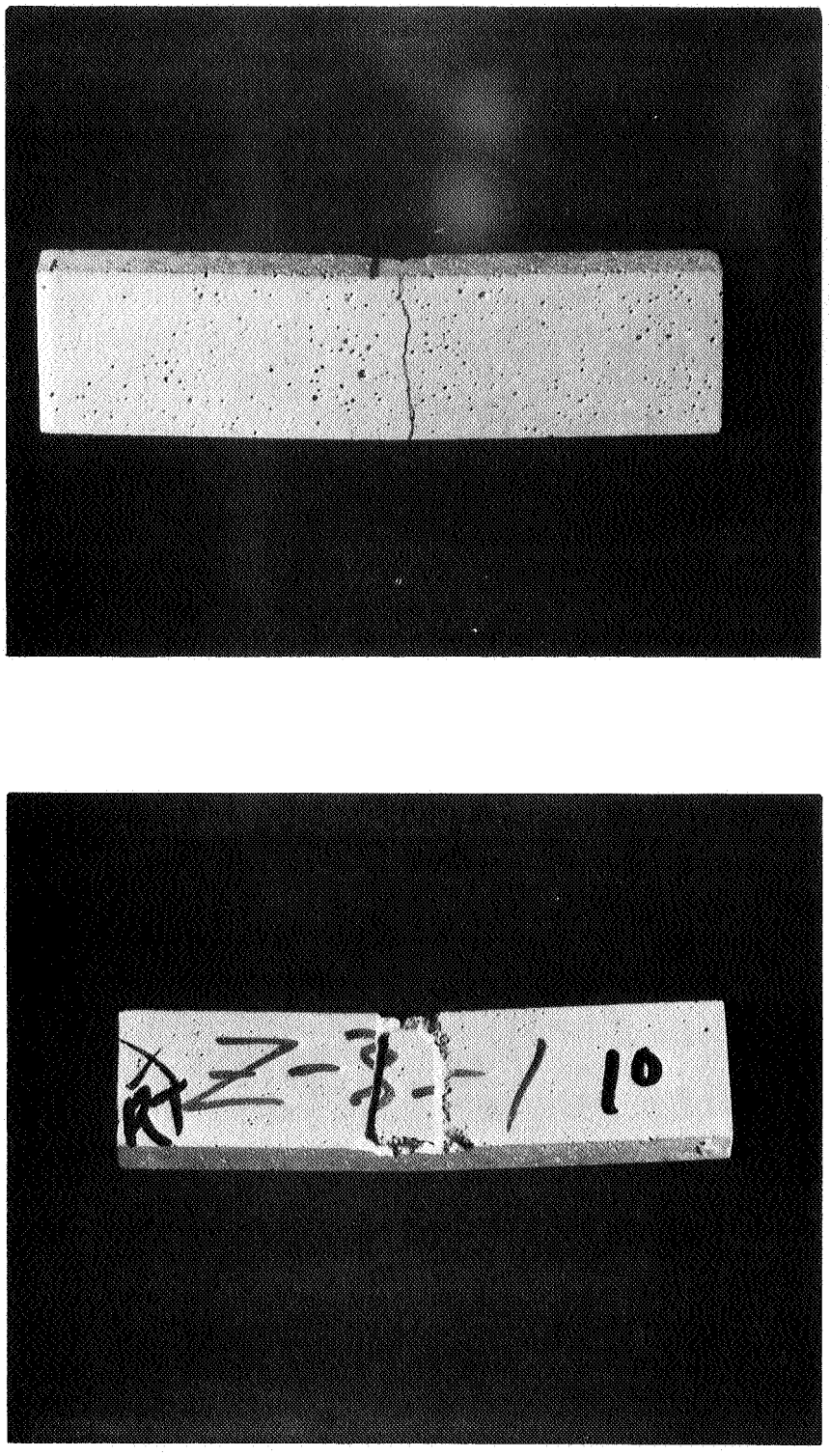

Figure 7-4a. Typical Initial Tensile Crack and Ultimate Compressive Failure of a Prestressed Zirconia Flexural Specimen (3/4x)

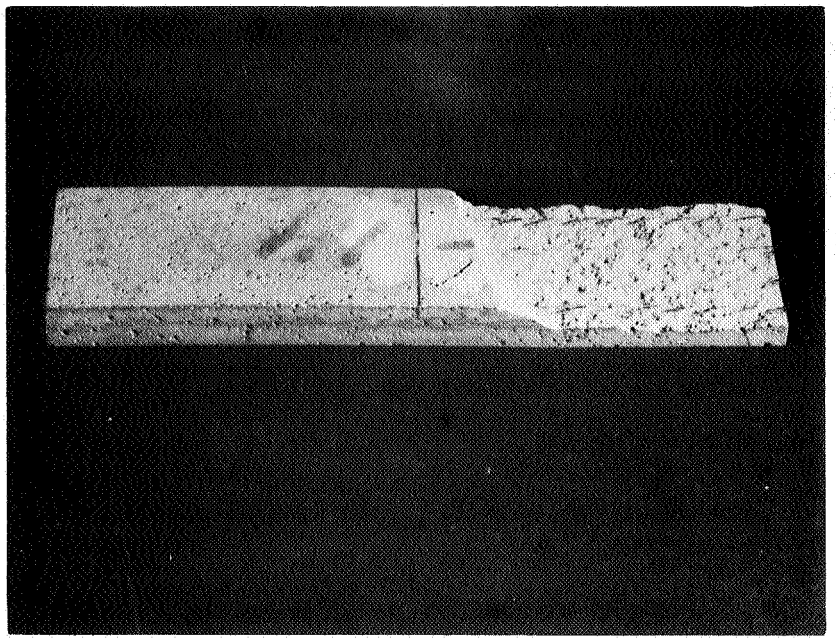

Figure 7-4b. Interlaminar Shear Failure of Prestressed Flexural Specimen

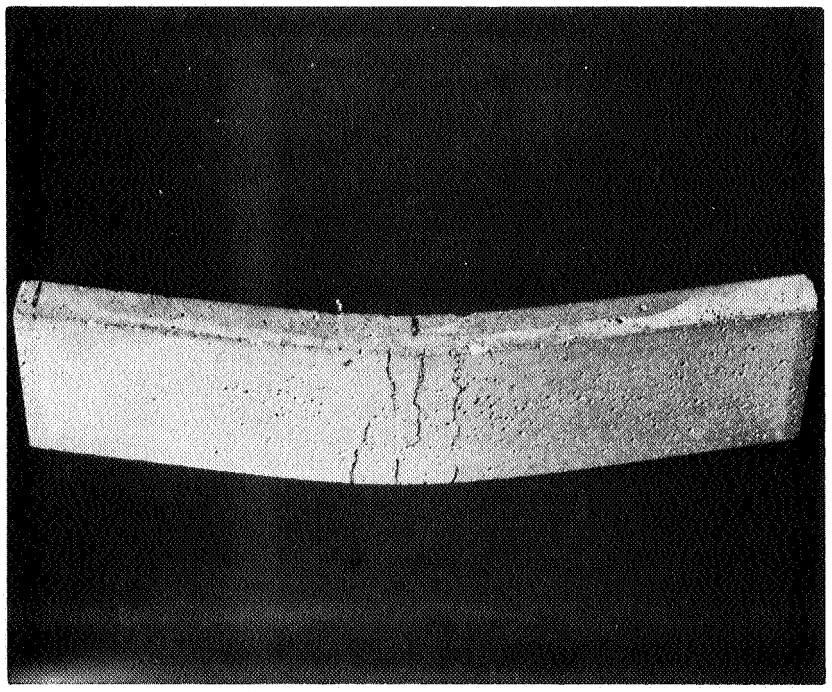

Figure 7-4c. Failure by Excessive Deformation of Prestressed Flexural Specimen (3/4x)

test was completed. Although it was obvious that cracking did occur, it was not discernible from the autographic recordings. In none of the specimens that were tested was there any evidence of the failure of the reinforcement either by pullout or tensile failure. The flexural test data obtained for the prestressed zirconia composites are presented in Table 7-2.

7.3 EVALUATION OF TENSION TEST DATA

A comparison of experimental and theoretical results on the tensile strength of prestressed zirconia is shown in Table 7-3. The theoretical cracking stress, that is the composite stress at which the ceramic fails, was computed from Equation 3. 2-4 using the experimentally obtained properties of constituents given in Tables 5-4, 5-5 and 5-7. The theoretical results are based on a consolidation temperature of 600°F (316°C) and prestress levels shown in Table 7-3. As loads cannot be carried by the ceramic after cracking, the ultimate strength of the composite was based on the load carried by the reinforcement.

Despite the scatter in properties of zirconia, significant variations in prestress level within any given specimen, and difficulties in measuring the exact loads at which ceramic cracking occurred, the agreement between the theoretical and experimental composite stress which initiated cracking in the ceramic is quite good. Even at high temperatures, the approximate theory appears to predict the cracking stresses to a reasonable degree of accuracy. At temperature of 2, 000°F (1, 093°C) and above, no cracking in the ceramic was apparent. At and above that temperature, the composite cracking stress and the ultimate stress coincided. It is interesting to note that the experimental ultimate tensile strengths are higher than the strengths calculated from the data given in Tables 5-4 and 5-5. This coincides with the findings discussed in Section 5. **3.** It appears that the restraint against untwisting, which is imposed by the ceramic on the reinforcement, is the cause for the increase in tensile strength of the reinforcement.

Due to the variation in applied prestress and porosity, it is difficult to present the data given in Table 7-3 in a more compact form. It is apparent

Table 7-3

TENSILE STRENGTH OF PRESTRESSED, TUNGSTEN-REINFORCED ZIRCONIA (EXPERIMENT AND THEORY)

(1) Specimen Designation	Test Temperature (°F)	(2) Applied Reinforcement Prestress (σ_{wi}) (psi)	(3) Variation In σ_{wi} (±%)	(4) (5) Composite Cracking Stress (psi) Experiment	Theory	(5) (6) Ultimate Tensile Strength of Composite (psi) Experiment	Theory	Failure Type and Location	Po o ty	
ZT3-14	70°	124, 000	20	6, 300	8, 167	*11, 270	10, 700	End; 87% of wires broken, rest pulled out	High	3380
ZT3-19	70°	174, 000	--	7, 850	9, 949	*11, 270	10, 700	End; 92% of wires broken; rest pulled out	Low	3380
ZT3-21	70°	174, 000	--	8, 880	9, 966	*11, 340	10, 700	End; parts of 3 cables broken	Low	3380
ZT-2	70°	48, 500	18	8, 600	8, 018	(21, 220)	24, 600	End and pullout of 2 cables; one broke	Low	3380
ZT-4	70°	55, 700	--	6, 500	8, 628	(15, 200)	24, 600	End and pullout of 2 cables; one broke	Medium	3380
ZT-5	70°	55, 700	--	9, 100	8, 628	(16, 300)	24, 600	End and pullout of 2 cables; one broke	Medium(a)	3380
ZT-6	70°	55, 700	--	7, 100	8, 628	(10, 800)	24, 600	Shoulder and pullout of 3 cables	Medium(b)	3380
ZT-14	70°	164, 000	6	13, 950	17, 760	*26, 640	24, 600	End; parts of 3 cables broken	Medium	3380
ZT-15	70°	164, 000	6	10, 180	17, 890	27, 100	24, 600	Near Shoulder	Low	3380
ZT-19	70°	210, 000	14	13, 000	21, 510	26, 280	24, 600	End; 2 cables broke; one pulled out	Low	3380
ZT3-10	1000°	52, 100	6	5, 300	4, 966	8, 450	6, 760	Center	High	1730
ZT3-11	1000°	52, 100	6	6, 500	4, 966	8, 600	6, 760	Center	Medium	1730
ZT3-15	1000°	124, 000	20	---	7, 603	8, 790	6, 760	Center	High	1730
ZT3-16	1000°	212, 000	--	9, 130	10, 800	9, 130	6, 760	Center	Low	1730
ZT3-17	1000°	212, 000	--	9, 050	10, 850	9, 910	6, 760	Center	Low	1730
ZT-1	1000°	48, 500	18	7, 700	8, 535	(11, 090)	15, 300	End; Pullout of 3 c es	Medium	1730
ZT-3	1000°	48, 500	18	---	8, 472	(13, 370)	15, 300	End and pullout of 3 cables	High	1730
ZT-16	1000°	188, 000	14	13, 900	20, 160	(18, 300)	15, 300	End and pullout of 2 cables ne broke	Medium(c)	1730
ZT3-2	1500°	54, 000	--	5, 280	5, 457	5, 500	4, 910	Center; low flaking	Medium	168
ZT3-3	1500°	54, 000	--	4, 060	5, 457	5, 490	4, 910	Center; low flaking	Medium(d)	168
ZT3-12	1500°	52, 100	6	5, 310	5, 380	5, 810	4, 910	Center	High	168
ZT3-13	1500°	124, 000	20	5, 480	8, 017	6, 010	4, 910	Center	Medium(e)	168
ZT3-18	1500°	212, 000	--	5, 900	11, 210	6, 260	4, 910	Center	Medium	168
ZT3-20	1500°	174, 000	--	---	9, 676	5, 960	4, 910	Cooter	Low	168
ZT-7	1500°	54, 000	--	3, 020	11, 040	(6, 280)	10, 900	E an pullout of 3 cables	Low	168
ZT-10	1500°	55, 500	--	8, 700	11, 150	12, 900	10, 900	Cooter	Low	168
ZT-12	1500°	55, 500	--	10, 080	11, 150	13, 500	10, 900	Cooter	Low(d)	168
ZT-13	1500°	164, 000	6	---	20, 770	13, 470	10, 900	Center	High(e)	168
ZT-20	1500°	210, 000	--	12, 000	24, 200	13, 600	10, 900	Center	Low	168
ZT-21	1500°	210, 000	--	6, 300	24, 420	15, 840	10, 900	Center	Medium	168
ZT3-25	2000°	176, 000	--	Composite cracking stress is equal to composite ultimate stress		3, 210	3, 280	Center; high flaking	Medium	---
ZT3-26	2000°	176, 000	--			3, 550	3, 280	Center; medium flaking	Medium(f)	---
ZT3-27	2000°	176, 000	--			3, 600	3, 280	Center; medium flaking	Medium	---
ZT3-1	2100°	54, 000	--			3, 340	2, 910	Center; low flaking	Medium	---
ZT3-7	2500°	45, 400	11			2, 380	1, 890	Center	Medium(g, h)	---
ZT3-8	2500°	45, 400	11			2, 300	1, 890	Center	High(g, h)	---
ZT3-22	2500°	156, 000	9			2, 250	1, 890	Center; high flaking	Low(g)	---
ZT3-23	2500°	156, 000	9			2, 350	1, 890	Center; high flaking	Low(g)	---
ZT3-24	2500°	156, 000	9			2, 650	1, 890	Center; high flaking	Low(g)	---
ZT-11	2500°	55, 500	--			3, 960	4, 070	Center	Medium(g)	---

NOTES:
(1) Specimens denoted ZT3-X contained 3.63% reinforcement by volume; those denoted ZT-X contained 8.47% reinforcement.
(2) σ_{wi} is the mechanically applied prestress.
(3) This column represents the variation in prestress from cable to cable in any given specimen. If no number is given, the variation was less than 5%.
(4) This is the composite tensile stress (load/area) at which ceramic cracks.
(5) At 2000°F and above, the cracking and ultimate composite stresses were equal.
(6) The numbers with asterisks indicate that the failure stress is near ultimate; numbers in parentheses denote failure by pullout of the reinforcement; only the numbers without parentheses or asterisks in front of them denote ultimate strength.

(a) Specimen contained 1/2" to 1" cracks
(b) Specimen cracked near shoulder
(c) Specimen contained cracks and holes
(d) Specimen heated 2 times
(e) Specimen contained cracks near surface
(f) Specimen contained 4" crack
(g) Specimen heated in air; all other heated in argon atmosphere
(h) Specimen contained cracks
(i) Specimen heated 3 times

from the results presented that prestressing is an efficient means of increasing the tensile load-carrying ability of ceramics.

At room temperature, the highest increase in load carrying ability of the ceramic due to prestress was by a factor of 4; at 1,000°F (538°C) this figure was 8; at 1,500°F (816°C) the figure was 71. The numbers quoted are based on stresses required to initiate cracking in the ceramic. The increases in ultimate strength were by factors even higher than those given above.

The experimental results, given in Table 7-3, also confirm the theoretical results shown in Figure 6-2 regarding the relationship between prestress, temperature, and composite tensile strength.

7.4 EVALUATION OF FLEXURE TEST

In conducting the theoretical analysis on the prediction of the strength of prestressed flexural specimens, two failure modes in each specimen were considered: (1) initial cracking of the ceramic on the tensile side (bottom side), followed by (2) compressive failure on the top side.

To predict the load which would initiate tensile failure in the flexure specimen, the prestress in the ceramic was determined as a function of the thermal and elastic properties of the constituents, location of the reinforcement, consolidation temperature, and the mechanical prestress. An expression similar to Equation 3.1-7 was obtained. This equation differed from Equation 3.1-7 only in the case when the reinforcement did not lie at the centroid of the specimen. The new equation allowed for determination of the nonuniform prestress distribution which occurs as a result of the reinforcement eccentricity. Using orthotropic beam theory, stresses due to an externally applied loading were then computed at any point in the specimen. An approach similar to that described in Section 3.2 was then used.

To obtain the ultimate flexural strength, that is the load which causes compressive failure in the beam, a somewhat different approach was employed. Rather than obtaining one value for the ultimate strength, two values were

calculated - the upper and the lower bounds. This was done since it could not be readily established how far the crack propagated due to the initial tensile failure at the bottom side of the beam. (It is noted here that the ultimate failure in compression took place after cracking occurred on the tension side.) To arrive at the upper bound, a load required to cause compressive failure of the beam was calculated assuming that the beam was uncracked. The lower bound was calculated assuming that the crack extended from the bottom of the beam to the plane of the reinforcement. An analysis similar to that used for predicting cracking stress was used to determine the upper bound. When computing the lower bound, however, the reduction in stiffness of the beam due to cracks was taken into account.

A comparison of experimental and theoretical results for the strength of prestressed flexural specimens at room and elevated temperatures is shown in Table 7-4. The experimental results shown are only for specimens of which the quality was similar to unreinforced, unprestressed flexural specimens which were tested to obtain the basic material properties. The theoretical results shown in Table 7-4 were based on properties of constituents given in Tables 5-3, 5-4, 5-8 and 5-10. The use of tensile properties of zirconia rather than flexural properties did not produce any significant differences in the theoretical results. Using the tensile properties of zirconia in the analysis, the theoretical cracking stress remained almost the same as shown in Table 7-4. The values for the two bounds were, however, decreased.

Since the data on the variation of compressive strength of the chemically consolidated zirconia with temperature were not available and such information was needed to predict the ultimate strengths, it was assumed that the variation of compressive strength with temperature was similar to the variation in flexural strength.

7.5 STRENGTH TO DENSITY RATIOS

The strength-to-density ratios of the zirconia matrix and the prestressed composites were determined for the average values of the flexural and tensile strength are shown in Tables 7-5 and 7-6. The data shows the

Table 7-4

FLEXURAL STRENGTH OF TUNGSTEN-REINFORCED, PRESTRESSED ZIRCONIA (TEST VS THEORY)

(1) Specimen Designation	Test Temp. (°F)	(2) Applied Reinforcement Prestress (σ_{wi}) (psi)	(3) Variation in σ_{wi} (±%)	(4) Cracking Load (lbs)		(5) Ultimate Load (lbs)			(6) Stress in Ceramic at Cracking (Experiment) (psi)	(7) Ultimate Composite Strength (Experiment) (psi)	Comments		Flexural Strength of Unreinforced, Unprestressed Zirconia (psi)
							Theory						
				Experiment	Theory	Experiment	Upper Bound	Lower Bound			General	Failure Type	
Z-1	70	52,500	6	99	96	310	380	212	7,980	26,500		b	H000
Z-2	70	52,500	6	117	115	345	391	254	9,100	30,000		b	H000
Z-3	70	52,500	6	94	79	284	375	177	7,610	25,500		b	H000
Z3-1	70	48,200	10	76	58	212	379	129	6,570	18,400		b	H000
Z3-2	70	48,200	10	75	65	205	380	161	6,430	17,600		b	H000
Z3-3	70	48,200	10	52	73	258	384	197	4,340	22,600		b	H000
Z3-16	70	199,000	6	215	234	544	483	295	13,880	37,400	a	b	H000
Z3-18	70	199,000	6	157	211	168	462	256	10,33Z	11,500	a	c	H000
Z3-10	500	199,000	6	220	329	532	607	501	13,400	35,7E0	a	c	H250
Z3-11	500	199,000	6	192	191	392	471	230	12,910	27,500	a	c	H250
Z3-12	500	199,000	6	242	213	429	491	267	16,080	29,700	a	c	H250
Z-5	800	52,500	6	123	149	467	430	311	9,630	40,500			H320
Z-4	1000	52,500	6	82	69	290	333	125	6,800	25,000		b	H130
Z-6	1000	52,500	6	102	118	358	361	194	8,390	31,500		b	H130
Z3-4	1000	48,200	10	60	97	210	397	222	5,060	18,200		b	H130
Z3-5	1000	48,200	10	80	76	225	387	153	6,750	19,200		b	H130
Z3-6	1000	48,200	10	81	81	300	384	170	6,960	26,000		b	H130

NOTES:

(1) Specimens designated Z3-X contained 3.4% reinforcement by volume; those designated Z-X contained 8.0% reinforcement.
(2) This is the mechanically applied average prestress.
(3) This column shows the variation in prestress from cable to cable in any given specimen.
(4) This column gives the load required to cause ceramic cracking due to tensile stress, when a flexure specimen is subjected to a 3-point loading.
(5) This column represents the load required to produce a compressive failure in the ceramic, after ceramic cracking has taken place.
(6) This is the true stress in the ceramic when cracking occurs. It is based on experimental value of the cracking load.
(7) This is the experimental c mpos ie st e33 in the Oe m, when the l tter i s bj.ct A to lim <e lo Ω

(a) Specimens contained cracks in the periphery of a plane which contained the wires.
(b) Initial failure was cracking on the bottom surface (tension side) of the beam; secondary failure was by compression on the top surface.
(c) Specimens failed by cracking and interlaminai shear through the plane containing reinforcement.

Table 7-5

FLEXURAL STRENGTH TO DENSITY RATIOS FOR ZIRCONIA MATRIX AND COMPOSITES

Temp. (°F)	Average Matrix(1) Strength (psi)	Matrix Strength to Density Ratio (in)	Prestressed Data: 3.4% Tungsten Wire (2) — Prestress = 52.8 KSI/Cable: Average Ultimate Strength (psi)	Strength to Density (in)	Prestress = 190 KSI/Cable: Average Ultimate Strength (psi)	Strength to Density (in)	8% Tungsten Wire (3) — Prestress = 54 KSI/Cable: Average Ultimate Strength (psi)	Strength to Density (in)	Prestress = 199 KSI/Cable: Average Ultimate Strength (psi)	Strength to Density (in)
70	4,000	29,000	19,576	128,000	20,100	131,500	26,860	148,000	23,430	134,000
1000	4,250	32,000	21,236	138,500	----	----	28,268	161,000	----	----
1500	1,200	8,700	5,152	33,700	17,800	116,200	2,053	11,300	11,200	61,500
2000	165	1,200	----	----	----	----	----	----	----	----

Table 7-6

TENSILE STRENGTH TO DENSITY RATIOS FOR ZIRCONIA MATRIX AND COMPOSITES

	Average Matrix(1) Strength (psi)	Matrix Strength to Density Ratio (in)	Prestressed Data: 3.63% Tungsten Wire (4) — Prestress = 52.8 KSI/Cable: Average Ultimate Strength (psi)	Strength to Density (in)	Prestress = 190 KSI/Cable: Average Ultimate Strength (psi)	Strength to Density (in)	8.47% Tungsten Wire (5) — Prestress = 54 KSI/Cable: Average Ultimate Strength (psi)	Strength to Density (in)	Prestress = 199 KSI/Cable: Average Ultimate Strength (psi)	Strength to Density (in)
70	3,380	24,600	---	---	11,290	71,400	17,400	94,500	26,690	145,000
100	1,730	12,600	6,760	42,800	9,274	58,600	10,340	56,100	14,125	76,900
150	168	1,220	5,543	35,000	6,187	39,000	10,833	58,700	14,304	77,500
200	---	---	---	---	3,440	21,800	---	---	---	---
250	---	---	2,670	900	2,393	15,100	---	---	---	---

(1) Matrix Density $\cong$ .137 lbs/in^3

(2) 3.4% Wire Composite Density = .153 lbs/in^3

(3) 8% Wire Composite Density = .182 lbs/in^3

(4) 3.6% Wire Composite Density = .158 lbs/in^3

(5) 8.47% Wire Composite Density = .184 lbs/in^3

comparison at various temperatures of volume fractions of reinforcement and various stress levels, The densities used in computing the strength to density ratio for the ceramic was the apparent bulk density of 3.81 gms/cm^3. The composite density was based on the theoretical density of tungsten and the measured bulk density value of the matrix.

SECTION 8
SUMMARY AND CONCLUSIONS

The feasibility of prestressing chemically consolidated ceramic has been demonstrated. The tensile strength of zirconia matrix, the average value of which was ~3, 000 psi at 70°F (21°C), was increased up to nominal 14, 000 psi by prestressing the matrix with tungsten cable subjected to 160, 000-psi prestress. At temperatures of 1, 500°F (816°C), tensile strength was increased from ~200 psi to as high as 12, 000 psi for a prestressed composite. The inability of the chemically consolidated zirconia to survive at temperatures above 2, 000°F (1, 093°C) may be attributed to the possible instability of the cubic phase in the calcia stabilized system in the presence of the phosphate radical. Conversions of the cubic to the monoclinic phase evidently reduces the strength. The variation in strength of the matrix cannot be attributed wholly to the crystalline inversion but was also influenced by the mode of testing, variations in porosity, and probable variations in the degree of stabilization.

Despite the great number of variables which influence the flexural strength, significant variations in prestress in any given specimen, and variations in material properties of constituents, the correlation between experimental and theoretical results is quite good. The theoretical cracking loads show good agreement with experimental results. Moreover, most of the ultimate loads fall within the theoretically predicted bounds,

The level of sophistication employed in the analysis of the strength of chemically consolidated zirconia prestressed and reinforced with tungsten cables appears to be adequate as compared to experimental results and the theoretical results based on rigorous elasticity solution. The latter was based on consideration of multiaxial internal stresses. The approximate theory that was used was sufficient for predicting composite stresses at which ceramic cracking occurred, as well as the ultimate strength of composites.

Since compressive failure of the matrix was one of the failure modes of pre-stressed zirconia, it appears desirable to conduct additional compression tests at room and elevated temperatures in order to be able to predict this failure mode. Further improvements in the correlation between experimental and theoretical results can be made by taking into account such variables as (1) porosity and its effect on various properties of ceramic, (2) effect of grain size on the various properties of ceramic, (3) the influence of material variability, and (4) the variation caused by not attaining a uniform prestress.

APPENDIX
MULTIAXIAL STRESSES IN PRESTRESSED CERAMIC

In order to obtain the magnitude and distribution of the multiaxial stresses in the matrix and the reinforcement of a prestressed system, a model shown in Figure A-1 is used. It consists of a solid cylinder (reinforcement) embedded in a material with different mechanical properties (ceramic). Because the composites in the present study employ small volume fractions of reinforcement, about 10% or less, the filaments are sufficiently far apart so that stress interaction from adjacent fibers is negligible. In view of the above condition, the solution for the problem is similar in form to that for a thick-walled cylinder.

A. 1 MULTIAXIAL STRESSES DUE TO AN EXTERNALLY APPLIED AXIAL LOAD

The first case to be considered is a composite subjected to an external load applied in the z-direction, that is the direction parallel to the reinforcement. The basic differential equation for the problem is (Reference 1)

$$\frac{d}{dr}(\sigma_r r) - \sigma_\theta = 0 \qquad \text{(A1-1)}$$

which may be easily derived by considering the equilibrium of forces acting on an element of a cylinder. The usual stress-strain relationships for the condition of triaxial loading are

$$\epsilon_r = \frac{1}{E}\left[\sigma_r - \nu(\sigma_\theta + \sigma_z)\right] \qquad \text{(a)}$$

$$\epsilon_\theta = \frac{1}{E}\left[\sigma_\theta - \nu(\sigma_r + \sigma_z)\right] \qquad \text{(b)} \qquad \text{(A1-2)}$$

$$\epsilon_z = \frac{1}{E}\left[\sigma_z - \nu(\sigma_\theta + \sigma_r)\right] \qquad \text{(c)}$$

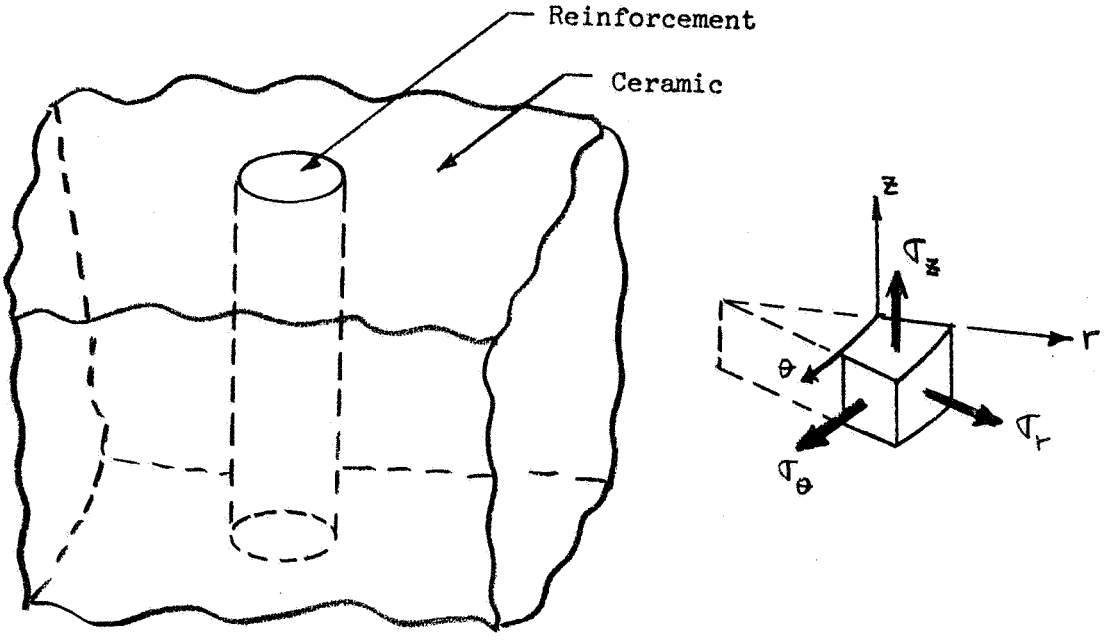

Figure A-1. Model for Determining Triaxial Stresses

from which it follows that

$$\sigma_r = E'\left[\epsilon_r(1-\nu) + \nu(\epsilon_\theta + \epsilon_z)\right] \quad \text{(a)}$$

$$\sigma_\theta = E^1\left[\epsilon_\theta(1-\nu) + \nu(\epsilon_r + \epsilon_z)\right] \quad \text{(b)} \qquad \text{(A1-3)}$$

$$\sigma_z = E1\left[\epsilon_z(1-\nu) + \nu(\epsilon_\theta + \epsilon_r)\right] \quad \text{(c)}$$

where for convenience the following notation has been introduced

$$E^1 = \frac{E}{(1+\nu)(1-2\nu)} \qquad \text{(A1-4)}$$

The relationship between the radial displacement, u, and the strains is

$$\epsilon_\theta = \frac{u}{r} \qquad \text{(A1-5)}$$

$$\epsilon_r = \frac{du}{dr} \tag{A1-6}$$

Combining equations (A1-1), (-3), (-5), and (-6) the resultant differential equation for the problem, in terms of the radial displacements, becomes

$$\frac{d^2u}{dr^2} + \frac{1}{r}\frac{du}{dr} - \frac{u}{r^2} = 0 \tag{A1-7}$$

This equation is valid for the ceramic as well as the reinforcement. The resultant solutions for the displacements in the reinforcement, u_w, and the ceramic, u_c, are

$$u_w = C_1 r + \frac{C_2}{r} \tag{A1-8}$$

$$u_c = C_3 r + \frac{C_4}{r} \tag{A1-9}$$

where C's are the constants of integration which have to be determined from the boundary conditions. For the present problem, the four boundary conditions for evaluating the four constants of integration are:

$$\begin{aligned} &\text{at } r = 0, \; u_w \neq \infty \\ &\text{at } r = b, \; \sigma_{rc} = 0 \\ &\text{at } r = a, \; u_c = u_w \\ &\text{at } r = a, \; \sigma_{rw} = \sigma_{rc} \end{aligned} \tag{A1-10}$$

where the various terms are defined in Figure A-2. The dimension b is related to the fiber volume fraction of a composite, **k,** through the following relationship

$$b = a\,(k)^{-1/2} \tag{A1-11}$$

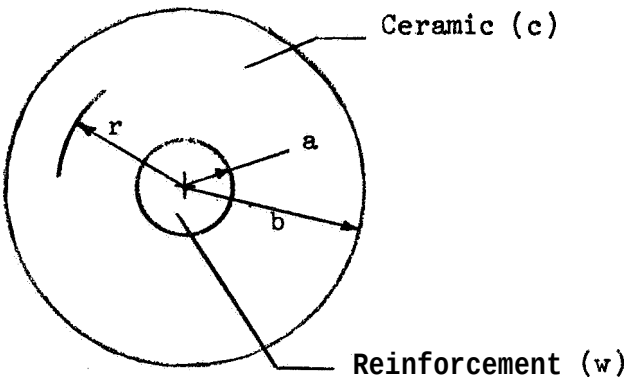

Figure A-2. **Notation**

By combining Equations (A1-5) and (-6) with Equations (A1-3) and substituting Equations (A1-8) and (A1-9) into the resultant equation, the following expressions are obtained for radial and tangential stresses in the constituents

$$\sigma_{rw} = E_w^1 \left[(1-\nu_w)(C_1 - \frac{C_2}{r^2}) + \nu_w (C_1 + \frac{C_2}{r^2}) + \nu_w \epsilon_z \right] \quad \text{(a)}$$

$$\sigma_{\theta w} = E_w^1 \left[(1-\nu_w)(C_1 + \frac{C_2}{r^2}) + \nu_w (C_1 - \frac{C_2}{r^2}) + \nu_w \epsilon_z \right] \quad \text{(b)} \qquad \text{(A1-12)}$$

$$\sigma_{rc} = E_c^1 \left[(1-\nu_c)(C_3 - \frac{C_4}{r^2}) + \nu_c (C_3 + \frac{C_4}{r^2}) + \nu_c \epsilon_z \right] \quad \text{(c)}$$

$$\sigma_{\theta c} = E_c^1 \left[(1-\nu_c)(C_3 + \frac{C_4}{r^2}) + \nu_c (C_3 - \frac{C_4}{r^2}) + \nu_c \epsilon_z \right] \quad \text{(d)}$$

To arrive at the above equations use has also been made of the compatibility condition in the a-direction

$$e_{zw} = {}_{a}e_{c} = \epsilon_z \tag{A1-13}$$

By combining Equations (A1-12) with the boundary conditions given by Equations (A1-10), the final expressions for the four constants of integration are found to be:

$$C_1 = \frac{\left\{E_w^1 \nu_w \left[k(2\nu_c - 1) - 1\right] - E_c^1 \nu_c (k-1)(2\nu_c - 1)\right\}\epsilon_z}{E_c^1 (2\nu_c - 1)(k-1) - E_w^1 \left[k(2\nu_c - 1) - 1\right]}$$

$$C_2 = 0 \tag{A1-14}$$

$$C_3 = \frac{\nu_c \epsilon_z t\, k(2\nu_c - 1) C_1}{(2\nu_c - 1)k - 1}$$

$$C_4 = k(C_1 - C_3)$$

where e_z is still an unknown. By introducing the notation

$$A = \frac{E_w^1 \nu_w \left[k(2\nu_c - 1) - 1\right] - E_c^1 \nu_c (k-1)(2\nu_c - 1)}{E_c^1 (2\nu_c - 1)(k-1) - E_w^1 \left[k(2\nu_c - 1) - 1\right]} \tag{A1-15}$$

$$B = \frac{\nu_c t\, k(2\nu_c - 1) A}{(2\nu_c - 1)k - 1} \tag{A1-16}$$

the C's may be expressed as

$$C_1 = A\epsilon_z$$

$$C_2 = 0 \tag{A1-17}$$

$$C_3 = B\epsilon_z$$

$$C_4 = (A-B)k\epsilon_z$$

which when substituted into Equations (A1-12) yield the following expressions for the stresses:

$$\sigma_{rw} = E_w^1 (A \, t \, \nu_w)\epsilon_z$$

$$\sigma_{\theta w} = E_w^1 (A + \nu_w)^E z$$

$$\sigma_{rc} = E_c^1 \left\{ B\left[1 + (a^2/_r 2)(1-2\nu_c)\right] + A(a^2/_r 2)(2\nu_c - 1) + \nu_c \right\} \epsilon_z \qquad \text{(A1-18)}$$

$$\sigma_{\theta c} = E_C^1 \left\{ B\left[1 - (a2/_r 2)(1-2\nu_c)\right] - A(a2/_r 2)(2\nu_c - 1) \, t \, \nu_c \right\} \epsilon_z$$

The relationship between E_z and the remotely applied average axial stress, σ_z, may be obtained by considering force equilibrium in the z-direction, which is

$$\int_o^a 2\pi r(\sigma_{zw})\, dr + \int_a^b 2\pi r(\sigma_{zc})\, dr = \pi b^2 \sigma z \qquad \text{(A1-19)}$$

The axial stresses in the reinforcement and the matrix are (from Equations A1-2)

$$\sigma_{zw} = \epsilon_z E_w \, t \, v_w(\sigma_{\theta w} + \sigma_{rw})$$

$$\sigma_{ZC} = \epsilon_z E_c + \nu_\epsilon (\sigma_{\theta c} \, t \, u_{rc}) \qquad \text{(A1-20)}$$

which when combined with Equations (A1-18) become

$$\sigma_{zw} = \left[E_w + 2\nu_w E_w^1 (A + \nu_w)\right] \epsilon_z$$

$$\sigma_{zc} = \left[E_c + 2\nu_c E_c^1 (B + \nu_c)\right] \epsilon_z \qquad \text{(A1-21)}$$

Substitution of the above expressions in two Equations (A1-19), and solving the resultant equation for ϵ_z yields

$$\epsilon_z = \frac{\sigma_z}{\left[E_w + \nu_w E_w^1 (2A + 2\nu_w)\right] k + \left[E_c + \nu_c E_c^1 (2B + 2\nu_c)\right] (1-k)} \qquad \text{(A1-22)}$$

Equations (A1-18) and (A1-21) in combination with expression given by Equation (A1-22) are the final expressions for the triaxial stresses in the constituents of a prestressed ceramic. They are given as a function of the properties of the constituents and the magnitude of the externally applied axial stress.

A. 2 MULTIAXIAL STRESSES DUE TO A MECHANICAL PRESTRESS

The multiaxial stresses induced in the constituents by a mechanical prestress of the reinforcement may be determined in a manner similar to that used above. In a prestressed system, the ceramic "slurry" is deposited onto prestressed fibers, allowed to cure and the end restraints inducing the prestress are then removed. The removal of the fiber end restraints causes stress transfer from the fibers to the matrix until force equilibrium is satisfied. After the removal of end restraint the conditions of strain compatibility and force equilibrium require that

$$\overline{\epsilon}_{zw} = \overline{\epsilon}_{zc} = \overline{\epsilon}_z \qquad \text{(A2-1)}$$

$$\bar{\sigma}_{zwk} + \bar{\sigma}_{zc}(1-k) = 0 \qquad \text{(A2-2)}$$

where $\bar{\sigma}_{zc}$ is the induced stress in the ceramic, and $\bar{\sigma}_{zw}$ is the remaining stress in the fibers. The latter quantity is related to the applied fiber prestress, $\bar{\sigma}_{wi}$, by the following relationship

$$\bar{\sigma}_{zw} = \sigma_{wi} + \Delta\sigma_{zw} \qquad \text{(A2-3)}$$

where $\Delta\sigma_{zw}$ is the change of stress in the reinforcement due to deformation of the ceramic. In view of Equations (A1-21) and utilizing Equation (A2-1), we can write

$$\Delta\sigma_{zw} = \bar{\epsilon}_z \left(E_w + \nu_w E_w^{1}(2A + 2\nu_w) \right| \qquad \text{(A2-4)}$$

$$\sigma_{zc} = \bar{\epsilon}_z \left| E_c t\ \nu_c E_c^{1}(2B + 2\nu_c) \right| \qquad \text{(A2-5)}$$

Combining Equations (A2-2), (-3), (-4) and (-5) and solving for $\bar{\epsilon}_z$ yields

$$\bar{\epsilon}_z \simeq \frac{-\sigma_{wi}k}{\left[E_w\ t\ \nu_w E_w^{1}(2A\ t\ 2\nu_w)\right]k + \left[E_c + \nu_c E_c^{1}(2B + 2\nu_c)\right](1-k)} \qquad \text{(A2-6)}$$

The final expressions for the triaxial stresses in the constituents due to mechanical prestress are:

$$\bar{\sigma}_{rw} = E_w^1 (A + \nu_w)\ \bar{\epsilon}_z$$

$$\bar{\sigma}_{\theta w} = E_w^1 (A\ t\ \nu_w)\ \bar{\epsilon}_z$$

$$\bar{\sigma}_{zw} = \sigma_{wi}\ t\ [E_w\ t\ \nu_w E_w^1 (2A\ t\ 2\nu_w)]\ \bar{\epsilon}_z \qquad \text{(A2-7)}$$

$$\sigma_{rc} = E_C^1 \left\{ B\left[1 + (a^2/r^2)(1-2\nu_c)\right] + A(a2/r^2)(2\nu_c - 1) + \nu_c \right\} \bar{\epsilon}_z$$

$$\sigma_{\theta c} = E_c^1 \left\{ B\left[1 - (a2/r^2)(1-2\nu_c)\right] - A(a2/r^2)(2\nu_c - 1)\ t\ \nu_c \right\} \bar{\epsilon}_z$$

$$\bar{\sigma}_{zc} = \left[E_c + \nu_c E_c^1 (2B + 2\nu_c)\right] \bar{\epsilon}_z$$

where $\bar{\epsilon}_z$ is given by Equation (A2-6), A is defined in Equation (A1-15), B is defined in Equation (A1-16), and E^1 is defined in Equation (A1-4).

A. *3* NUMERICAL RESULTS

To establish the effect of multiaxial internal stresses on the strength and behavior of prestressed ceramics, several numerical examples are considered. The properties of the constituents used in these examples are those obtained experimentally. The results given are for alumina and zirconia prestressed with 49-strand tungsten cable. Numerical results are presented only for the multiaxial stresses due *to* an externally applied load. In view of the similarity of Equations (A 1-18), (-21), and (-22) with Equations (A2-6) and (A2-7) the conclusions reached from considerations of the effect of multiaxial stresses for the case of external loading will also apply *to* the case of mechanical prestress. Moreover, the relative importance of multiaxial stresses obtained from consideration of externally loaded composite should also apply to the case when the composite is loaded externally and also subjected *to* elevated temperature.

A. 3. 1 Arbitrary Composite with $\nu_c = \nu_w = \nu$.

For the case when the Poisson's ratios of the constituents are equal it follows from (A1-15) and(A1-16) that:

$$A = -\nu$$

$$B = -\nu \qquad \text{(A3. 1-1)}$$

Substitutions of these values into Equations (A1-18), (-21), and (-22) yields

$$\sigma_{rw} = \sigma_{\theta w} = \sigma_{rc} = \sigma_{\theta c} = 0 \qquad \text{(A3. 1-2)}$$

$$\epsilon_z = \frac{\sigma_z}{E_w k + E_c(1-k)} \qquad \text{(A3. 1-3)}$$

$$\sigma_{zw} = E_w \epsilon_z \qquad \text{(A3. 1-4)}$$

$$\sigma_{zc} = E_c \epsilon_z \qquad \text{(A3. 1-5)}$$

which results are identical to the elementary results (Section 3) based on consideration of uniaxial state of stress. Thus if the Poisson's ratios of the constituent materials are the same, the rigorous and elementary solutions give identical results for composites consisting of arbitrary combinations of materials.

A. 3. 2 Alumina-Tungsten Composite

For the case of a composite consisting of chemically bonded alumina reinforced with tungsten fibers, and subjected to an external load, the multiaxial internal stresses in the constituents are summarized in Figure A-3. The stresses shown are those that exist at the ceramic-reinforcement interface; the stresses are maximum at this point. As was pointed above, when the Poisson's ratios of the materials are equal, only the axial stresses are present; the radial and tangential stresses in the constituents are identically

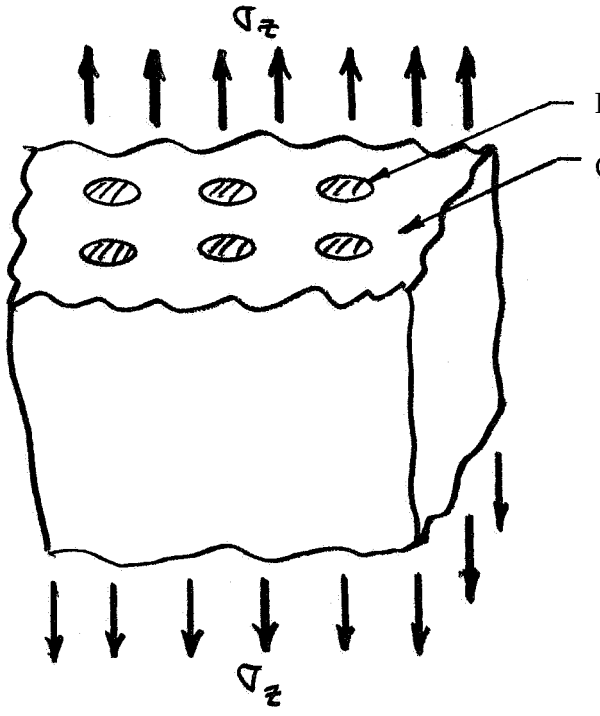

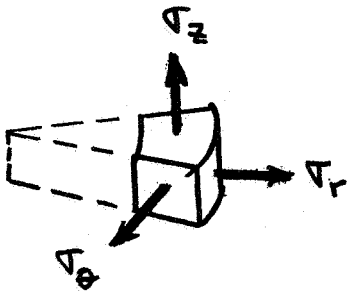

Reinforcement: 49-strand tungsten cable

Ceramic: chemically bonded alumina

$k = 0.10$ (reinforcement volume fraction)

$E_w = 23.9 \times 10^6$ psi

$E_c = 16.1 \times 10^6$ psi

σ_z = Externally applied stress

SUMMARY OF MULTIAXIAL STRESSES AT CERAMIC-REINFORCEMENT INTERFACE

Poisson's Ratios of Constituents	ν_c	0	0.2	0.284	0.3	0.4
	ν_w	0.284	0.284	0.284	0.284	0.284
Stresses in the Reinforcement	σ_{rw}/σ_z	0.1681	0.0448	0	-0.0081	-0.0564
	$\sigma_{\theta w}/\sigma_z$	0.1681	0.0448	0	-0.0081	-0.0564
	σ_{zw}/σ_z	1.4978	1.4403	1.4159	1.4112	1.3820
Stresses in the Ceramic	σ_{rc}/σ_z	0.1681	0.0448	0	-0.0081	-0.0564
	$\sigma_{\theta c}/\sigma_z$	-0.2055	-0.0548	0	0.0099	0.0853
	σ_{zc}/σ_z	0.9447	0.9511	0.9538	0.9543	0.9576
Axial Strain Ratio (1)	$\varepsilon_z/\varepsilon_z^*$	0.99045	0.99924	1.00000	0.99997	0.99869

(1) ε_z is the strain obtained from rigorous solution (based on triaxial stresses); ε_z^* is the strain obtained from elementary solution (based on uniaxial state of stress).

Figure A-3. Summary of Multiaxial Stresses in Alumina Reinforced with Tungsten Fibers

equal to zero. For the case when Poisson's ratios of the constituents are not equal, the internal stresses in the constituents will be as shown in Figure **A-3.**

For alumina, the Poisson's ratio ranges between $\nu_C = 0.2$ to $\nu_C = 0.3$ depending on the porosity. From Figure **A-3** it is quite obvious that for either of the above values the radial and tangential stresses are negligibly small as compared to the axial stresses. Moreover, the axial stresses, σ_{zc} and σ_{zw}, are within 2% of the values corresponding to those based on elementary theory (Section **3),** which neglects the effect due to Poisson's ratios. The axial strains predicted by the elementary and rigorous theories agree to within 1%. The results shown in Figure **A-3** justify the use of the simple theory for predicting the strength and behavior of prestressed reinforced ceramics under consideration.

To establish the effect of the multiaxial stresses on the strength of prestressed ceramics, one can use either the maximum stress theory or maximum strain theory to predict the strength of ceramic. If maximum strain theory is used, then from Figure **A-3** it follows that the strength based on consideration of multiaxial stresses is always greater than the strength based on elementary theory. The difference, however, does not exceed 1%. If maximum stress theory is used, then the allowable strength based on consideration of multiaxial stresses is greater than the allowable strength based on consideration of uniaxial stresses if $\nu_C > \nu_w$; the reverse is true if $\nu_C < \nu_w$. Even for large differences in Poisson's ratios of the constituents, the difference between allowable strengths based on the rigorous and simple theories is negligible (about 2% and less).

Away from the interface, the radial and tangential stresses in the ceramic will depend on the radial distance. They are, however, maximum at the ceramic-reinforcement interface and diminish with increasing radial distance. In the reinforcement, the radial, tangential, and axial stresses remain constant and equal to the values of the reinforcement stresses at the interface. **A** typical stress distribution is shown in Figure **A-4.**

FIGURE A-4
INTERNAL MULTIAXIAL STRESSES
IN ALUMINA REINFORCED WITH
TUNGSTEN FIBERS

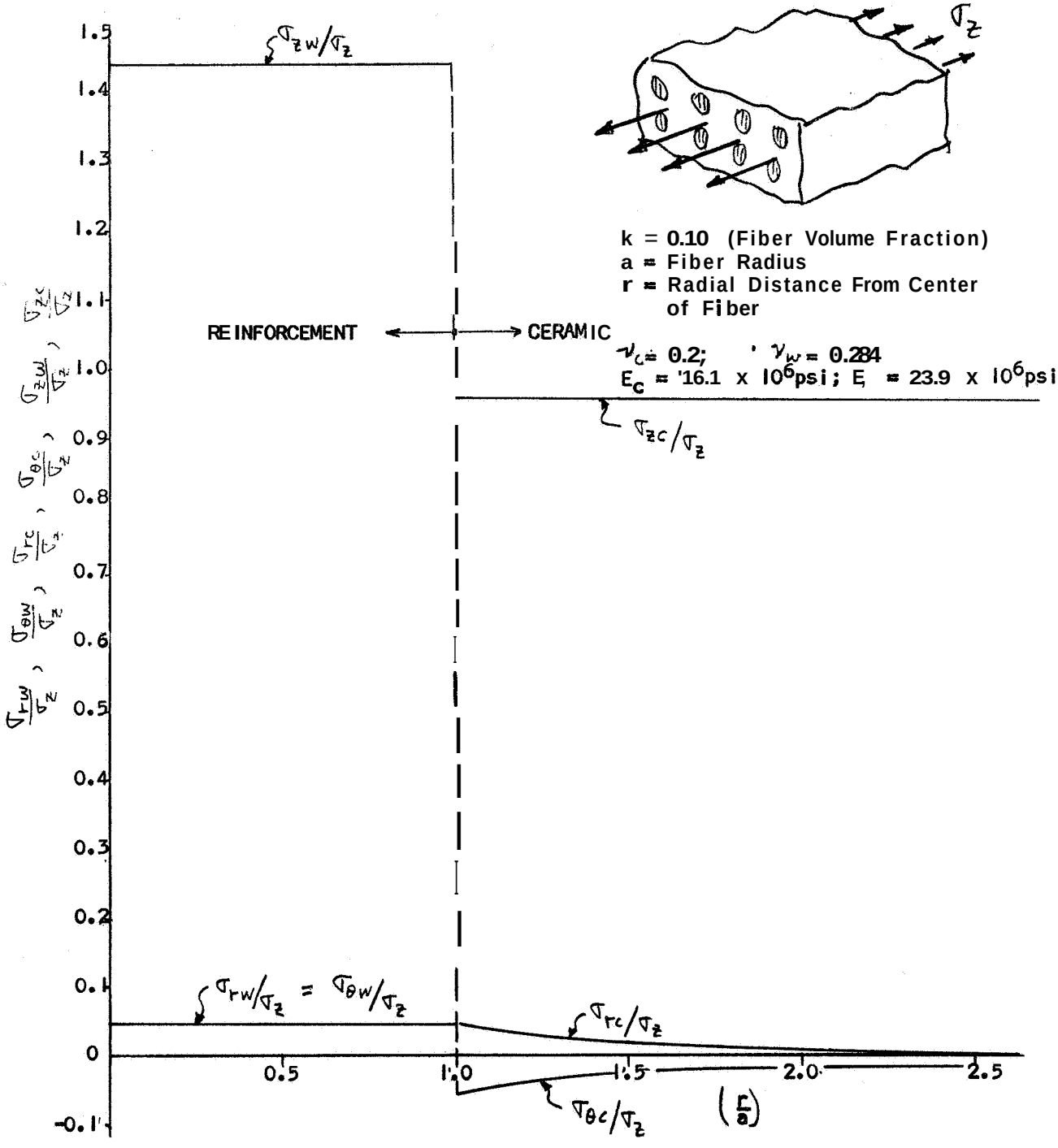

Figure A-4. Internal Multiaxial Stresses in Alumina Reinforced with Tungsten Fibers

A. 3. 3 Zirconia-Tungsten Composite

For the case of a composite consisting of chemically bonded zirconia reinforced with tungsten fibers and subjected to an external load, the stresses in the constituents are summarized in Figure A-5, as in the previous example the radial and tangential stresses in the constituents are negligibly small as compared to the axial stresses. The values of the axial stresses obtained from the rigorous solution agree with the stresses obtained from the solution which ignores the Poisson's ratio effect. Regarding the importance and effect of multiaxial stresses, the conclusions for this case are the same as for the previous case.

A. 3. 4 Effect of Fiber Volume Fraction

To establish the effect of fiber volume fraction on the multiaxial stresses, the worst case will be considered -- the Poisson's ratio of the ceramic will be taken as zero $v_C = 0$. For the case of $\nu_c = 0$, the constants A and B become

$$A = \frac{E_w^1 \nu_w (1 + k)}{E_c (k-1) - E_w^i (1+k)} \qquad \text{(A3.4-1)}$$

$$B = \frac{kA}{1 t k} \qquad \text{(A3. 4-2)}$$

while for the case of externally applied loading the expression for axial strain, ε_z, given by Equation (A1-21) simplifies to

$$\varepsilon_z = \frac{\sigma_z}{\left| E_w \; t \; v_w E_w^1 (2 A t 2\nu_w) \right| k + E_C (1-k)} \qquad \text{(A3. 4-3)}$$

From Equations (A1-18) and (A1-21), the expressions for multiaxial stresses now become

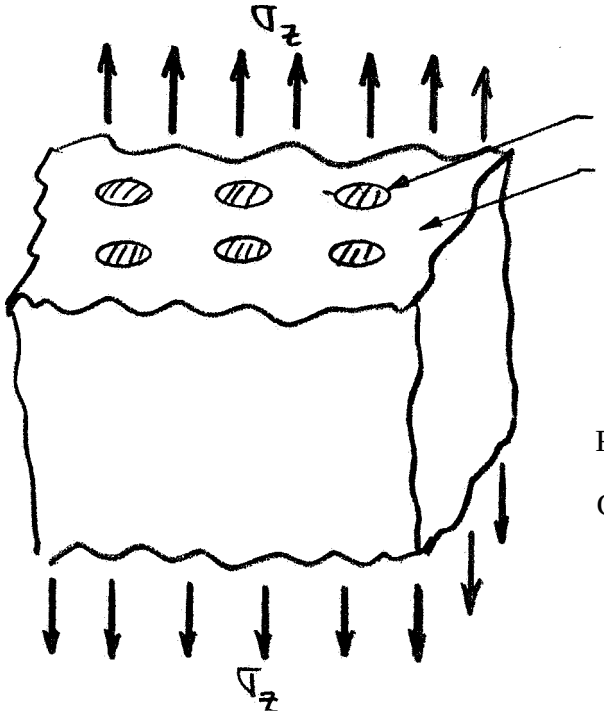

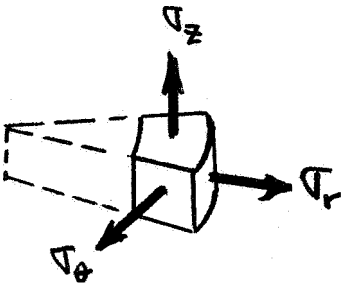

Reinforcement : 49-strand tungsten cable

Ceramic: Chemically bonded zirconia

k = 0.10 (fiber volume fraction)

$E_w = 23.9 \times 10^6$ psi

$E_C = 6.4 \times 10^6$ psi

SUMMARY OF MULTIAXIAL STRESSES AT CERAMIC-REINFORCEMENT INTERFACE

Poisson's Ratios of Constituents	ν_c	0	0.2	0.284	0.4
	ν_w	0.284	0.284	0.284	0.284
Stresses in the Reinforcement	σ_{rw}/σ_z	0.1612	0.0422	0	-0.0524
	$\sigma_{\theta w}/\sigma_z$	0.1612	0.0422	0	-0.0524
	σ_{zw}/σ_z	2.9972	2.9544	2.9325	2.899
Stresses in the Ceramic	σ_{rc}/σ_z	0.1612	0.0422	0	0.0524
	$\sigma_{\theta c}/\sigma_z$	-0.1970	-0.0516	0	0.0641
	σ_{zc}/σ_z	0.7781	0.7828	0.7853	0.7890
Axial Strain Ratio	$\varepsilon_z/\varepsilon_z^*$	0.99084	0.99929	1.00000	0.99879

Figure A-5. Summary of Multiaxial Stresses in Zirconia Reinforced with Tungsten Fibers

$$
\begin{aligned}
\sigma_{rw} &= E_w^1 (A + \nu_w)\epsilon_z && \text{(a)} \\
\sigma_{\theta w} &= E_w^1 (A + \nu_w)\epsilon_z && \text{(b)} \\
\sigma_{zw} &= \left[E_w + 2\nu_w E_w^1 (A + \nu_w)\right]\epsilon_z && \text{(c)}
\end{aligned}
\qquad \text{(A3.4-4)}
$$

$$
\begin{aligned}
\sigma_{rc} &= E_c\left[B + \left(\frac{a}{r}\right)^2 (B - A)\right]\epsilon_z && \text{(a)} \\
\sigma_{\theta c} &= E_c\left[B - \left(\frac{a}{r}\right)^2 (B - A)\right]\epsilon_z && \text{(b)} \\
\sigma_{zc} &= E_c \epsilon_z && \text{(c)}
\end{aligned}
\qquad \text{(A3.4-4)}
$$

Using the above equations, multiaxial internal stresses were computed at the interface of tungsten reinforced alumina, for composites incorporating various volume fractions of the reinforcement. The results are shown in Figure A-6. The properties of the constituents were taken as:

$$E_w = 23.9 \times 10^6 \text{ psi} \qquad \nu_w = 0.284$$

$$E_c = 16.1 \times 10^6 \text{ psi} \qquad \nu_c = 0$$

The internal stresses increase with the decreasing fiber volume fraction. For high fiber volume fractions, however, one would expect interaction of stresses from the adjacent filaments. This would, for high fiber volume fraction, cause the reversal in the fiber volume-stress relationship, that is, stresses may increase with increasing fiber volume. On the basis of information presented in Figure A-4 and Figure A-6, it appears reasonable to neglect stress interaction for $k \lesssim 0.20$. Even for the worst case ($\nu_c = 0$),

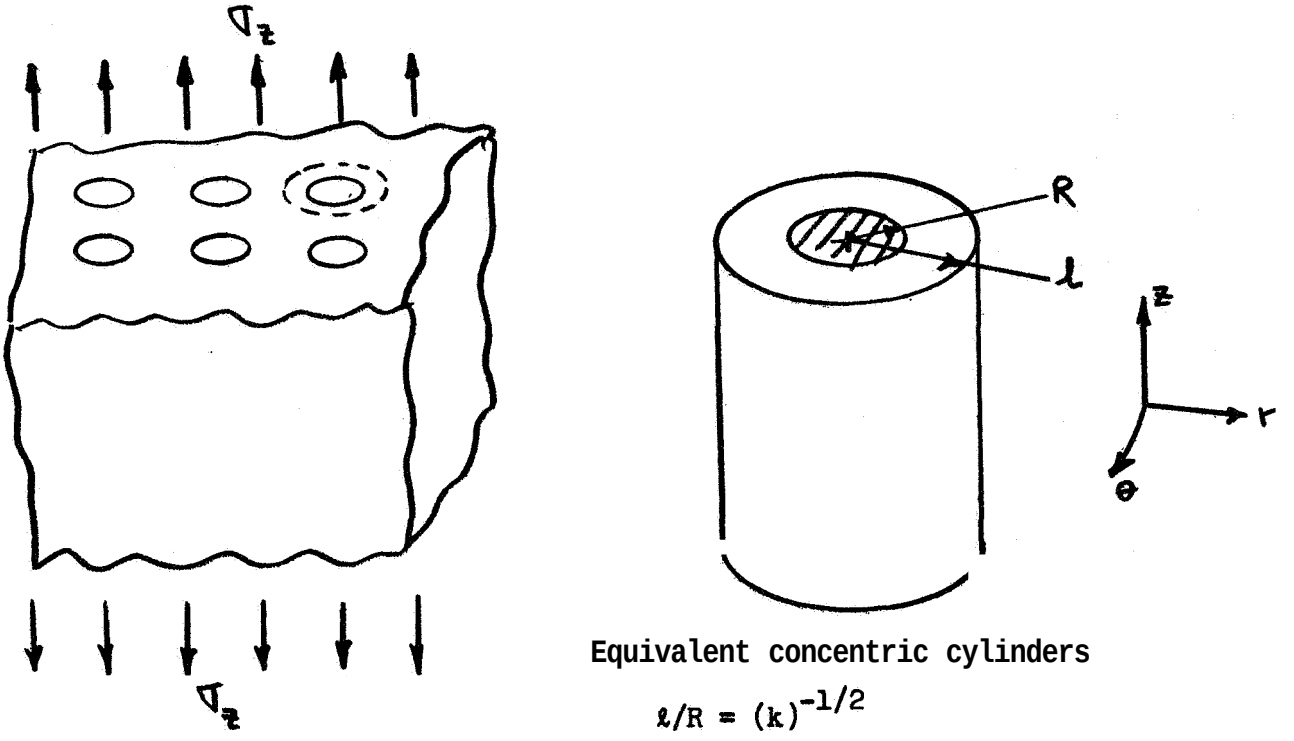

Equivalent concentric cylinders

$\ell/R = (k)^{-1/2}$

SUMMARY OF MULTIAXIAL STRESSES AT CERAMIC-REINFORCEMENT INTERFACE AS A FUNCTION OF REINFORCEMENT VOLUME

Reinforcement Volume Faction	k	0	0.05	0.10	0.20	0.40
	ℓ/R	∞	4.47	3.16	2.24	1.58
Stresses in the Reinforcement	σ_{rw}/σ_z	0.2065	0.1866	0.1681	0.1360	0.0861
	$\sigma_{\theta w}/\sigma_z$	0.2065	0.1866	0.1681	0.1360	0.0861
	σ_{zw}/σ_z	1.6032	1.5460	1.4978	1.4093	1.2690
Stresses in the Ceramic	σ_{rc}/σ_z	0.2065	0.1866	0.1681	0.1360	0.0861
	$\sigma_{\theta c}/\sigma_z$	-0.2065	-0.2060	-0.2055	-0.2040	-0.2012
	σ_{zc}/σ_z	1.0000	0.9700	0.9447	0.8970	0.8210

Figure A-6. Effect of Reinforcement Volume Fraction on Multiaxial Stresses in a Tungsten Reinforced Alumina

the radial and tangential stresses in the constituents are quite small as compared to the axial stresses. This further substantiates the conclusions reached in the previous cases, that is, that the theory which neglects the effect of Poisson's ratio is sufficient for composites presently under investigation. More important, the error in the results obtained from the rigorous and the simple theory is significantly less than the scatter in test data on the properties of the constituents.

A. 4 REFERENCES FOR APPENDIX

1. S. P. Timoshenko, Strength of Materials, Part II, D. Van Nostrand Company, Inc., New York, N. Y., (1955).

DISTRIBUTION LIST

Addressee	Number of Copies
Mr. Norman J. Mayer Code RV-2 NASA Headquarters Washington, D. C. 20546	4
Mr. Richard R. Heldenfels Code 23.000, Mail Stop 188 NASA Langley Research Center Langley Station Hampton, Virginia 23365	2
Mr. Paul R. Hill Code 61.000, Mail Stop 213 NASA Langley Research Center Langley Research Center Langley Station Hampton, Virginia 23365	1
Library NASA Langley Research Center Langley Station Hampton, Virginia 23365	1
Mr. Jack B. Esgar Code 2320, Mail Stop 49-1 NASA Lewis Research Center 21000 Brookpark Road Cleveland, Ohio 44135	1
Mr. Donald L. Nored Code 9522, Mail Stop 500-209 NASA Lewis Research Center 21000 Brookpark Road Cleveland, Ohio 44135	1
Library NASA Lewis Research Center 21000 Brookpark Road Cleveland, Ohio 44135	1

Addressee	Number of Copies
Mr. Emil A. Hellebrand Code R-P&VE-DIR NASA Marshall Space Flight Center Huntsville, Alabama 35812	1
Mr. Joseph F. Blumrich Code R-P&VE-SA NASA Marshall Space Flight Center Huntsville, Alabama 35812	1
Associate Chief Counsel - Patent Matters, CC-P NASA Marshall Space Flight Center Huntsville, Alabama 35812	1
Scientific & Technical Information Branch, MS-1 NASA Marshall Space Flight Center Huntsville, Alabama 35812	2
Materials Division, R-P & VE-M Attn: Vaughn F. Seitzinger NASA Marshall Space Flight Center Huntsville, Alabama 35812	5
Dr. William R. Lucas Code R-P&VE-M NASA Marshall Space Flight Center Huntsville, Alabama 35812	1
Library NASA Marshall Space Flight Center Huntsville, Alabama 35812	1
Mr. Albert L. Erickson Mail Stop N-218-1 NASA Ames Research Center Moffett Field, California 94035	1
Library NASA Ames Research Center Moffett Field, California 94035	1
Mr. William H. Gayman Section 353, Mail 156-119 Jet Propulsion Laboratory 4800 Oak Grove Drive Pasadena, California 91103	1

Addressee	Number of Copies
Mr. Joseph N. Kotanchik Code ES NASA Manned Spacecraft Center Houston, Texas 77058	1
Library NASA Manned Spacecraft Center Houston, Texas 77058	1
Mr. Daniel G. Mazur Code 620 NASA Goddard Space Flight Center Greenbelt, Maryland 20771	1
Mr. Edward J. Kirchman Code 321 NASA Goddard Space Flight Center Greenbelt, Maryland 20771	1
Library NASA Goddard Space Flight Center Greenbelt, Maryland 20771	1
Mr. Harry Williams NASA Western Operations Office 150 Pico Boulevard Santa Monica, California 90406	1
Dr. Stephen W. Tsai Philco Corporation Aeronutronic Division Ford Road Newport Beach, California	1
Prof, Francis R. Shanley Department of Engineering University of California Los Angeles, California 90024	1
Mr. Ralph L. Barnett IIT Research Institute 10 West 35th Street Chicago, Illinois 60616	1
Dr. Hans U. Schuerch Astro Research Corporation P. O. Box 4128 Santa Barbara, California	1

Addressee	Number of Copies
Mr. William J. Eakins DeBell & Richardson, Inc. Hazardville, Connecticut 06036	1
Mr. James C. Withers General Technologies Corporation 708 North West Street Alexandria, Virginia	1
Mr. B. Walter Rosen General Electric Company P. O. Box 8555 Philadelphia, Pennsylvania	1
Dr. Anthony M. Schwartz Assistant Director Harris Research Laboratories, Inc. 6220 Kansas Avenue, NE Washington, D, C, 20011	1
Mr. Jack H. Ross Code ASRCN-3 Wright-Patterson Air Force Base Ohio 45433	1
Mr. J. M. Whitney Code MANC Wright-Patterson Air Force Base Ohio 45433	1
Mr. R. F. Hoener Structures Division, Code FDT Wright-Patterson Air Force Base Ohio 45433	1
Mr. George Peterson Advanced Filaments & Composites Division Code MAC Air Force Materials Laboratory Wright-Patterson Air Force Base Ohio 45433	1
Mr. J. A. Kies Naval Research Laboratory Washington, D. C.	1

Addressee	Number of Copies
Mr. N. E. Promisel Materials Division, RRMA Bureau of Weapons Department of the Navy Washington, D. C.	1
Mr. Paul Stone Materials Division, RRMA Bureau of Weapons Department of the Navy Washington, D. C.	1
Mr. W. R. Graner Code 634C Bureau of Ships Department of the Navy Washington, D. C.	1
Mr. Eldon E. Mathauser Code 23.600, Mail Stop 188 NASA Langley Research Center Langley Station Hampton, Virginia 23365	1
Mr. Edward F. Baehr Mail Stop 500-116 NASA Lewis Research Center 21000 Brookpark Road Cleveland, Ohio 44135	1
Dr. Julian H. Lauchner Dean, School of Technology Southern Illinois University Carbondale, Illinois 62903	1